Stellingen behorende bij het proefschrift

Cloud measurements with radar

Victor Venema, 13 november 2000

1. Coherent particle scattering can be an important mechanism in the scattering of radio waves by clouds.

   Coherente deeltjesverstrooiing kan een belangrijk mechanisme voor de verstrooiing van radiogolven door wolken zijn.

2. It is likely that coherent scattering by spatial cloud or humidity structures dominates incoherent particle scattering in S-band radar measurements of stratocumulus clouds.

   Het is waarschijnlijk dat coherente verstrooiing door ruimtelijke structuren in de hoeveelheid wolkenwater of in de luchtvochtigheid sterker is dan incoherente deeltjesverstrooiing in S-band radar metingen van stratocumuluswolken.

3. Because the retrievals of cloud properties can be significantly improved by combining information from different instruments, having a super-measurement site with a large variety of instruments will be very valuable.

   Daar de bepaling van wolkeneigenschappen significant kan worden verbeterd door het combineren van informatie afkomstig van verschillende instrumenten, zal een meetfaciliteit met een grote verscheidenheid van instrumenten zeer waardevol zijn.

4. The height of cloud boundaries can be measured much more reliably and accurately when radar and lidar are combined. In the future it should be possible to carry out these measurements without the help of a lidar under most atmospheric conditions by using smart radar measurement techniques.

   De hoogte van de wolkengrenzen kan veel betrouwbaarder en nauwkeuriger gemeten worden door radar en lidar te combineren. In de toekomst moet het mogelijk zijn om dit soort metingen onder de meeste atmosferische omstandigheden zonder hulp van de lidar uit te voeren door gebruik te maken van slimme radar meettechnieken.

5. Met een (klimaat)model kunnen nooit met zekerheid voorspellingen gedaan worden over een nieuw éénmalig probleem als het versterkte broeikaseffect. In deze en vele andere gevallen moet de wetenschap duidelijk maken waar haar beperkingen liggen.

6. Wetenschappers die milieuvervuiling willen verwerken in een Groen Bruto Nationaal Product tellen appels bij peren op. Dit is de taak van de politiek en niet van de wetenschap.

7. In de wetenschap en de maatschappij zijn overweldigend veel meer ideeën aanwezig dan ik ooit zou kunnen bedenken. Naast 'ik denk dus ik besta', kan dus ook gesteld worden dat anderen duidelijk ook denken en dus ook bestaan.

8. In een niet-deterministische wereld heeft de mens net zoveel vrije wil als in een deterministische wereld.

9. De evolutietheorie is een beschrijvende theorie, daar de uitkomst van 'survival of the fittest' pas achteraf kan worden bepaald in een niet-stationaire omgeving.

10. Het zou de belastingdiscipline verbeteren als mensen bij de opgave van hun inkomstenbelasting zelf mogen aangeven bij welk(e) ministerie(s) het geld moet worden besteed.

11. Kiesrecht voor allochtonen bevordert de integratie omdat dit de interesse in de Nederlandse politiek vergroot.

Cloud measurements with radar

Cloud measurements with radar

Wolkenmetingen met radar

Proefschrift

ter verkrijging van de graad van doctor
aan de Technische Universiteit Delft,
op gezag van de Rector Magnificus prof. ir. K.F. Wakker,
voorzitter van het College voor Promoties,
in het openbaar te verdedigen op maandag 13 november 2000 te 16.00 uur
door Victor Karel Christiaan VENEMA
doctorandus in de natuurkunde
geboren te Groningen

Dit proefschrift is goedgekeurd door de promotor:
Prof. dr. ir. L.P. Ligthart

Toegevoegd promotor: dr. ir. H.W.J. Russchenberg

Samenstelling promotiecommissie:

Rector Magnificus,	Voorzitter
Prof. dr. ir. L.P. Ligthart,	Technische Universiteit Delft, promotor
Prof. dr. ir. G. Brussaard,	Technische Universiteit Eindhoven
Prof. dr. J.W. Hovenier	Vrije Universiteit Amsterdam & Universiteit van Amsterdam
Dr. A.J. Illingworth	Universiteit van Reading, UK
Prof. dr. ir. F.T.M. Nieuwstadt	Technische Universiteit Delft
Dr. ir. H.W.J. Russchenberg	Technische Universiteit Delft, toegevoegd promotor

ISBN: 90-804551-9-9

Contents

Chapter 1

Introduction

1.1 CLARA

Clouds are an important component of the climate system. They reflect the light of the sun, retain the heat of the earth, produce precipitation, and are necessary for many important chemical reactions in the atmosphere. In 1996 the properties of the Dutch clouds were measured in three large cloud measurement campaigns. The emphasis lay on the cloud properties that are important for the radiative balance of the earth, thus the name of these campaigns: CLARA, *CLouds And RAdiation; an intensive experimental study of clouds and radiation in the Netherlands.* In these campaigns the macrophysical and microphysical cloud properties were measured in situ by aeroplane and with a large number of remote sensing devices: S-band radar, near-infrared and optical lidar, microwave radiometer, infrared radiometer, radiosondes, satellites and GPS, amongst others [Van Lammeren et al., 1999]. The campaigns focused on stratiform water clouds, stratocumulus and stratus.

CLARA started as an initiative of four Dutch institutes: the Royal Netherlands Meteorological Institute (KNMI), the International Research Centre for Telecommunications-transmission and Radar (IRCTR), the National Institute of Public Health and the Environment (RIVM) and the Netherlands Energy Research Foundation (ECN). This PhD thesis was prepared at the IRCTR, a radar research institute at the faculty of Information Technology and Systems at the Delft University of Technology. See section 2.1 for more information on the CLARA project.

Figure 1.1. The Delft Atmospheric Research Radar, DARR, on the roof of the Electrical Engineering building. On the background the X-band (3-cm wavelength) radar SOLIDAR is visible.

1.2 Scientific aims

The global climate is changing due to human activities, mainly the burning of fossil fuels and changes in land use. Both activities lead to higher concentrations of carbon dioxide and methane in the atmosphere, which trap heat radiation at the earth's surface. This extra amount of energy results in higher temperatures and an increase in the fluxes of the hydrological cycle. Expected consequences are: more violent storms, an increase in incidence of extremely high temperatures, droughts, floods, and fires, more outbreaks of pests, a rising sea level, an increase of the incidence in tropical diseases, and a reduction of the biodiversity [Watson et al., 1996]. To make better decisions on averting these severe dangers we need a clearer understanding of the climate system.

A large source of uncertainty in the predictions of the future climate is the reaction of the cloud system to climate change. The cloud feedback is the largest source of uncertainty in the climate-change calculations in current climate models [Kattenberg et al., 1996]. The influence of clouds on the radiative transfer through the at-

mosphere, and thus on our climate, is large. Clouds have a cooling effect: they reflect solar radiation and radiate heat to space. They also have a warming effect, because clouds trap the heat emitted by the earth. To quantify these effects we must understand the macro and micro properties of clouds.

Important cloud parameters for research on the interaction between clouds and radiation are cloud height (base and top), liquid (or ice) water content, the particle number density and their diameter. *This thesis focuses on improving (our understanding of) radar measurements of the height of cloud boundaries and liquid water content of clouds.*

1.3 Radar and lidar technology

A radar transmits a radio wave and measures the part of the wave that is reflected by a target. The difference between the time the wave is transmitted and received is used to measure the distance of the target. The properties of the reflected wave can be used to infer properties of the target (e.g., its velocity or shape). The radar of the TU Delft used in CLARA is called DARR, Delft Atmospheric Research Radar, Fig. 1.1. It is a rather large instrument with antennas of 2 and 4 m. DARR uses a wavelength

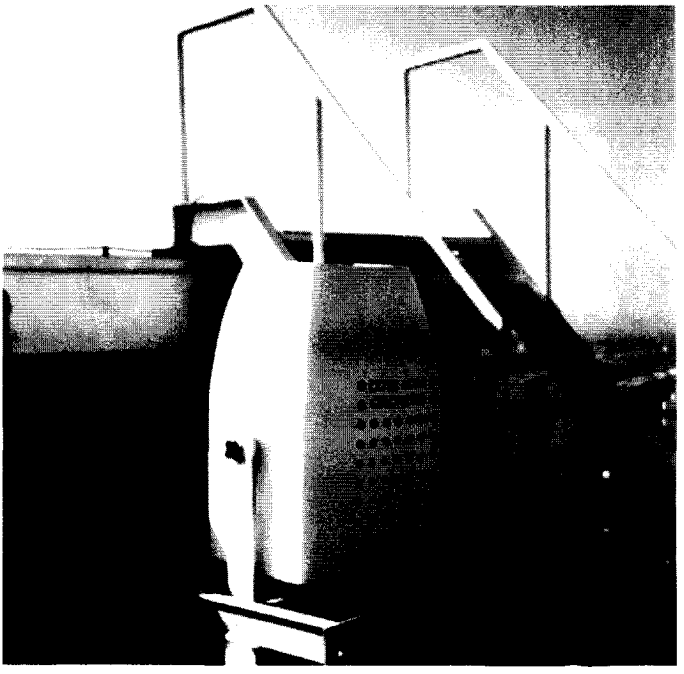

Figure 1.2. The Vaisala CT-75K lidar ceilometer on the roof during the CLARA campaigns.

of 9 cm and is therefore a so-called S-band radar. During the cloud measurements in this thesis DARR always pointed towards the zenith. Before CLARA, DARR was mainly used for research on precipitation for radio wave transmission studies and hydrological research. Due to technological advances it is now possible to use this radar to measure water clouds, whose reflections are much smaller than those of precipitation.

Radar plays a large role in cloud research, as it can measure inside dense clouds, and thus also at the rear cloud surface. The transmitted radio wave can penetrate the entire cloud as just a small portion of the power is scattered or absorbed by clouds. Because DARR is a 9-cm radar, its (back)scatter from cloud particles is very small so it has to be very sensitive, but an advantage is that attenuation can be ignored.

Lidar is another instrument much used in cloud research and it uses the same physical principles as radar. Lidar, however, transmits a light pulse (from UV to infrared) instead of a radio wave. Just as the human eye, this instrument can often only observe the front of the cloud as its signal interacts strongly with the droplets and is thus heavy attenuated. One of the lidars used is shown in Fig. 1.2. More background information on these instruments is given in sections 2.2 and 2.3.

1.4 Scattering of radio waves

Radio waves can be scattered by either air molecules or particles, and the scattering can be incoherent (randomly distributed scatterers) or coherent (spatial structures in the distribution). Thus there are four possible scattering mechanisms: incoherent air scattering, coherent air scattering, incoherent particle scattering, and coherent particle scattering. Incoherent air scattering is insignificant for radar because molecules are too small compared to the radar wavelength.

Coherent air scatter is caused by spatial variations in the refractive index of atmospheric gases. This type of scatter is often called Clear-air scatter or Bragg scatter. In this thesis it will be called coherent air scatter. Coherent air scatter is normally dominated by spatial variations in humidity, but also variations in temperature and pressure can play a role, as well as the co-variances between these three variables [Gossard and Strauch, 1980]. Coherent air scatter occurs mainly in radar measurements using a long wavelength (cm-waves or longer).

Incoherent particle scatter comes from particles (e.g. cloud droplets) which are randomly distributed within the radar volume. For small particles it is normally called Rayleigh scatter, for larger ones Mie scatter. Incoherent particle scatter is most important for atmospheric radars with a small wavelength. For the retrievals of cloud properties using quantitative radar reflectivities it is normally assumed that the radar scattering by particles is incoherent; in this case the reflected power of the particles can be summed to get the reflected power of all particles.

Spatial variations in the mass concentration of particles can cause *coherent particle scattering* in a way similar to that of coherent air scattering. In clouds this coherent particle scattering by spatial structures in the liquid water content was long thought to be insignificant. Gossard (1979) has calculated that in a cloud, coherent air scattering should be 30 times as strong as coherent droplet scattering. However, Gossard based this theory on the explicit assumption that the spatial variations of liquid water and humidity are about equal; this is probably not true for real clouds, e.g. due to entrainment. Furthermore, his implicit assumption that the distribution of the variations over the spatial scales is similar may not be valid either. This thesis will make plausible that coherent particle scattering can be significant and that it can largely explain the correlation observed in the dual-frequency radar measurements of developing cumulus clouds performed by Knight and Miller (1998) and measurements of a smoke plume by Rogers and Brown (1997).

1.5 Retrievals of cloud properties

At the start of the CLARA project the main idea behind co-locating the instruments was to be able to compare and validate their results. We wanted to answer questions as, for example, to what extent does DARR detect clouds that the lidar misses and vice versa, and how well do the cloud base heights of radar and lidar correspond. During the research we found that a combination of instruments considerably improves the quality of the retrievals of cloud properties. The AWATER project (a subproject of CLARA) already aimed at achieving sensory synergy by combining a radar with a microwave radiometer to measure liquid water content profiles [Erkelens et al., 1998]. The theme of sensor synergy by means of different combinations of instruments became more and more important in the data analysis phase of CLARA, as can be seen in the studies of Boers et al (2000), Erkelens et al. (1999), De Wit et al. (1999), Donovan et al. (1999) and Bloemink et al. (1999).

Many different methods to estimate the cloud liquid water content exist, see section 3.4. In these retrievals there are two crucial parameters that radar can deliver: the cloud boundaries [Boers et al., 2000] and the quantitative radar reflectivity profiles [Frisch et al., 1998; Löhnert et al., 1999]. Furthermore, these retrievals assume that the radio wave is reflected by incoherent particle scatter.

In view of the requirements of these retrieval methods our main research aim can therefore be rephrased as *improving (our understanding of) radar measurements of clouds in order to obtain the height of the cloud top and base and the quantitative radar reflectivity profiles.*

To perform quantitative radar measurements that are reliable we must have a clear insight in the radar, its data processing and the scattering of radio waves by clouds. In all areas good progress has been made during the PhD project. This thesis con-

tains new research results on spectral radar data processing (chapter 4), scattering of radio waves by spatial structures in clouds (chapter 5 and 6), and on combining active instruments to measure the melting layer and the cloud boundaries (chapter 7 and 8). These areas are now understood much better. It is expected that this will eventually lead to improved measurements of the liquid water content and the cloud boundary height.

1.6 This thesis

The instruments used in the CLARA measurement campaigns are discussed in *chapter 2*. The principles of the instruments that are most important for this thesis are given together with a basic explanation of their possibilities for cloud research. The main purpose of this chapter is to provide technical background knowledge for cloud researchers who have little experimental background.

Chapter 3 is for readers who want to know more about clouds, cloud measurements and retrievals of cloud properties. This chapter also includes non-cloud phenomena present in the radar data that are important for understanding the cloud measurements, such as precipitation, clear-air scatter and system artefacts. A section on retrievals is included to explain what measurement techniques are needed for the estimation of cloud properties.

The radar data processing has to be robust, sensitive and accurate. For that reason *chapter 4* investigates the influence of the radar data processing on the measured radar reflectivity. The spectral processing method that we used, clipping, increases the sensitivity of DARR for clouds. This principle has been used before to improve the estimated velocity and width of the spectrum [Sirmans and Bumgarner, 1975; Gordon, 1995]. In this thesis clipping has been used to estimate the radar reflectivity. Maybe this has not been done before because quantitative values of the measured radar reflectivities can decrease drastically as a result of this method, which can lead to a large measurement error, especially for the signals with a low signal-to-noise ratio coming from clouds. Therefore we developed a method to correct the measured reflectivities for this clipping effect using *a-priori* knowledge about the statistical properties of the cloud reflections. This chapter is similar to Venema et al. (1999).

For the retrievals using quantitative radar reflectivities it is normally assumed that the radar scattering is incoherent particle scatter. As DARR sometimes receives reflections from spatial humidity variations in the boundary layer, there was some concern that (part of) the reflections from clouds were not caused by incoherent particle scatter, but by coherent air scatter. We will show that apart from these scattering

mechanisms also coherent particle scattering by cloud structures has to be taken into account.

By deriving a new formulation for coherent particle scatter as a function of measurable variables in *chapter 5* it will be shown that in S-band radar measurements of cumulus clouds the coherent particle scatter (by cloud structures) can dominate the incoherent particle scatter. Recent unexplained dual-frequency measurements of cumulus clouds (and smoke) can largely be explained with this formulation. Chapter 5 is based on Erkelens et al. (2000).

Chapter 6 continues the theme of coherent particle scatter by looking at its importance for radar measurements of various cloud types. New material in this chapter is the calculation of the strength of coherent particle scatter for various clouds and atmospheric conditions. Combining in-situ measurements with these calculations leads to the new finding that coherent particle scatter can be expected to be important in (cm-wave) radar measurements of stratocumulus clouds. Another new finding is the understanding that the radar reflectivity by humidity and liquid water structures depends very much on the distribution of these structures over spatial scales. For the typical case of the CLARA campaigns, S-band radar measurements of stratocumulus, coherent (particle or air) scattering can dominate over incoherent particle scattering. Chapter 6 is based on Venema et al. (2000a).

The measurement of cloud boundaries is not only directly important for climate studies, but also for some algorithms for retrieving microphysical cloud properties [Boers et al., 2000; Crewell et al., 1999]. That is why in *chapter 7* measurements of cloud boundaries are discussed that are carried out with radar and lidar. As for climate studies long-term continuous measurements are necessary, the chapter focuses on identifying situations where the measurements are not yet possible or not reliable. It is found that for reliable measurements the combination of lidar and radar is indispensable; either instrument by itself is often incapable of getting good results. Radar is typically best at measuring the cloud top, and lidar at measuring the cloud base.

Fox and Illingworth (1997) showed the importance of large droplets for radar cloud measurements of the LWC. This chapter stresses that due to the large ice particles also radar cloud boundary height measurements in the presence of (ice) precipitation, virga and in many kinds of ice clouds can be a problem. Furthermore, it argues that it may be difficult to interpret lidar measurements due to specular reflections in ice clouds. Based on case studies, suggestions are given for new measurement techniques that will lead to an increase in the number of situations in which the cloud boundary measurements are reliable. This chapter is based on Venema et al. (2000c).

In *chapter 8* radar and lidar measurements of the melting layer of precipitation are analysed. This layer, in which ice melts into rain, typically gives high radar reflections and is therefore called the bright band. Lidar reflections in the melting layer, on the other hand, are lower than those of its environs; hence the name lidar dark band [Sassen and Chen, 1995]. Based on the new insight gained by the analysis of the measurements some old explanations of the lidar dark band can be rejected. New hypotheses that can explain the dark band have been put forward. Chapter 8 is based on Venema et al. (2000b).

A general overview of the results of the work is presented in *chapter 9*. Furthermore, recommendations are given for further radar cloud research.

Reference

Bloemink, H.I., A.C.A.P. van Lammeren, A.J. Feijt, and S.C.H.M. Jongen. Active-passive sensor synergy for cloud observation: IR cloud properties and cloud liquid water. *Proc. Remote sensing of cloud parameters: retrieval and validation*, IRCTR, Delft, The Netherlands, pp. 113-118, ISBN: 90-804551-6-4, 21-22 Oct., 1999.

Boers, R, H.W.J. Russchenberg, J.S. Erkelens, V.K.C. Venema, A.C.A.P. Van Lammeren, A. Apituley, and S. Jongen. Ground-based remote sensing of stratocumulus properties during CLARA-1996. *J. Appl. Meteorol.*, **39**, no. 2, pp. 169–181, 2000.

Crewell, S., U. Löhnert, and C. Simmer. Remote sensing of liquid water profiles using microwave radiometry. *Proc. Remote sensing of cloud parameters: retrieval and validation*, IRCTR, Delft, The Netherlands, pp. 45-50, ISBN: 90-804551-6-4, 21-22 Oct., 1999.

Donovan, D.P., A.C.A.P. van Lammeren, and H.W.J. Russchenberg. Cloud effective radius and water contents inferred from combined lidar and radar observations during CLARA. *Proc. Remote sensing of cloud parameters: retrieval and validation*, IRCTR, Delft, The Netherlands, pp. 89-94, ISBN: 90-804551-6-4, 21-22 Oct., 1999.

Erkelens, J.S., H.W.J. Russchenberg, S.C.H.M. Jongen, and M.H.A.J. Herben. Combining radar and microwave radiometer for cloud liquid water retrieval. *Proc. 28th European Microwave Conf.*, Amsterdam, The Netherlands, **2**, pp. 67-72, 1998.

Erkelens, J.S., S.C.H.M. Jongen, H.W.J. Russchenberg, and M.H.A.J. Herben. Estimation of Cloud Droplet Concentration from Radar, Lidar and Microwave Radiometer Measurements. *Proc. Remote sensing of cloud parameters: retrieval and validation*, IRCTR, Delft, The Netherlands, pp. 107-111, ISBN: 90-804551-6-4, 21-22 Oct., 1999.

Erkelens, Jan, Victor Venema, Herman Russchenberg, and Læo Ligthart.Coherent scattering of microwaves by particles; Evidence from clouds and smoke. *Journal of the Atmospheric Sciences*, in press, 2000.

Fox, N.I., and A.J. Illingworth. The potential of a spaceborne cloud radar for the detection of stratocumulus clouds. *J. Appl. Meteorol.*, **36**, no. 6, pp. 676-687, 1997.

Frisch, A.S., G. Feingold, C.W. Fairall, T. Uttal, and J.B. Snider. On cloud radar and microwave radiometer measurements of stratus cloud liquid water profiles. *J. Geophys. Res.*, **103**, no. D18, pp. 23195-23197, 1998.

Gage, K.S., C.R. Williams, W.L. Ecklund, and P.E. Johnston. Use of two profilers during MCTEX for unambiguous identification of Bragg scattering and Rayleigh scattering. *J. Atmos. Sci.*, **56**, pp. 3679-3691, 1999.

Gordon, W.B.. Estimation of Doppler parameters using a thressholding technique. *27th Conf. on radar meteorol.*, pp. 753-755, 1995.

Gossard, E.E. A fresh look at the radar reflectivity of clouds. *Radio Sci.*, **14**, pp. 1089-1097, 1979.

Gossard, E.E., and R.G. Strauch. The Refractive Index Spectra within Clouds from Forward-Scatter Radar Observations. *J. Atmos. Sci.*, **20**, pp. 170-183, 1981.

Kattenberg, A. et al., in *Climate Change 1995,* J.T. Houghton et al., Eds. (Cambridge University Press, Cambridge), chap. 6, 1996.

Löhnert, U., S. Crewell, and C. Simmer. Combining a Cloud Radar, a Passive Microwave Radiometer and a Cloud Model to Obtain Cloud Liquid Water. *Proc. Remote sensing of cloud parameters: retrieval and validation*, IRCTR, Delft, The Netherlands, pp. 101-106, ISBN: 90-804551-6-4, 21-22 Oct., 1999.

Platt, C.M.R., N.L. Abshire, and G.T. McNice. Some Microphysical Properties of an Ice Cloud from Lidar Observations of Horizontally Oriented Crystals. *J. Appl. Meteorol.*, **17**, pp. 1220-1224, 1970.

Rogers, R.R., and W.O.J. Brown. Radar observations of a major industrial fire. *Bull. Am. Met. Soc.*, **78**, no. 5, pp. 802-814, 1997.

Sassen, K., and T. Chen. The lidar dark band: An oddity of the radar bright band analogy, *Geoph. Res. Lett.*, **22**, no. 24, pp. 3505-3508, 1995.

Sirmans, D., and B. Bumgarner. Numerical Comparison of Five Mean Frequency Estimators. *J. Appl. Meteorol.*, **14**, Sept., pp. 991-1003, 1975.

Thomas, L., Cartwright, J.C., and Wareing, D.P. Lidar observations of the horizontal orientation of ice crystals in cirrus clouds. *Tellus*, **42B**, pp. 211-216, 1990.

Van Lammeren, A., A. Feijt, D. Donovan, H. Bloemink, H.W.J. Russchenberg, V.K.C. Venema, J.S. Erkelens, A. Apituley, H. Ten Brink, A. Khystov, S. Jongen, G. Brussaard, and M. Herben. *Clouds and radiation: intensive experimental study of clouds and radiation in the Netherlands (CLARA)* Proc. Symposium Remote Sensing of Cloud Parameters: Retrieval and Validation, pp. 5-10, 21-22 October Delft, The Netherlands, 1999.

Venema, V., H. Russchenberg, and L. Ligthart. Correction for clipping of Doppler spectra from clouds and other atmospheric targets. *Proc. Igarss99*, June 28-July 2, Hamburg, Germany, pp. 1180-1183, 1999.

Venema, Victor, Jan Erkelens, Herman Russchenberg, and Leo Ligthart. The contribution of coherent particle scattering to the reflections of radio waves by clouds. Unpublished, 2000a.

Victor Venema, Herman Russchenberg, Arnoud Apituley, André van Lammeren, Susanne Crewell and Leo Ligthart. Measurements of the melting layer using lidar and radar: the lidar dark band. Unpublished, 2000b.

Venema, V.K.C., H.W.J. Russchenberg, A. Apituley, A. van Lammeren, L.P. Ligthart. Cloud boundary height measurements using lidar and radar. *Physics and Chemistry of the Earth.*, **24**, no. 2, pp. 129-134, 2000c.

Watson, R.T., M.C. Zinyowera, and R.H. Moss (eds.). *Climate Change 1995; Impacts, Adaptations and Mitigation of Climate Change: Scientific-Technical Analyses.* Cambridge University Press, Cambridge, UK, 878 p., ISBN: 0-521-56431-X, 1996.

Wit, J.J.M. de, R.J.P. Baedi, J.S. Erkelens, H.W.J. Russchenberg, and J.P.V. Poiares Baptista. Development of retrieval algorithms of cloud parameters from radar and lidar based on the CLARE'98 data set. *Proc. Symposium Remote Sensing of Cloud Parameters: Retrieval and Validation*, pp. 83-88, 21-22 October Delft, The Netherlands, 1999.

Chapter 2

CLARA and the instrumentation

Abstract. *In this chapter the aim and execution of the CLARA project will be discussed. Furthermore, the basic principles behind the instrumentation used in the CLARA campaigns will be given. The focus is on the instruments used most in this thesis: radar and lidar, but also the microwave radiometer, the infrared radiometer, the radiosondes and the FSSP are discussed.*

2.1 CLARA

The work presented in this thesis was carried out in the framework of CLARA. The acronym CLARA stands for CLouds And RAdiation: an intensive experimental study of clouds and radiation. The main objective of the CLARA campaigns was to increase the understanding of radiative processes in the atmosphere by making high-quality measurements of the micro- and macro-physical cloud properties [Van Lammeren et al., 1999]. The focus was not on the radiative flux measurements, but on the cloud properties that are important for radiative transfer. CLARA started as an initiative of four Dutch institutes: the Royal Dutch Meteorological Institute (KNMI), the International Research Centre for Telecommunications-transmission and Radar (IRCTR) of the Delft University of Technology (TU Delft), the National Institute of Public Health and the Environment (RIVM) and the Netherlands Energy Research Foundation (ECN). Several sub-projects of CLARA were created and related projects joined CLARA to benefit from and contribute to the synergy of the multi-sensor campaigns. In the end 10 institutes were involved.

Table 2.1. Instruments used in the CLARA measurement campaigns.

Instrument	Comments	Quantity
Radar	DARR; 3.3 GHz wavelength	Radar reflectivity, velocity
Lidar	1064 & 532 nm wavelengths	Lidar backscatter
Lidar ceilometer	Vaisala 905 nm wavelength	Lidar backscatter
Infrared radiometer	9.6 - 11.5 μm wavelength band	Cloud base temperature
Microwave radiometer	20; 30 and 3 band at 50 GHz	Liquid water and water vapour column
Radiosondes	Released at 6, 12, and 18 h UT	Temperature, humidity and wind
Meteorological station	South of Delft university campus	Temperature, pressure and wind
Cloud Chamber	At ECN, Petten	Number density CCN
Cloud detection network	Lidar, infrared radiometer, pyranometer at 10 stations.	
FSSP	Mounted on aircraft	Drop size distributions
Satellites	AVHRR, Meteosat, ATSR-2	Cloud images in visible and IR (cloud-top temperature)
GPS		Precipitable water column
Infrared camera	For short periods	Cloud images
Visible camera	Continuous measurement	Cloud images

For the measurement campaigns a large set of instruments was installed in Delft, see Table 2.1 for an overview. On the roof of the electrical engineering building most instruments were gathered close to each other: the lidars, a radar, an infrared radiometer, and a microwave radiometer. The location Delft was chosen because the Delft Atmospheric Research Radar is not movable. There were three campaigns: in spring (April 15 to 27), in summer (August 19 to September 4) and in the autumn (November 18 to December 7). When there were extended fields of water clouds, an aircraft performed in situ measurements of the drop size distributions with an FSSP-100. During the campaigns the images from the AVHRR, Meteosat, and ATSR-2 satellites were collected. The campaigns were all planned in 1996, because this way it could be combined with the KNMI Cloud Detection Network (CDN). This network was set up to study the spatial variability of clouds within a typical climate model grid box (100 by 100 km) and consisted of 10 sites where a Vaisala lidar ceilometer, an infrared radiometer and a pyranometer had been set up.

2.2 Radar

A radar transmits a radio wave and measures the part of the wave that is reflected by a target. The difference between the time the wave is transmitted and received is used to measure the distance of the target. The properties of the reflected wave can be

Table 2.2. Specification of the Delft Atmospheric Research Radar during CLARA.

DARR specifications	
Radar type	FM-CW; linear modulation
Transmitted power	90 W; 100 W in CLARA Spring campaign
Transmitter	Solid state amplifier; TWT in Spring campaign
Receiver noise figure	1 dB; 2.5 dB in Spring campaign
Frequency	3.315 GHz
Wavelength	9.04 cm
Frequency excursion	1-50 MHz; typically 5 or 10 MHz
Sweep time	0.625-640 ms; typically 1.25 or 2.5 ms
Antenna gain	32.7 dB receiver
	40.0 dB transmitter
Antenna beam width	3.0° receiver (Full Width Half Power)
	1.5° transmitter
	1.8° effective (31 mrad)
Antenna diameter	4.28 m transmitter
	2.12 m receiver
Antenna isolation	> 90 dB
Maximum range	0.5-30 km; typically 4 or 8 km
Range resolution	typically 15 or 30 m
Temporal resolution	5.12 s
Sampling frequency	100 kHz
Sensitivity for cloud signal	-27 dBZ at half range

used to infer properties of the target (e.g., its velocity or shape). Because the radar receives the power it transmits itself, it is called an active remote sensing instrument. This section will discuss the scattering of radio waves and the principles of radar.

The radar of the TU Delft used in CLARA is called DARR, Delft Atmospheric Research Radar. It is a rather large instrument; the transmit antenna has a diameter of 4.28 m and the receive antenna is 2.12 m. The antennas have to be this large to get a small beam width of 1.8° while using a wavelength of 9 cm. More specifications of DARR can be found in Table 2.2. The antenna can be steered in any direction, but for the measurements presented in this thesis it always pointed towards the zenith.

The scattering of radio waves by atmospheric targets is discussed in much more detail in the chapters 5 and 6; here just the basic formulations will be given. The strength of the radar reflections from a volume of randomly distributed droplets is given by:

$$\eta = \frac{\pi^5 |K|^2}{\lambda^4} Z = \frac{\pi^5 |K|^2}{\lambda^4} \frac{1}{V} \sum D_i^6 \tag{2.1}$$

with η radar volume reflectivity in [$m^{+2}m^{-3}$], $K = (\varepsilon_r - 1)(\varepsilon_r + 2)^{-1}$, a constant that is determined by the relative permittivity of the particles (ε_r), Z the radar reflectivity factor in [$m^{+6}m^{-3}$], V the radar volume in [m^3], and D the diameter of the droplets in [m]. The constant $|K|^2$ is 0.93 for water and 0.17 for ice for the wavelength of DARR. This type of scattering is called incoherent particle scattering in this thesis. An assumption behind this equation is that the Rayleigh approximation holds, i.e. that the particles are much smaller than the wavelength of the radar. For the 9-cm radar of the TU Delft this is true for all particles considered in this dissertation. It can be seen in Eq. (2.1) that incoherent particle scatter depends greatly on the wavelength of the radar. The backscatter will be stronger for radars using a small wavelength. That is why cloud radars typically use a wavelength in the order of a few millimetres, although it is technologically more difficult to transmit a strong radio wave at these wavelengths. The wavelength of DARR is long for cloud measurements. However, because of its uncommonly high sensitivity DARR is able to observe most clouds. Another interesting feature of incoherent particle scatter is the 6th power dependence on the particle diameter. This means that, e.g., one particle of 100 μm will scatter just as strongly as one million particles of 10 μm.

A radar can also receive reflections from spatial variations in the radio refractive index of the air, called coherent air scattering in this thesis. The pressure, temperature and humidity of the air determine the radio refractive index of the air. In the troposphere this kind of scattering is mainly caused by spatial *variations* in humidity and temperature. The strength of the radar reflectivity per unit volume is given by:

$$\eta = 0.38 C_n^2 \lambda^{-1/3} \tag{2.2}$$

C_n^2 is a measure for the total variance of the spatial refractive index variations. The wavelength dependence of this type of scatter is much less that that of incoherent scatter. This means that coherent air scatter is most important for radars with a long wavelength. Radars using a wavelength of more than 10 cm mostly receive reflections from variations in the lower troposphere. They are used to continuously measure the velocity of the air as a function of height and are called wind profiler.

Cloud droplets can also be described as contributing to the radio refractive index of the atmosphere. Therefore, spatial variations in the amount of cloud liquid water (blobs of droplets and voids) can also cause reflections. This type of scatter is called

coherent particle scatter and is one of the main topics of this thesis. Readers interested in this subject are advised to read chapters 5 and 6.

The radar reflectivity (or the radar cross section) is a property of the radar target itself. One can relate it to the power received by the radar (P_r) by taking into account the system constants; use the radar equation:

$$P_r = \frac{P_t G_t G_r \lambda^2}{(4\pi)^3 r_d^4}\sigma = \frac{P_t G_t G_r \theta_b^2 \Delta r \lambda^2}{\pi^5 512(\ln 2) r_d^2}\eta \qquad (2.3)$$

with P_t the transmitted power in [W], G_t and G_r the gain of the transmitting and receiving antenna, λ the wavelength in [m], r_d the distance between the radar and the target (the range) in [m], σ the radar cross section of the target in [m^2], θ_b the -3dB full beam width in [rad]. The first part of the equation is for a single target, e.g. a bird, insect of plane, the second part applies to a volume with targets, e.g. a cloud, rain or a group of insects. The backscattered power for a point target is inversely proportional to the 4th power of the range, as both the transmitted and the reflected wave are assumed to expand isotropically. That the radar beam is not isotropic is accounted for by the gains (G_t and G_r) of the antennas. If the backscattered power of the target is not isotropic this can be accounted for by an angular dependence of the radar cross section. The radar equation for volume scatterers is inversely proportional to the square of the range because the volume of the radar range cell (and thus the number of targets) increases with the square of the range.

The calibration constants used for the CLARA database were determined by calibration of the separate system components like the output power, the antenna patterns, etc. See Gibbs (1997) for details on this method. With this method the accuracy of the calibration is about 1 dB. The sensitivity of DARR to clouds is about -27 dBZ at half the maximum range. This number, however, also depends slightly on the properties of the target, see chapter 4.

Most radars determine the distance of the target by transmitting a short pulse and measuring which part of the signal is returned as a function of time. This time period can be converted into a distance. The Delft Atmospheric Research Radar, however, operates by the so-called Frequency Modulated Continuous Wave (FM-CW) principle. The FM-CW principle is explained in much more detail in Russchenberg (1992), Ligthart and Sinttruyen (1992) and Skolnik (1981); here just the basic principle and equations from these works will be given.

An FM-CW radar transmits a continuous radio wave, the frequency of which is modulated. When the frequency is increased in a linear fashion, the difference between the transmitted and the received frequency is proportional to the distance of the target (range; r_d). Of course the frequency cannot be increased continuously. Therefore the frequency is modulated in so-called sweeps; it is changed a specific

amount – called the frequency excursion (F) in Hz – in a certain time – called the sweep time (T) in seconds – and this pattern is repeated. One such sweep is comparable to a pulse of a pulse radar. The difference between the transmitted and the received frequency is determined by mixing the two signals; this gives a beat signal with frequency:

$$f_b = \frac{2r_d}{c}\frac{F}{T} \tag{2.4}$$

with f_b the beat frequency in Hz, and c (=3 10^8 m/s) the speed of light. Which proportion of the power comes from a certain distance can be calculated by a discrete Fourier transform on N samples of the real valued beat signal. This transform will result in complex voltages in each of the $N/2$ range cells. The resolution of these range cells is given by:

$$\Delta r = \frac{c}{2F} \tag{2.5}$$

with Δr the range resolution in m. The resolution can easily be changed by changing the frequency excursion. During most of the CLARA campaigns the range resolution was either 15 or 30 m; the number of range cells was 256; the maximum range was thus 3840 m or 7680 m.

The velocity of the target is derived from the phase change that is associated with the movement of the target between the sweeps in a specific range cell. The difference in the two-way path between the radar and a target moving with constant speed (v) for a time Δt is $2v\Delta t$. The phase change that corresponds to this is:

$$\phi_D(t) = 2\pi\frac{2v\Delta t}{\lambda} \tag{2.6}$$

with ϕ_D the phase difference in [rad] between two sweeps, λ the wavelength, and Δt the time difference between two sweeps. As the phase can only be measured within an interval of $(-\pi, \pi]$, there is a maximum velocity, which can be measured unambiguously; this velocity is given by:

$$v_{\max} = \pm\frac{\lambda}{4\Delta t} \tag{2.7}$$

with Δt the time between two sweeps. In practice it is often possible to partially exceed this limit. Look at the change of the velocity as a function of range. If there is a discontinuous jump in the velocity from one range cell to the next, correct this by adding (or subtracting) two times the maximum velocity. *A priori* knowledge of the target is needed to know which range cell contains the right velocity and which one needs to be corrected.

Meteorological targets are composed of multiple scattering centres, which each have their own velocity. For these targets a discrete Fourier transform can be used to calculate a power spectrum. The number of velocity cells calculated in this way is equal to the number of sweeps (complex voltages) that is used to calculate the spectrum. During the CLARA campaigns a triangular sweep pattern was used. The data processing was applied to the upward part of the triangle, while the downward part was ignored. So although the sweep time was 1.25 and 2.5 ms, the Δt was 2.5 and 5 ms. The maximum velocity was thus or ± 9 or ± 4.5 m/s. The number of sweeps used to calculate one power spectrum was 512 or 256 respectively to keep the calculation time of one spectrum the same at 1.28 s and the velocity resolution at 3.5 cm/s.

The data in the CLARA database does not contain all these measured power spectra, as the database would become too large. Instead from these power spectra the moments (total received power, average velocity and spectral width) are calculated and stored. Before the moments are calculated, the reflections from non-atmospheric sources are removed; these reflections are called clutter. The clutter (P_c) is divided into two categories: clutter from sources that move a little (e.g. a tree) and stable clutter. Reflection from ground targets that move a little are removed using a predetermined shape. This shape is an exponential function: $P_c(v)=a\exp(-b|v|)$, where v is the velocity. The constant a is determined by the amount of clutter in the zero velocity cell and b is a fixed value, determined on a day without atmospheric reflections. The stable clutter in the zero velocity cell is completely removed when we make this cell equal to the average of the two neighbouring velocity cells. This simple algorithm is sufficient for DARR because this radar operates in an environment with little clutter; DARR stands atop a 100-m high building.

Before the moments are calculated, the noise is removed by means of a clipping algorithm. This method and its consequences are treated in chapter 4.

2.3 Lidar

The physical principles of lidar are similar to those of radar, although the technologies involved are very different. The main difference is the use of laser light instead of microwaves. Lasers emitting light in the ultraviolet, visible light, near-infrared and infrared range are used. The energy in one pulse (E) of a pulse lidar is:

$$E = \Delta t P_0 \tag{2.8}$$

with Δt the pulse duration and P_0 the average pulse power. The received power $P_r(x)$ as a function of the range (r_d) is given by [Weitkamp, 1996]:

$$P_r(r_d) = P_0 \frac{c\Delta t}{2} \frac{A\eta}{r_d^2} \beta(\lambda, r_d)\tau^2(\lambda, r_d) \tag{2.9}$$

Table 2.3. Specifications of the High Temporal Resolution Lidar during CLARA.

Specifications HTRL-lidar	
Lidar type	Elastic backscatter lidar; wide FOV
Transmitted power pulse	0.3 J
Emitter	pulsed Nd:YAG laser
Wavelength	1064 nm fundamental; 532 harmonic
Beam width emitter	0.029° (0.5 mrad)
Maximum range CLARA database	6750 m
Pulse duration	10 ns
Sample rate	20 or 100 MHz
Range resolution	1.5 or 7.5 m
Temporal resolution	1.6 Hz stored

Table 2.4. Specifications of the Vaisala CT-75K lidar ceilometer.

Specifications Vaisala lidar ceilometer	
Lidar type	Elastic backscatter lidar; single lens
Transmitted power pulse	1.6 mJ
Pulse repetition rate	5.1 kHz
Emitter	Pulsed diode, InGaAs MOCVD laser
Wavelength	905 nm
Beam width	0.038° (0.66 mrad)
Range resolution	15 or 30 m
Averaging time	12 s (and after this 18 s of processing)
Temporal resolution	30 s

with c the speed of light, A the area of the detector, η the efficiency of the detector, β the backscatter coefficient, λ the wavelength, and τ the transmittance (see Eq. (2.10)). The backscatter by waterdroplets is on average proportional to their area.

The interaction between the laser light and the clouds is very strong, i.e. like the naked eye, the lidar often only detects the outside of the cloud, not the inside, as here all laser power has already been scattered. The strong extinction of the lidar signal by clouds is accounted for in Eq. (2.9) by the transmittance [Weitkamp, 1996]:

$$\tau(\lambda, r_d) = \exp\left(-\int_0^{r_d} \alpha(\lambda, \xi) d\xi \right) \tag{2.10}$$

with α the extinction coefficient. In case of full extinction the transmittance is zero. The transmittance is squared in Eq. (2.9) as it affects both the transmitted and the scattered light.

During CLARA two different near-infrared backscatter lidar systems were used: the RIVM-High Temporal Resolution Lidar (HTRL-lidar, see Table 2.3) and the Vaisala CT-75K lidar ceilometer (see Table 2.4). The Vaisala is a commercial system made for operational use at airports, and has a range resolution of 30 m.

The HTRL system stores the single-shot returns at a rate of 1.6 Hz and the lidar has a range resolution of either 1.5 or 7.5 m. In the CLARA autumn campaign this lidar used two wavelengths (near infrared and green). More information on the HTRL system can be found in Apituley et al. (2000). All lidar backscatter profiles presented in this thesis are in a range-corrected arbitrary dB scale.

2.4 Other instruments

A microwave radiometer measures the power of the radio waves from of the atmosphere. Radio waves are absorbed and emitted by water vapour, liquid water and oxygen. The strength of these interactions depends on the temperature of the atmospheric layer and the wavelength. Typical frequencies used in microwave radiometry are 20, 30, 50 and 90 GHz. Around 20 GHz water vapour causes a peak in the radio wave extinction; and 50 GHz is in the tail of the 60 GHz oxygen peak. The 30 and 90 GHz band are outside these peaks and are relatively sensitive to liquid water. Microwave radiometry is by far the most accurate remote sensing method to measure the liquid water path (the total amount of water in a column) of the atmosphere [Crewell et al., 1999].

Many retrieval algorithms that relate the received power to the liquid water path are available. The accuracy ranges between 8 and 30 gr m^{-2} and depends on the radiometer frequencies and the extra information on the distribution of the water from other instruments, e.g. lidar, radar, and infrared radiometers [Löhnert et al., 1999; Crewell et al., 1999]. This information on the distribution of liquid water with height is important due to the temperature dependence of the extinction. Combining a microwave radiometer with other instruments makes it possible to estimate the liquid water content, droplet number density, and droplet size, see section 3.4.

During CLARA a microwave radiometer was operated in the framework of the sub-project AWATER, a co-operation between the IRCTR and the Technical Univer-

Table 2.5. Aeroplane flights during CLARA.

Julian day	Date	Time UTC
110	April 19	6 - 09
114	April 23	8 - 11
117	April 26	7 - 10
234	Aug 21	15 - 16
236	Aug 23	08 - 11
238	Aug 25	05 - 08
242	Aug 29	06 - 08
243	Aug 30	08 - 11
245	Sep 01	11 - 15
248	Sep 04	06 - 09
330	Nov 25	15 - 16
331	Nov 26	12 - 14
336	Dec 01	11 - 14
342	Dec 03	07 - 10
342	Dec 07	07 - 11
342	Dec 07	13 - 16

sity of Eindhoven. The radiometer had channels at 21.3, 31.7, 51.85, 53.85, 54.85 GHz [Jongen et al., 1999].

The physical principles behind the infrared radiometer are very similar to those of the above-mentioned microwave radiometer. It also measures the radiation coming from the atmosphere, but at a wavelength band of 9.6 to 11.5 μm. The emissivity of clouds in this wavelength band is nearly unity for clouds with a liquid water path above 50 gr/m^2 [Bloemink et al., 1999]. This means that for these clouds the readings from the infrared radiometer are a measure for the temperature of the cloud base. If the emissivity is below one, the infrared radiometer can be used to estimate the liquid water path.

The IR-radiometer operated in the CLARA campaigns was an IR radiation pyrometer, lens system K6 from Heimann Optoelectronics, with an opening angle of 50 mrad. The system has an averaging time of 1 s and a temperature resolution of 0.5 °C.

Radiosondes carry out in situ measurements of the temperature, humidity and pressure; they hang under a balloon that is slowly ascending. Normally the balloon bursts at a height between 10 and 20 km. Radiosondes derive their name from the way their position is determined: by radio links with a number of ground stations. From position of the radiosonde the wind speed and direction are derived. From the air pressure the height of the instrument is calculated. A difficulty of using the radiosonde together with the remote sensing instruments is that the radiosonde can drift very far from the launching position; up to 200 km. The radiosondes launched in Delft can, for example, land in Germany with their parachutes.

The radiosondes were released at a field one kilometre south of the electrical engineering building, where most remote sensing instruments were located. At this field the ground values of the temperature, humidity and air pressure were monitored continuously by a meteostation, and one Vaisala lidar ceilometer was located at this field.

Radiosondes from Vaisala were used. Their accuracy is in the order of 1 °C in temperature, 10 % in relative humidity, 0.5 m/s in wind speed and about 2 degrees in wind direction.

During days when the weather prediction was favourable, i.e. when the KNMI predicted extended fields of water clouds, an aircraft performed in situ measurements of the drop size distributions with an FSSP-100. See Table 2.5 for an overview of the flights. The analysis of the CLARA data focused on these days.

The drop size distribution was measured using a Forward Scattering Spectroscope Probe, FSSP [Brenguier et al., 1994]. This instrument illuminates the droplets in its measurement volume. The amount of light scattered in the forward direction is used as a measure for the size of the droplet. One drop size distribution is typically calculated from a total sampled volume of about 20 cm^3. For this reason, the volume may not be representative for the volume measured by the remote sensing instruments. An occasional large drop may be missed, for instance, by the FSSP. Furthermore, the maximum drop size the FSSP can measure is 47 μm.

The flights took place above the area of Delft when possible or Petten (because a cloud chamber was located there), but the airways are busy in these areas and cloud prediction not always accurate, so sometimes flights had to take place elsewhere. Furthermore, mainly horizontal lags were flown. This is a good basis for comparisons with satellite measurements, but not for comparisons with data of profiling remote sensing instruments.

2.5 Concluding remarks

The CLARA campaigns provided a high-quality data set that are useful for studying the properties of clouds and for developing and testing new retrieval techniques, especially techniques that combine the data from more than one sensor. All measured data is available in a free, public database as a facility for cloud research. More information on this and on CLARA in general can be found on the internet at: http://www.knmi.nl/CLARA/; information about the contribution of IRCTR is found on: http://irctr.et.tudelft.nl/projects/clara/.

References

Apituley, A., A. van Lammeren, and H.W.J. Russchenberg. High time resolution cloud measurements with lidar during CLARA. *Phys. Chem. Earth (B)*, **24**, no. 2, pp. 107-114, 2000.

Bloemink, H.I., A.C.A.P. van Lammeren, A.J. Feijt, and S.C.H.M. Jongen. Active passive sensor synergy for cloud observations; IR cloud properties and cloud liquid water. *Proc. Remote sensing of cloud parameters: retrieval and validation*, IRCTR, Delft, The Netherlands, pp. 113-117, ISBN: 90-804551-6-4, 21-22 Oct., 1999.

Brenguier J.L., D. Baumgardner, and B. Baker. A review and discussion of processing algorithms for FSSP concentration measurements. *J. of atmos. and oceanic technol.*, **11**, no. 5, pp. 1409-1414, Oct., 1994.

Crewell, S., U. Löhnert, and C. Simmer. Remote sensing of liquid water profiles using microwave radiometry. *Proc. Remote sensing of cloud parameters: retrieval and validation*, IRCTR, Delft, The Netherlands, pp. 45-50, ISBN: 90-804551-6-4, 21-22 Oct., 1999.

Gibbs, A.P.R. *A comparative study of reflectivity and liquid water content of stratocumulus and cumulus clouds using radar and FSSP measurements.* IRCTR-master's thesis no. 68-220-A254-97, 105 p., 1997.

Jongen, S.C.H.M., G. Brussaard, and M.H.A.J. Herben. Atmospheric water vapour, liquid water and temperature profile retrieval using 20/30/50 GHz radiometer data. *Proc. Remote sensing of cloud parameters: retrieval and validation*, IRCTR, Delft, The Netherlands, pp. 39-43, ISBN: 90-804551-6-4, 21-22 Oct., 1999.

Ligthart, L.P., and J.S. van Sinttruyen. FM-CW radar polarimetry. *Direct and inverse methods in radar polarimetry, part 2*, W.-M Bourner et al. (eds.), pp. 1625-1657, 1992.

Russchenberg, H.W.J. *Ground-based remote sensing of precipitation using a multi-polarized FM-CW Doppler radar.* PhD dissertation, Delft University Press, Delft, The Netherlands, 206 p., ISBN: 90-6275-823-1, 1992.

Skolnik, M.I. *Introduction to radar systems; second edition.* McGraw-Hill, Singapore, 581 p., ISBN: 0-07-066572-9, 1981.

Van Lammeren, A., A. Feijt, D. Donovan, H. Bloemink, H.W.J. Russchenberg, V.K.C. Venema, J.S. Erkelens, A. Apituley, H. Ten Brink, A. Khystov, S. Jongen, G. Brussaard, and M. Herben. *Clouds and radiation: intensive experimental study of clouds and radiation in the Netherlands (CLARA)* Proc. Symposium Remote Sensing of Cloud Parameters: Retrieval and Validation, pp. 5-10, 21-22 October Delft, The Netherlands, 1999.

Weitkamp, C. Lidar Measurements: Atmospheric Constituents, Clouds, and Ground Reflectance. Chapter 10 in *Radiation and Water in the Climate system: Remote Measurements.* E. Raschke (ed.), Springer-Verlag, Berlin, Germany, 1996.

Chapter 3

The atmosphere: phenomena, measurements and retrievals

Abstract. *This chapter provides some background material on the atmosphere for the non-meteorologist, and gives some examples of what can be measured in the atmosphere. We focus on radar measurements of clouds and precipitation, but coherent air scatter and some system effects are discussed as well as these can be mistaken for cloud reflections. The chapter finishes by reviewing briefly the proposed methods that use remote sensing instruments for the retrieval of cloud properties; this gives some insight into what kind of measurement techniques are necessary for high-quality retrievals.*

3.1 Climate change and clouds

Mankind is changing the climate on earth. The average temperature of the earth's surface is rising and further climate change is predicted for the future. In an average scenario the temperature has risen about 1 to 3.5 degrees by 2100 [Watson et al., 1996]. This will have many consequences for human society. Likely results are: more violent storms, increase in incidence of extremely high temperatures, droughts, but also floods, fires, outbreaks of pests, sea level rise, increase of the incidence of tropical diseases, and reduction of the biodiversity. Human health, terrestrial, aquatic, ecological and socio-economic systems (e.g. agriculture and water resources) are all sensitive to climatic change [Watson et al., 1996].

A large source of uncertainty in the predictions of the future climate is the reaction of the cloud system to climate change. The cloud feedback is the largest source

of uncertainties in the climate-change calculations of current climate models [Kattenberg et al., 1996].

The influence of clouds on the radiative transfer through the atmosphere, and thus on our climate, is large. Clouds have a cooling effect: they reflect solar radiation to space, and radiate heat radiation to space. They also have a warming effect because clouds retain heat on the earth's surface. To quantify these effects we must understand the macro and micro cloud properties. Macro physical properties are the height of the cloud base and top, and related to that the thickness (vertical extent) of the cloud, the cloud fraction and the cloud overlap. The cloud fraction is the part of an area that is covered by clouds. In case of two layers with broken clouds it becomes important whether the cloudy fractions of the two layers overlap each other. Important microphysical cloud properties are the phase of the particles (water or ice) and the particle size distribution. The particle size distribution is parameterised in models by the number density, average drop size, width of the drop size distribution, liquid water content, or optical depth. The optical depth is a measure of the amount of radiation that can penetrate the cloud and it is related to the total area of the droplets, phase and cloud structures (bumpiness).

The cloud parameters are important for the radiative transfer, as, for example, a high and hence cold cloud will radiate less heat to space than a low and hence warm cloud. An almost transparent cloud with a low optical depth will reflect less solar radiation to space than a cloud with a high optical depth. A broken cloud will let more radiation through than an even cloud with the same average liquid water content.

These problems form the background of this thesis. By improving cloud measurements, we hope to contribute to a better understanding of the influence of clouds on our changing climate. For an excellent basic treatment of the climate system and climate change, see Graedel and Crutzen (1995) or the Dutch book Crutzen and Graedel (1996). Houghton et al. (1996) give a full scientific review of climate change.

3.2 Phenomena

This section explains the physics of clouds and precipitation as background information for the understanding of remote sensing measurements; it is not intended to be a rigorous scientific treatment. It is limited to these two phenomena as they are important for understanding the radar and lidar measurements that are presented in this thesis.

3.2.1 Clouds

There are many types of clouds. The scientific classification is mainly based on morphology and cloud height. The height classification is used as low clouds typically contain waterdroplets, whereas high clouds contain ice crystals. Midlevel clouds may contain either of these or both. Low clouds with a large horizontal extent are called *stratus clouds* (typical abbreviation: St). When separate clouds are clearly visible that are horizontally not much larger than vertically, they are called *cumulus* (Cu). This can be fair-weather cumulus, which remain small, or cumulonimbus, which can grow into kilometre-high clouds. Between cumulus and stratus cloud, we find the stratiform clouds, which have a bumpy character and are called *stratocumulus* (Sc).

Midlevel cloud names begin with 'alto-'. A smooth midlevel cloud is called *altostratus* (As), whereas midlevel clouds with a more bumpy character are called *altocumulus* (Ac); these can occur in large fields. High clouds are called *cirrus* (Ci), and distinctive features are that these look feathery and optically are typically not very thick.

Important cloud types that have not been mentioned yet are: mist (a stratus cloud whose cloud base is found at the surface) and *contrails* (high linear clouds that are created by aeroplanes). If clouds are precipitating this is indicated in the name by 'nimbo'. Thus a raining stratus cloud is called *nimbostratus* (Ns) and a precipitating cumulus, *cumulonimbus*.

The amount of water in a cloud is amazingly small. Large cumulus cloud can have a liquid water content (LWC) of a few grams per cubic metre, depending on the height. The liquid water content of stratus clouds are usually in the range of 0.05 to 0.25 gr/m^3 [Rogers and Yau, 1996]. Compare this to 1000 kg per cubic meter for pure water and one can see that a cloud volume is almost empty.

That clouds are visible at all is due to the high number of droplets. A cumulus cloud can have 500 to 900 droplets per cubic *centimetre* and stratus cloud a few hundred, see table 6.2 in chapter 6. These droplets are very small, typically in the order of 10 µm. Because of the small mass and relatively large area of these drops their gravitational force is very small compared to the frictional force, so the droplets float in the air. Furthermore, because of the small sizes and the high number density of the drops, clouds can combine a low LWC with a high total area, which makes clouds important for the transfer of solar and heat radiation through the atmosphere.

Clouds are formed when the humidity (mass density of water vapour) of the air becomes too great (above 100 % relative humidity). How much water vapour air can contain depends on the air temperature: warm air can contain more water vapour than cold air. Thus the relative humidity can reach values above 100 %, for example, when an air parcel whose humidity levels already approach saturation cools down by being lifted up.

The water will condense on the aerosols. The fraction of the aerosols on which the water condenses are called the Cloud Condensation Nuclei (CCN). Whether an aerosol will become a CCN depends on its composition and on the supersaturation of the humidity. The amount of droplets thus depend on the amount of aerosols, their composition and the supersaturation they are exposed to. As there are on average less aerosols above the ocean than above land, clouds above the ocean tend to have less but bigger droplets, see e.g. the differences in table 6.2 of chapter 6.

Cumulus clouds are formed when warm (and thus light) and humid air lifts. As water starts condensing, heat is generated, which will warm the parcel and can promote further lifting of the parcel to create a very tall cloud. While the cloud grows higher, the size of the droplets increases due to condensation. The smallest particles of a few micrometers are, therefore, found at the base of cumulus clouds, whereas the large particles are found close to the cloud top. In stratocumulus clouds the largest drops are found near the top of the cloud as well, see e.g. Gerber (1996), Martin et al. (1994) and Slingo et al. (1982).

An easy introduction into cloud physics is Rogers and Yau (1996). A more detailed book on clouds (and precipitation), covering mainly physics, is Pruppacher and Klett (1997). Seinfield and Pandis's (1998) introductory book is rather thick, but a good read; it treats the physics and chemistry of the atmosphere with much attention to clouds.

3.2.2 Precipitation

There is just a gradual difference between a cloud droplet and a raindroplet; it is hard to pinpoint a certain drop diameter as a dividing line. An often-used definition for rain is that the drops have to reach the ground. However, precipitation that evaporates before it reaches the ground (virga) has many similarities with precipitation: a high fall velocity, large particles, sometimes a bright band, for instance.

Note, however, that if a cloud drop is to become a raindrop, a considerable increase in volume is needed; a cloud drop is typically 10 μm, whereas a raindrop is 1 mm, so the mass has to grow about a million times as large. Two mechanisms may cause this transformation: the warm, and the cold precipitation process. In the warm rain process, droplets grow initially due to condensation. The critical step from cloud droplet to raindrop is made by coalescence of droplets. The width to the droplet velocity (and size) spectrum is a key variable as collisions are necessary for coalescence. There is some indication that turbulence can promote the aggregation of waterdroplets, for a recent article see Vohl et al. (1999).

In the cold rain process raindrops are produced as water collects on ice crystals. The saturation pressure of water vapour above ice is less than above liquid water, so in a volume containing both ice crystals and waterdroplets, the droplets will evapo-

rate and the ice crystals will grow. There are typically much less ice crystals than waterdroplets. These ice crystals will, therefore, grow large as they absorb the water of the many droplets and will eventually fall out of the cloud. At some height the ice precipitation may melt into raindrops. In stratiform rain the melting will occur at a well-defined height below the zero-degree level. The atmospheric layer in which this happens is called the melting layer, or the bright band because of the high radar reflectivity of the layer.

Roughly we can explain the high reflections in the melting layer by observing that the radar reflectivity in the ice precipitation above the melting layer is lower due to the lower radio refractive index of ice and that the radar reflectivity of the rain below is lower due to the lower number density and the smaller size of the droplets. The bright band combines the high radio refractive index of the rain with the high number density and large size of ice crystals before melting. The melting layer is discussed in much more detail in any of the IRCTR dissertations mentioned in the next paragraph.

Precipitation and the melting layer has been the focus of IRCTR research for a long time, both in polarimetric radar measurements and modelling of radar backscatter and radio wave propagation, see Niemeijer (1996), Russchenberg (1992) and Klaassen (1989). The physics of precipitation is comprehensively treated in Pruppacher and Klett (1997). Doviak and Zrnic (1984) discuss many precipitation-related issues from a radar perspective.

3.3 Atmospheric measurements

3.3.1 Clouds

ALTOSTRATUS

The lidar backscatter from an altostratus cloud between 2 and 5 km is shown in Figure 3.1a. The contour in the figure is the cloud boundary based on the radar reflectivity measured by DARR (see Figure 3.1b). The radar reflectivity, up to –5 dBZ, is much higher than that of a typical stratiform water cloud. So the radar reflections probably mainly come from relatively big ice crystals.

The attenuation of the lidar signal is not very strong during the greatest part of the measurement: there is not much difference between the radar and lidar cloud top height. By comparing the lidar backscatter with the radar contour, one can see, however, that between 21 and 22.5 hrs UT and after 23.5 hrs UT, the lidar signal probably is complete attenuation: The radar estimates the cloud top to be a few hundred meters higher.

Also at the cloud base there is some difference in estimation of the cloud base between the radar and the lidar. The radar cloud base is likely to be lower due to re-

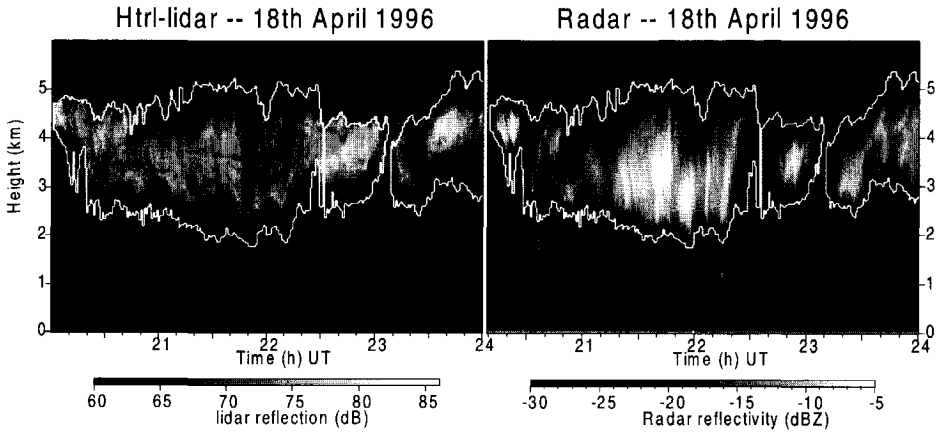

Figure 3.1. Measurement of an altostratus cloud with radar and lidar on the evening of the 18th of April. The contour in both subparts is the cloud boundary as estimated from the radar reflectivity.

flections from a few relatively large ice crystals – with a low optical backscatter – falling out of the cloud. This measurement is discussed in much more detail in chapter 7.

Below 2 kilometres the measurement shows some vertical stripes. These stripes are actually point targets that are smeared out by cross talk from the Fourier trans-

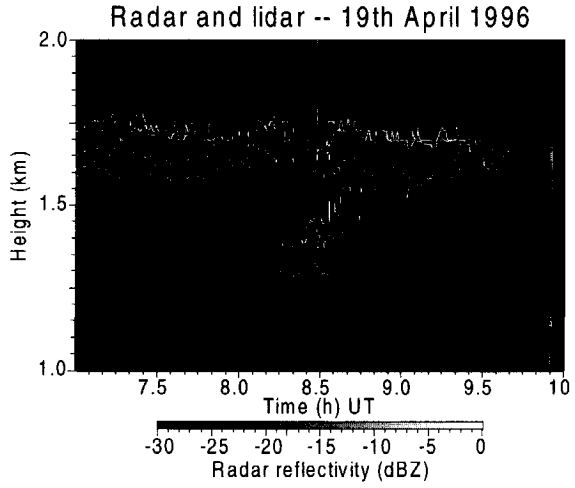

Figure 3.2. Stratocumulus cloud measured using radar and lidar, in the morning of 19th of April 1996. The background of the figure is the radar reflectivity factor measured by DARR and the contours are the range-corrected lidar backscatter given by the Vaisala CT-75K. The contours are 10 dB apart.

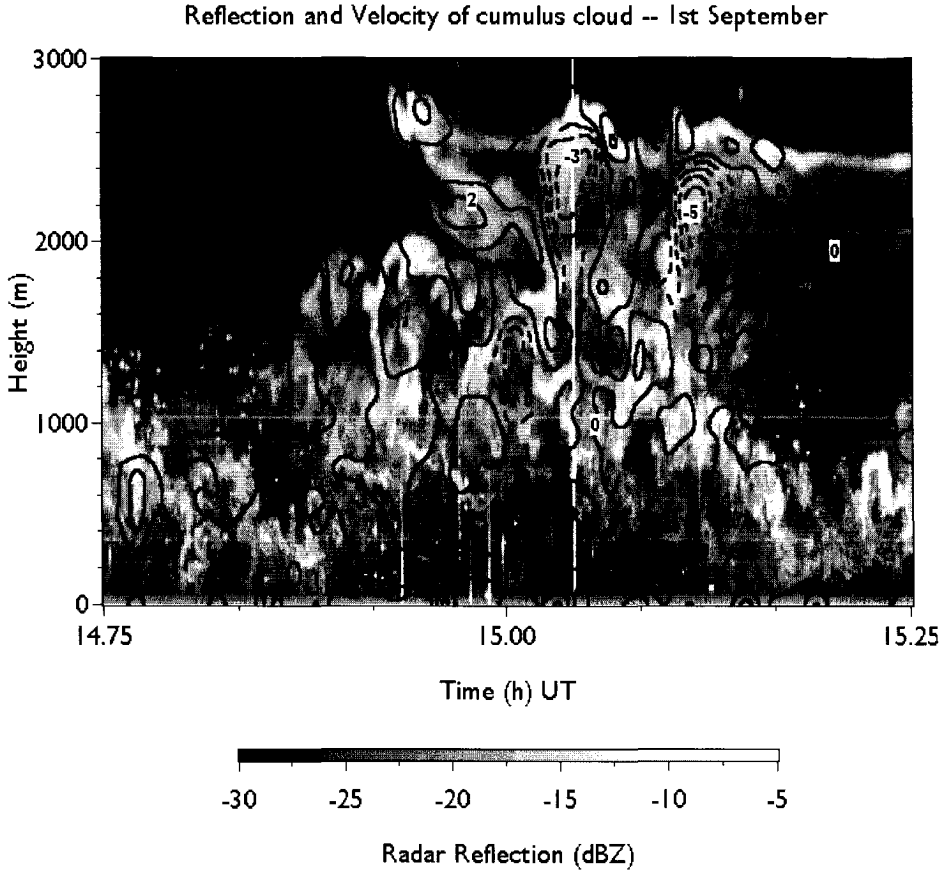

Figure 3.3. Measurement of a cumulus cloud with DARR in the afternoon of 1st of September 1996, showing both radar reflectivity and radar weighted average velocity. The background is the radar reflectivity and the contours indicate the (smoothed) velocity. The contours are 1 m/s apart and the dashed lines indicate negative (upward) velocities.

form in the data processing that converts frequency into range information. The origin of these reflections is not known; for more information on this phenomenon see section 3.3.3 on angels.

STRATOCUMULUS

One CLARA measurement of stratocumulus is shown in Figure 3.2. The background of the figure is the radar reflectivity from DARR and the contours represent the lidar backscatter. The cloud base measured by lidar is about a 100 meters below the first radar signals from DARR. This is because the radar

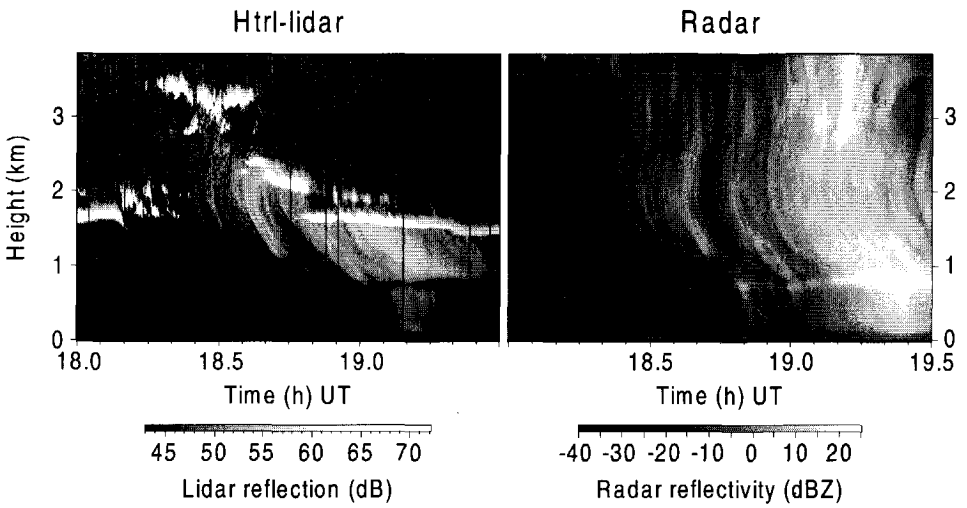

Figure 3.4. Measurement of light precipitation on the 6th of December 1996 during the third CLARA campaign. Figure 3.4a represents the range-corrected lidar backscatter of the HTRL-lidar and Fig. 3.4b the radar reflectivity factor measured by DARR.

reflection from the small droplets (just 10 μm) at cloud base is much too small for DARR. This is typical for water clouds. Based on a simple model of a stratus water cloud, Sassen *et al.* (1999) estimate that a radar with a minimum detectable signal of –30 dBZ will detect the first signals 200 m above the lidar cloud base. The sensitivity of DARR at this height is between –30 and –25 dBZ. This measurement is discussed in more detail in chapter 7 and chapter 6.

CUMULUS

In Figure 3.3 a radar measurement of a cumulus cloud is shown, in particular the dynamical behaviour of this cumulus. The background is the radar reflection, whereas the contours give the velocity as measured by the radar. Two thermal plumes are visible in this cloud, which move up with high speed, up to 5 m/s.

The measurement is analysed in much more detail in Gibbs (1997), who compared this radar measurement with other instruments: lidar, FSSP and microwave radiometer. The lidar measurement shows that many of the radar reflections in the boundary layer are not from clouds. These reflections are due to refractive index variations, see section 3.3.3 on coherent air radar measurements.

The reflections at the top of the cloud are up to –5 dBZ, which is much too high for scatter due to waterdroplets. Most likely this scatter is coherent, and either coherent air scatter or coherent particle scatter, see chapters 5 and 6. The high reflections might also come from large ice crystals.

3.3.2 *Precipitation*

Precipitation gives much larger radar reflections than clouds. The radar reflectivity can be related to the rain intensity. A commonly used relation for this is the Marshall-Palmer relation:

$$Z = 200R^{1.6} \quad (1)$$

with Z the radar reflectivity factor in $mm^6\ m^{-3}$ and R the rain rate in $mm\ hr^{-1}$. This relation was derived for stratiform rain. As the relation is sensitive to the shape of the drop size distribution, different Z–R relations are used for different situations. With the Marshall-Palmer relation a light-rain rate of 1 mm/hr would correspond to 23 dBZ. The radar reflectivity of rain is thus typically much higher than that of clouds, especially stratiform water clouds.

The ability of radar to measure the rain rate is usually exploited in weather radars, which point almost horizontally and scan in azimuth to estimate rainfall over large regions. The stages of the cold rain production process can be studied with a radar that points vertically. An example of this process can be seen in Figure 3.4b between 16:40 and 19:30 hrs UT. The melting layer is visible at about 700 m: the layer with high reflections. Below the melting layer we find the raindrops, whereas above it the precipitation consists of ice crystals.

In the lidar measurement (Fig. 3.4a) one can see three cloud layers (around 1.5, 2.0 and 3.3 km), the lowest of which is well above the melting layer at 700 m. The lidar backscatter in the melting layer is lower than the backscatter in its environs. This lidar dark band is discussed in chapter 8. It is remarkable that the cloud layers from the lidar measurement cannot be detected in the radar reflectivity figure; this is discussed in chapter 7. A temperature profile measured by a radio sonde revealed that the zero-degree level is at 1500 m, so 800 meters above the melting layer.

Concluding, the general outline of the cold rain process is that ice particles are created which melt into rain. The crystals (or snowflakes) fall down and are subject to riming by small particles in the cloud and possibly they aggregate with each other. Below the cloud base the crystals can aggregate further (this is most efficient below the –6 °C level), and may fall through other cloud layers. In the air below the cloud, which is normally subsaturated, the crystals will sublimate and thus moisten and cool the air. When the particles reach the zero-degree level they will not directly start to melt, but first sublimation will continue to cool the crystals and the air. Only when the temperature increases further, the particles will start to melt. At which temperature this will happen will depend on the humidity. The above is a standard situation: sometimes some of these steps may not occur.

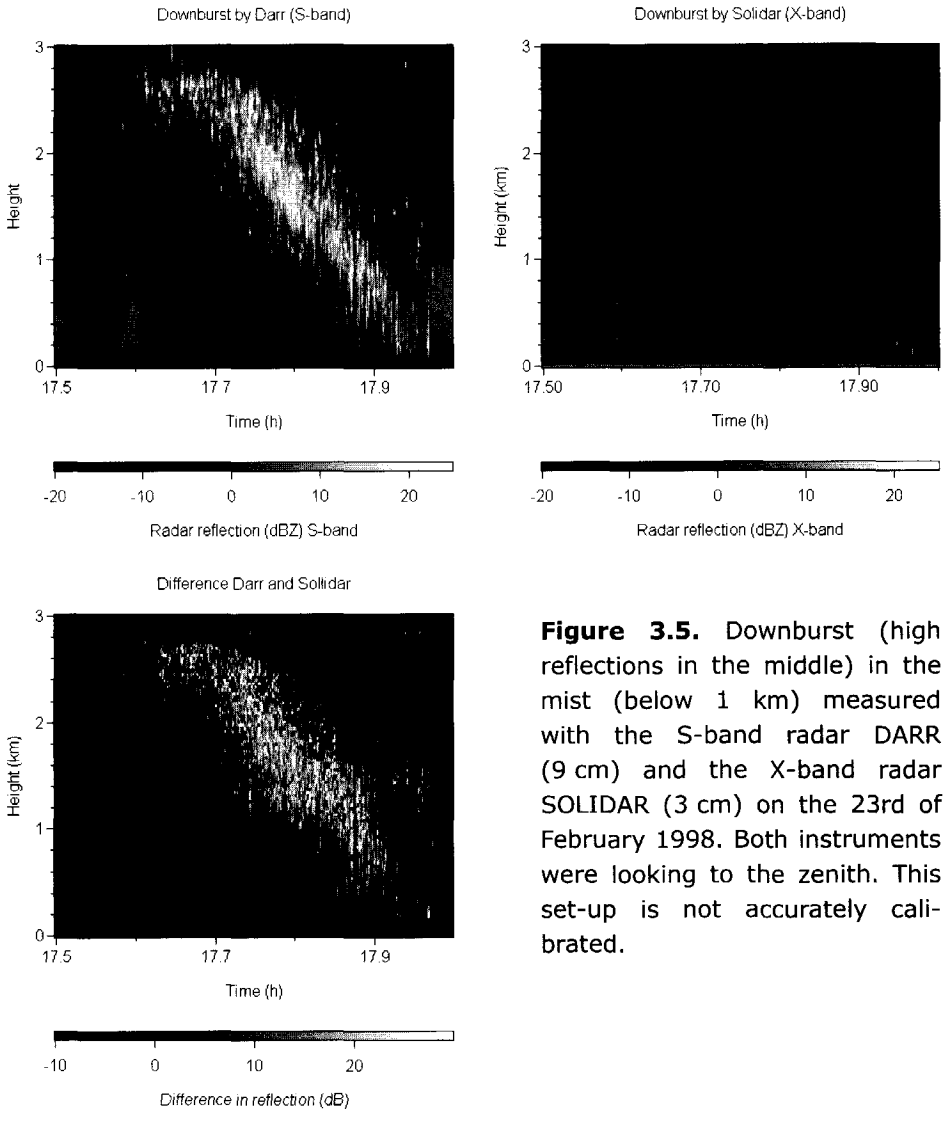

Figure 3.5. Downburst (high reflections in the middle) in the mist (below 1 km) measured with the S-band radar DARR (9 cm) and the X-band radar SOLIDAR (3 cm) on the 23rd of February 1998. Both instruments were looking to the zenith. This set-up is not accurately calibrated.

3.3.3 Coherent air scatter

Air without particles can also reflect radar waves. Sharp gradients in the radio refractive index can cause radar reflections. The humidity, temperature and pressure determine the refractive index of the atmosphere. Traditionally this type of scatter is called 'clear air' scatter. As it can also occur in cloudy air, this name can be a bit con-

fusing. Therefore it is called coherent air scatter in this dissertation. Some examples of coherent air scatter in clear air are given in this section.

Boundary layer coherent air scatter

Boundary layer coherent air scatter is caused by spatial radio refractive index variations. These radio refractive index variations can be compared to the optical refractive index variations that one can see above hot asphalt in summer. The radar reflections in the boundary layer (below 1 km) in Figure 3.3 are a typical example. This type of scatter usually produces beautiful structures.

The origin of this type of scatter is a lot of turbulence in the boundary layer due to solar heating of the surface and wind drag. This is combined with high gradients of humidity and temperature in the boundary layer. Together turbulence and gradients create strong local gradients that act as scattering centres.

Boundary layer coherent air scatter can be important for cloud studies with an S-band radar as it can obscure the presence of clouds in the boundary layer. It would be interesting to study whether it is still possible to do radar cloud measurements in this situation. Maybe the signal statistics can be used. Dual-wavelength radar may be of help in case some part of the signal is incoherent particle scatter.

Downburst

Figure 3.5 of a downburst is an example of the ability of dual-wavelength radar to distinguish between coherent and incoherent scatter. Figure 3.5a is the reflection of DARR, an S-band radar with a wavelength of 9 cm. In the lower 1.2 km of Fig. 3.5 there is some drizzle or mist (velocities from 1.5 to 3.0 m/s downward). In the middle, from 3 km to the ground, one can see a downburst, giving strong reflections with a speckled pattern. Figure 3.5b shows the same event with an X-band radar (SOLIDAR), with a wavelength of 3 cm. Figure 3.5c shows the difference in radar reflection between the two radars. Radar reflections from small Rayleigh particles (expressed in dBZ) should be the same for two radars. This can be seen in the mist layer. The downburst, however, gives reflections which are about 19 dBZ lower. This is about what one would expect for coherent air scatter.

This set-up has not yet been carefully calibrated, which is probably the reason why there is a small difference in reflectivity in the mist. The beam width of both antenna systems is about the same, as is their range and time resolution.

Refractive index gradients

A layer in which the refractive index of the air changes quickly with height can also cause radio wave reflections. No examples in the CLARA database are known of which we can be sure it is a refractive index gradient. They are seen most clearly with radars with longer wavelengths (windprofilers). Layers with refractive index gradients are treacherous as they can be mistaken for a thin cloud layer.

Cohn et al. (1995) reported an intriguing measurement with a UHF profiler: the onset of rain caused an increase of about 10 dB in the reflections from a layer with coherent air scatter from a subsidence inversion and a strong humidity lapse. One

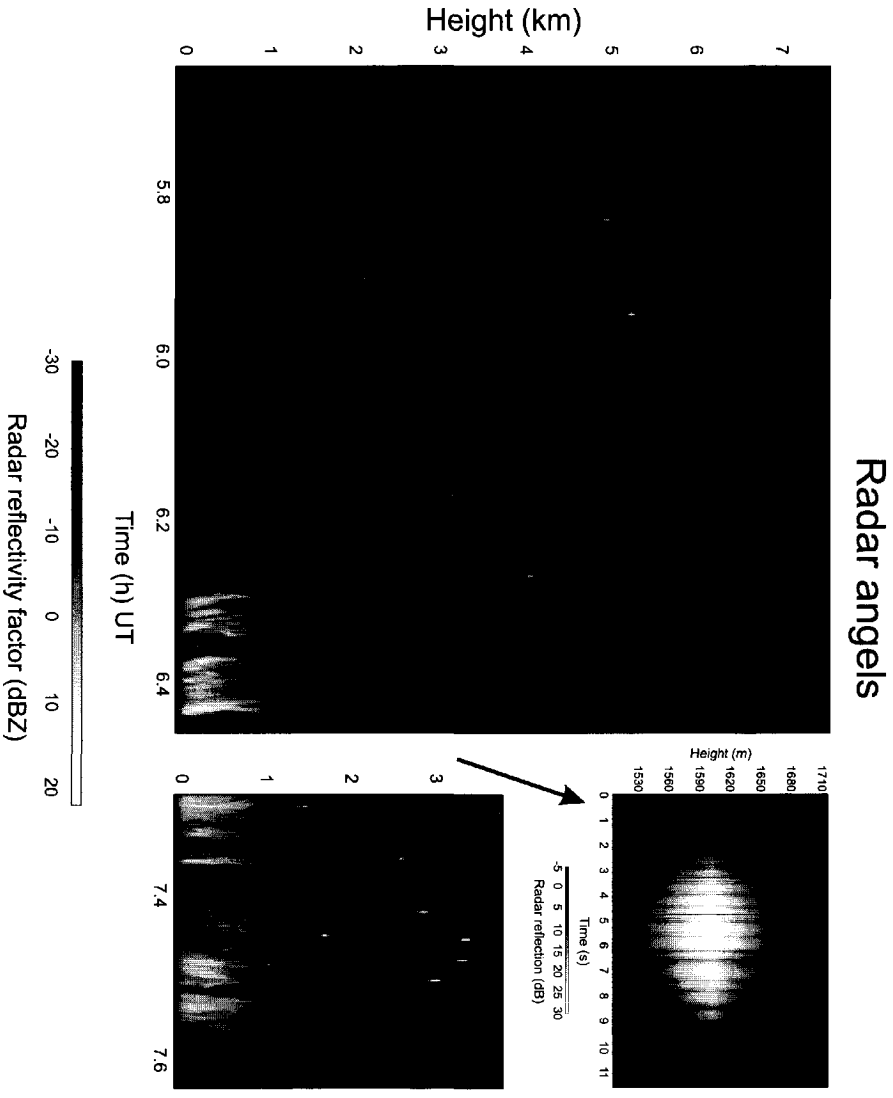

Figure 3.6. Measurement of angels performed with DARR on the 4th of September 1996 in the summer CLARA campaign. The picture at the left and bottom right show the radar reflectivity factor calculated using the standard processing with a temporal resolution of 5.12 s. The high temporal image (top right) has a resolution of 5 ms.

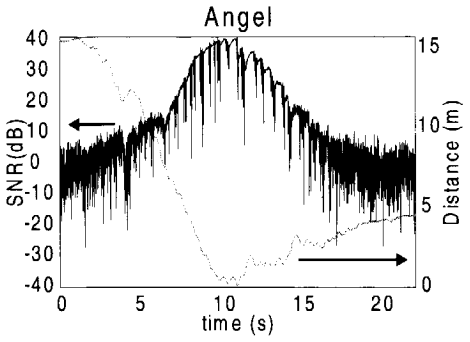

Figure 3.7. Measurement of an angel with DARR. This line graph is made from a cross section of the angel in Fig. 3.6 at 2235 m. The highly fluctuating line is the signal-to-noise ratio of the angel. The smooth grey line is the unwrapped phase of the angel converted into a measure for the relative distance to the radar.

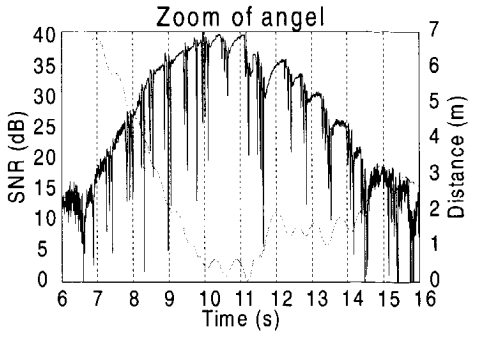

Figure 3.8. Zoom of the angel in Fig. 3.7. The highly fluctuating line is the signal-to-noise ratio of the angel. The smooth grey line is the unwrapped phase of the angel converted into a measure for the relative distance to the radar.

would expect the contrary, however: a decrease of the coherent air reflections (Rogers and Brown, 1998). A possible, though very speculative explanation is that the scatter in the inversion layer does not come from refractive index variations, but is incoherent particle scatter from light debris that is captured in the layer. As the debris becomes wet due to the rain, its refractive index and thus radar backscatter increases, a process similar to snow flakes that melt a little. This hypothesis may be validated by dual-frequency radar measurements.

ANGELS

Radars sometimes observe strong point reflections the origin of which is still unknown. These are called angels, worms, or ghosts, and it is speculated that these reflections are from insects, birds, leaves, atmospheric plankton (anything organic in the air) or spontaneous turbulence [Ottersten, 1970].

Normally angels are seen as small dots (or vertical stripes due to the Fourier transform), e.g. the dots and stripes below the altostratus cloud in Figure 3.1b. This type of angel is shown in more detail in Figure 3.6. The two overview measurements, which were made with the standard processing with a 5-second temporal resolution, show a light-rain event with angels above it.

In between these two measurements, the beat signal of the radar was stored. This detailed measurement (top right) has a time resolution of 5 ms. The time resolution is determined by the sweeps of our FM-CW radar (one sweep is comparable to one

pulse for a pulse radar). The measured thickness of the object is due to the signal processing. This high temporal resolution provides new insight about these angels. An interference pattern is seen in the power and a sinus pattern in the phase.

The pattern in the reflected power (signal-to-noise ratio, SNR) is more obvious in the line graphs of Figures 3.7 and 3.8. These figures also show the unwrapped phase (distance) of the measured signal, which has a sinus pattern. Both line graphs are taken from the range cell at a height of 2235 m. The measured phase was unwrapped, i.e. corrected for 2π jumps by a simple algorithm that compared two consecutive phases and added or subtracted 2π if that would reduce the phase difference. The scattering object is probably a point target. In this case the phase can be converted into a distance (with an arbitrary starting point) as 2π radians is equal to the wavelength of 9 cm.

At the moment the SNR is irregular, the unwrapped phase is at a minimum (after the trend has been removed). The tops of the sinus patterns in the phase correspond to the periods in which the SNR is smoothly increasing. The period of the phase signal is about 0.8 seconds. And after the trend has been removed the maximum amplitude of the unwrapped phase is 0.5 m.

3.3.4 Artefacts

Not all features in the radar images shown in this dissertation correspond to meteorological phenomena. It is important to recognise artefacts in the radar data as they can be mistaken for the meteorological events. To identify and possibly remove these artefacts is especially crucial in automated feature retrievals.

The so-called *disturbance lines* (also called noise lines) are nearly always present, and are caused by the radar system itself [Kaya, 1999]. They can be identified as straight horizontal lines with a reasonably stable SNR, see for example the lines in Figure 3.1 and 2 just above 2 km.

Vertical lines also occur in the radar images. Sometimes they are caused by strong point scatterers that produce lines due to cross talk of the FFT, as in Figure 3.3 at 15.04 hrs UT and twice in Figure 3.2 around 9 hrs UT. Some of the rain measurements in the CLARA database contain reflections from the rain and melting layer that were so strong that the returned signal saturated the receiver. This is visible in the radar images as broad vertical lines above the cloud top, which occur during the most intense periods.

Sometimes in the top of the radar image (10 %) residual noise is present, which is visible as a speckled pattern with typically a very low SNR. The top part of the figures in this dissertation is usually removed. However, this noisy part has to be taken into account when data from the CLARA database are used, where residual noise is often present.

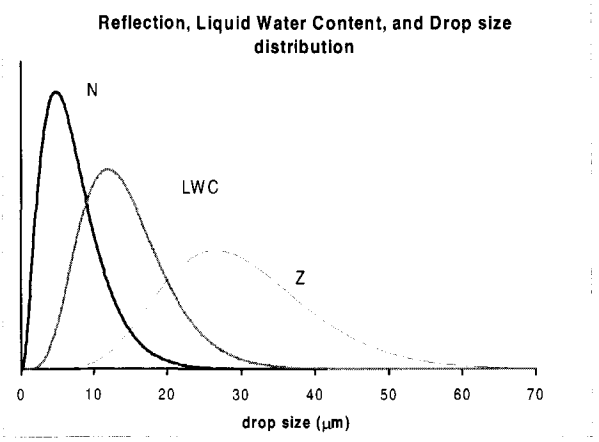

Figure 3.9. Illustration of the importance of the drop size to the relation between LWC and radar reflectivity factor (Z) when a typical theoretical distribution is used for the number density.

Close to the surface level there is sometimes some residual ground clutter. This may be the cause of the reflections in the lowest 100 m of Figures 3.3 and 3.4.

3.4 Retrieval of cloud properties

This section will give a short overview of the scientific work on the retrieval of cloud properties. Our main aim is to explain how the other chapters fit into this scientific effort; the treatment will thus be far from comprehensive. This section mainly discusses retrievals by means of radar data and possible with the CLARA set-up.

3.4.1 Radar

The simplest method to retrieve the LWC is to relate the radar reflectivity directly to the liquid water content (LWC) of the clouds, i.e. by using a Z-LWC relation. This is similar to the methods used to estimate the rain rate based on the radar reflectivity. Traditionally, one uses a power law for this Z-LWC relation.

The direct problem is easily solved; for a known drop size distribution one can calculate the LWC and the radar reflectivity factor (assuming incoherent particle scatter). The inverse problem, estimating the LWC from the measured radar reflectivity, is far from trivial, however. The radar reflectivity depends mainly on the large

droplets, whereas the LWC content is typically concentrated in the smaller part of the drop size distribution, see Fig. 3.9.

When the drop size distribution (DSD) is narrow and hence there is a strong relation between the smaller drops and the larger drops, knowledge of the average drop diameter is a prerequisite for solving the inverse problem. An example of clouds with a narrow DSD are young cumulus clouds. On the basis of in situ measured (FSSP) drop size spectra, Paluch et al. (1995) conclude that the LWC can be estimated with an error of just 13 % if the height above the cloud base is known. This height is closely related to the average drop size. They use only incoherent particle scatter.

The inverse problem becomes more difficult to solve when the drop size distribution is wider or bimodal. In stratocumulus clouds, especially drizzling clouds, the relation between LWC and incoherent particle scatter can be very weak [Fox and Illingworth, 1997; De Wit et al., 1999]. In the precipitating clouds shown in Fig. 3.4 and discussed in chapter 7, the cloud layer is not apparent in the radar reflectivity measurements; the information content of the radar reflectivity about the LWC is in this case negligible.

3.4.2 Radar, Radiometer

A ground-based microwave radiometer is able to give an accurate estimate of the liquid water *path* (LWP): the total amount of water in an atmospheric column [Löhnert et al., 1999]. The power received by the radiometer is determined by the LWP, but also by the distribution of the liquid water as a function of height. This latter is due to the temperature dependence of the absorption and of the emission of microwaves by the waterdroplets. Therefore, the estimate of the LWP can be improved by combining the radiometer data with information from other (remote sensing) instruments, for example with the radar reflectivity profile, lidar backscatter profile, infrared radiometer temperature, and ground temperature and humidity [Erkelens et al., 1998; Crewell et al., 1999].

Using an assumption on the distribution of the water in the cloud, one can take the liquid water path as a basis for estimating the LWC, the droplets' diameter and the number density. Frisch et al. (1998) used the radar reflectivity to estimate this height distribution. The square root of the radar reflectivity is proportional to the LWC if a fixed width of the drop size distribution is assumed. This LWC integrated over the height of the atmosphere should give the LWP, which makes it possible to estimate the constant of proportionality. This constant includes the square root of the number density, so it is possible to estimate the number density as well – together with the average diameter – assuming the number density is height independent.

Löhnert et al. (1999) use a similar approach, but they use a cloud model to estimate the parameters in the power law relationship between Z and LWC

($Z = a\ LWC^b$). In the Frisch method b is fixed at 0.5. All the retrieval parameters are optimised according to their uncertainty. Based on a modeling study Löhnert et al. (1999) find that their retrieval method has a smaller root-mean-square error than the method of Frisch et al. (1998).

3.4.3 Radar, Radiometer, Lidar

The retrieval method for stratocumulus clouds of Boers et al. (2000) uses radar (for the cloud top), lidar (for the cloud base), and microwave radiometer (for the LWP). Between cloud base and top a linear LWC profile is assumed, the slope of which is fitted to match the LWP from the radiometer. With the aid of radiosondes or an infrared radiometer the deviation of this cloud from the adiabatic profile can be estimated, if it is assumed that the deviation is constant for the entire height of the cloud. With this information and the lidar extinction profile near the cloud base it is possible to estimate the number density and average droplet diameter. This method was applied to data from the CLARA measurement campaigns and the results were found to be in the same order of magnitude as simultaneous FSSP measurements.

Boers et al. use the lidar to estimate the cloud base height, because lidar is more reliable than radar in estimating this variable (see chapter 7). From the radar measurements only the cloud top is used, which makes the method robust against inaccuracies in the measurements of the radar reflectivity factor of clouds.

Another approach to combining the radar, lidar and microwave radiometer to retrieve liquid water content profiles is using an artificial neural network, see e.g. Crewell et al. (1999). The neural network is trained using radiative transfer calculations, which are based on measured profiles of humidity and temperature from radiosondes. Clouds were modeled in these profiles by assuming that clouds (with a modified adiabatic LWC-profile) are present when the humidity is above 95 percent. An advantage of this approach is that it makes it very easy to combine data from very different instruments to get an estimate of the LWC profile. Crewell et al. (1999), for example, combined a varying number of channels from the microwave radiometer with the cloud base (lidar), cloud top (radar), cloud-base temperature (infrared radiometer), ground temperature, ground humidity, ground pressure.

3.4.4 Evaluation

There is no such thing as the best retrieval method. The different methods all have their own applications, strengths and weaknesses. The methods can be compared theoretically, by modeling and by comparing their results in case studies. Validation of the retrieval methods (or falsification) with in situ measurements is often difficult, as the difference in measurement characteristics (measurement volume, position and

time) between the ground-based remote sensing instruments and the in situ instruments introduces large uncertainties.

In a modelling study with artificial clouds done by Löhnert et al. (1999) the Z-LWC power law retrieval gave RMS errors in the order of 70 to 80 percent of the LWC, although cases with drizzle were excluded. According to this modelling study the Frisch method gave better results: 50 to 65 percent RMS error. The Optimal Estimation method was 10 to 15 percent better than Frisch, with RMS errors between 30 and 50 percent.

Erkelens et al. (1999) compared the retrieval methods of Frisch et al. (1998) and Boers et al. (2000) for estimating the number density of the cloud droplets. Conclusions from this study are that the Frisch method is more sensitive to errors in the assumed width of the drop size distribution, and that for the Boers method an accurate estimate of cloud height is necessary. Furthermore, the Frisch method will not work during drizzle (due to the large-drop problem), whereas the Boers method was affected less by this factor.

What do these retrievals tell us about radar remote sensing of clouds? In these retrievals there are two crucial parameters that radar can deliver: cloud boundaries and a radar reflectivity profile. That is partly why chapter 7 is devoted to the accurate measurement of cloud boundaries in as many atmospheric conditions as possible. Of course the cloud boundaries are not only important to retrieve these micro-physical cloud properties, but are themselves also of direct interest to climate change studies.

The measured radar reflectivity profiles can be unrepresentative for the cloud drops that contain most of the cloud liquid water due to the large-drop problem [Fox and Illingworth, 1998]. Promising measurement techniques for solving this problem are the ones using attenuation of the radar signal instead of the radar reflectivity itself [Guyot and Testud, 1999; Hogan et al. 1999].

The Doppler processing of the radar, which is discussed in chapter 4, can also influence the measured radar reflectivity profiles. This chapter also gives a method to correct for the influence of the radar processing, so the measured reflectivities become useable for retrievals requiring quantitative values.

An assumption in the retrievals that use the radar reflectivity quantitatively is that the scattering of the microwaves is determined by incoherent particle scattering. This can lead to large retrieval errors when coherent air scatter or coherent particle scatter dominates. That is why chapter 5 introduces coherent particle scattering by spatial structures in the liquid water content of the clouds. Chapter 6 builds on this by examining the importance of coherent particle scattering and coherent air scattering compared to incoherent particle scattering.

Reference

Boers, R, H.W.J. Russchenberg, J.S. Erkelens, V.K.C. Venema, A.C.A.P. Van Lammeren, A. Apituley, and S. Jongen. Ground-based remote sensing of stratocumulus properties during CLARA-1996. *J. Appl. Meteorol.*, **39**, no. 2, pp. 169–181, 2000.

Cohn, S.A., R.R. Rogers, S. Jascourt, W.L. Ecklund, D.A. Carter, and J.S. Wilson. Interactions between clear-air reflective layers and rain observed with a boundary layer wind profiler. *Radio Sci.*, **30**, pp. 323-341, 1995.

Crewell, S., U. Löhnert, and C. Simmer. Remote sensing of liquid water profiles using microwave radiometry. *Proc. Remote sensing of cloud parameters: retrieval and validation*, IRCTR, Delft, The Netherlands, pp. 45-50, ISBN: 90-804551-6-4, 21-22 Oct., 1999.

Crutzen, P.J., and T.E. Graedel. *Weer en klimaat; atmosfeer in verandering.* In Dutch, Beck, Natuur en Techniek, 192 p., ISBN: 90-73035-42-2, 1996.

Doviak, R.J., and D.S. Zrnic. *Doppler radar and weather observations; second edition.* Academic Press, San Diego, 562 p., ISBN: 0-12-221422-6, 1993.

Erkelens, J.S., S.C.H.M. Jongen, H.W.J. Russchenberg, and M.H.A.J. Herben. Estimation of Cloud Droplet Concentration from Radar, Lidar and Microwave Radiometer Measurements. *Proc. Remote sensing of cloud parameters: retrieval and validation*, IRCTR, Delft, The Netherlands, pp. 107-111, ISBN: 90-804551-6-4, 21-22 Oct., 1999.

Erkelens, J.S., H.W.J. Russchenberg, S.C.H.M. Jongen, and M.H.A.J. Herben. Combining radar and microwave radiometer for cloud liquid water retrieval. *Proc. 28th European Microwave Conf.*, Amsterdam, The Netherlands, **2**, pp. 67-72, 1998.

Fox, N.I., and A.J. Illingworth. The potential of a spaceborne cloud radar for the detection of stratocumulus clouds. *J. Appl. Meteorol.*, **36**, no. 6, pp. 676-687, 1997.

Frisch, A.S., G. Feingold, C.W. Fairall, T. Uttal, and J.B. Snider. On cloud radar and microwave radiometer measurements of stratus cloud liquid water profiles. *J. Geophys. Res.*, **103**, no. D18, pp. 23195-23197, 1998.

Gerber, H. Microphysics of marine stratocumulus clouds with two drizzle modes. *J. Atmos. Sci.*, **53**, no. 12, pp. 1649-1662, 1996.

Gibbs, A.P.R. A comparative study of reflectivity and liquid water content of stratocumulus and cumulus clouds using radar and FSSP measurements. IRCTR-graduation thesis no. 68-220-A254-97, 105 p., 1997.

Graedel, T.E., and P.J. Crutzen. *Atmosphere, climate, and change.* Freeman, Oxford, UK, 196 p., ISBN: 0-7167-5049-X, 1995.

Guyot, A., and J. Testud. The Dual-Beam Technique Applied to Airborne Cloud Radar. *J. Atmos. and Ocean. Tech.*, **16**, pp. 924-938, July, 1999.

Hogan, R.J., A.J. Illingworth, and H. Sauvageot. Cloud characteristics from dual wavelength millimetre-wave radar. *Proc. 29th Conf. Radar Meteorol.*, Montreal, Canada, pp. 457-459, 1999.

Houghton, J.T., L.G. Meira Filho, and B.A. Callander (eds.). *Climate change 1995; the science of climate change.* Cambridge University Press, Cambridge, UK, 572 p., ISBN: 0-521-56433-6, 1996.

Kattenberg, A. et al., in *Climate Change 1995,* J.T. Houghton et al., Eds. (Cambridge University Press, Cambridge), chap. 6, 1996.

Kaya, C. Filtering disturbance lines from radar images. In Dutch: Filteren van Stoorlijnen uit radar beelden. IRCTR, Delft University of Technology, Delft, The Netherlands, report no. IRCTR-S-003-99, 85 p., 1999.

Klaassen, W. *From snowflake to raindrop; Doppler radar observations and simulations of precipitation.* PhD dissertation, 134 p., 1989.

Knight, C.A., and L.J. Miller. Early radar echoes from small, warm cumulus: Bragg and hydrometeor scattering. *J. Atmos. Sci.*, **55**, pp. 2974-2992, 1998.

Löhnert, U., S. Crewell, and C. Simmer. Combining a Cloud Radar, a Passive Microwave Radiometer and a Cloud Model to Obtain Cloud Liquid Water. *Proc. Remote sensing of cloud parameters: retrieval and validation*, IRCTR, Delft, The Netherlands, pp. 101-106, ISBN: 90-804551-6-4, 21-22 Oct., 1999.

Martin, G.M., D.W Johnson, and A. Spice. The measurement and parameterization of effective radius droplets in warm stratocumulus clouds. *J. Atmos. Sci.*, **51**, no. 13, pp. 1823-1842, 1994.

Niemeijer, R.J. *Doppler-polarimetric radar signal processing.* PhD dissertation, Delft University Press, Delft, The Netherlands, 221 p., 1996.

Ottersten, H. *Radar angels and their relationship to meteorological factors.* FOA reports, **4**, no. 2, 33 p., Forvarets Forskningsanstalt, Stockholm, Sweden, 1970.

Paluch, I.R., C.A. Knight, and L.J. Miller. Cloud liquid water and radar reflectivity of non-precipitating cumulus clouds. *J. Atmos. Sci.*, **53**, pp. 1587-1603, 1996.

Pruppacher, H.R, and J.D. Klett. *Microphysics of Clouds and Precipitation; second edition.* Kluwer, Dordrecht, 954 p., ISBN: 0-7923-4211-9, 1997.

Rogers, R.R, and W.O.J. Brown. Interactions Between Scattering by Precipitation and the Clear Air. *Proc. 8th URSI Comm. F triennial Open Sym.*, pp. 235-238, 22-25 September, 1998.

Rogers, RR, and M.K. Yau. *A short course in cloud physics - 3rd edition.* Butterworth-Heinemann, Oxford, UK, 290 p., ISBN: 0-7506-3215-1, 1996.

Russchenberg, H.W.J. *Ground-based remote sensing of precipitation using a multi-polarized FM-CW Doppler radar.* PhD dissertation, Delft University Press, Delft, The Netherlands, 206 p., ISBN: 90-6275-823-1, 1992.

Sassen, K., G.G. Mace, Z. Wang, M.R. Poellot. Continental Stratus Clouds: A Case Study Using Co-ordinated Remote Sensing and Aircraft Measurements. *J. Atmos. Sci.*, **56**, pp. 2345-2358, 15 July, 1999.

Seinfeld, J.H., and S.N. Pandis. *Atmospheric chemistry and physics; From Air Pollution to Climate Change.* John Wiley & Sons, New York, USA, 1326 p., ISBN: 0-471-17815-2, 1998.

Slingo, A., S. Nicholls, J. Schmeitz. Aircraft observations of marine stratocumulus during JASIN, *Quart. J. R. Met. Soc.*, **108**, pp. 833-856, 1982.

Vohl, O., S.K. Mitra, S.C. Wurzler, and H.R. Pruppacher. A Wind Tunnel Study of the Effects of Turbulence on the Growth of Cloud Droplets by Collision and Coalescence. *J. Atmos. Sci.*, **56**, pp. 4088-4099, 15 Dec., 1999.

Watson, R.T., M.C. Zinyowera, and R.H. Moss (eds.). *Climate Change 1995; Impacts, Adaptations and Mitigation of Climate Change: Scientific-Technical Analyses.* Cambridge University Press, Cambridge, UK, 878 p., ISBN: 0-521-56431-X, 1996.

Wit, de J.J.M., R.J.P. Baedi, J.S. Erkelens, H.W.J. Russchenberg, and J.P.V. Poiares Baptista. Development of retrieval algorithms of cloud parameters from radar and lidar based on the CLARE data set. *Proc. Remote sensing of cloud parameters: retrieval and validation*, Delft, The Netherlands, 21-22 Oct, pp. 83-88, 1999.

Chapter 4

Clipping radar velocity spectra to enhance the sensitivity to cloud measurements

Abstract. *Spectral processing can enhance the sensitivity of cloud radars considerably. This chapter discusses a method for estimating the moments of velocity spectra from clouds. In this method the velocity cells with a power level close to the noise level are removed. This method is called clipping or thresholding. With this method cloud signals well below the total noise level can be detected. A disadvantage of clipping is that it also reduces the power received from the cloud itself. Using a priori knowledge on the cloud signal one can correct for this effect. Clipping seems a promising processing technique to enhance the sensitivity of cloud radars. Still many improvements and further processing steps can be investigated to refine the technique.*

4.1 Introduction

To study clouds, one needs a radar having a high sensitivity. Especially the radar measurements of stratocumulus clouds that provide the background for this thesis explore the technological limits. For example, on the basis of a simple cloud model Sassen *et al.* (1999) estimate that a radar with a sensitivity of –40 dBZ is needed to give about the same cloud base height as a lidar for water clouds. For some ice clouds the sensitivity needs to be even better than –40 dBZ [Sassen and Khvorostynov, 1998]. Weitkamp et al. (1998) report a total multi-layered cirrus cloud which their cloud radar could not detect as the reflectivity was below –30 dBZ. So it is paramount that radar data processing increases the sensitivity as much as possible, both for cloud detection and for quantitative measurements.

Accurate cloud detection is required by, e.g., the Boers-method for retrieving the Liquid Water Content (LWC) of water clouds [Boers et al., 2000]. And quantitative measurements are needed for LWC retrievals by the Frisch-method [Frisch et al., 1995]. Many other applications require either sensitive cloud detection or accurate quantitative radar reflectivity measurements. To get optimal performance these two tasks are best done by separate processing methods. For example, Cloutiaux et al. (1999) extensively studied the detection capabilities of the radars used at the site of the ARM (Atmospheric Radiation Measurement) program. The ARM mm-wave cloud radars use specific processing methods to detect different cloud types; some of the most sensitive methods do not give reliable quantitative results.

In this chapter clipping of the velocity spectra will be presented as a robust data processing method that can enhance the sensitivity of coherent cloud radars for quantitative measurements. As clipping can influence the quantitative results, a correction method for this effect will be given. Computing a velocity spectrum can increase the signal-to-noise ratio (SNR) considerably. The noise is distributed over all velocity cells and the signal from atmospheric targets is concentrated to a limited interval. Usually the entire velocity spectrum is not stored as this takes a lot of disk space; instead the moments of the velocity spectrum are computed: total power, average velocity and spectral width.

One way to prevent that the scattered power of the atmospheric target is again drowned in noise when the moments are calculated is to apply clipping or thresh-

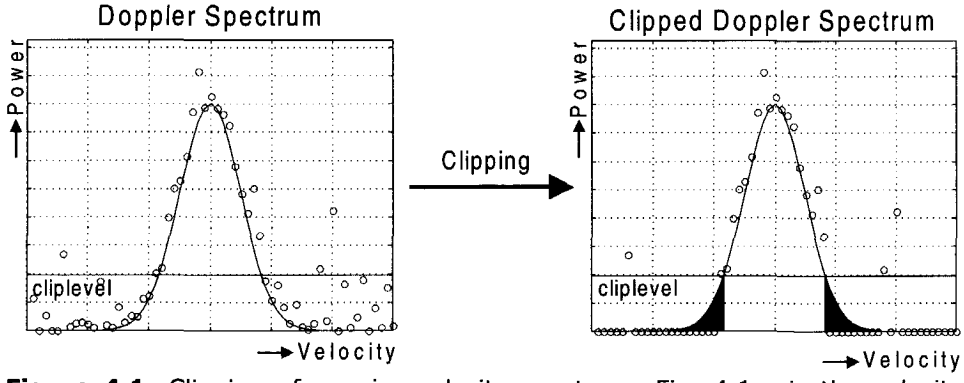

Figure 4.1. Clipping of a noisy velocity spectrum. Fig. 4.1a. is the velocity spectrum before clipping; Fig. 4.1b after clipping. The circles are the measured points: the original signal plus noise. The original signal is drawn to guide the eye. The horizontal line is the clipping level (four times the noise level per velocity cell). After clipping most of the noise power is removed, although some cells outside the region of the signal are not clipped away. A part of the original signal is also removed: the hatched area. To correct for this removal of power, a clipping correction is derived in this study.

olding. Clipping simply means ignoring velocity cells that have a power close to the noise level (per velocity cell). Figure 4.1 explains this idea visually. The spectral data processing is described in more detail in section 4.2.

Although clipping is very effective in removing noise, it has a drawback: part of the signal is removed; the hatched area in Fig. 4.1. Especially, if the clip level in a velocity cell is close to the peak power, most of the signal power will be removed. The width of the velocity spectra is also strongly affected. If the distribution is not symmetrical, the average velocity will also change due to clipping. Clipping of the velocity spectra is not a new idea; it was one of the methods Sirmans and Bumgarner (1975) considered for estimation of the mean Frequency (velocity), while Gordon (1995) used it to estimate the mean velocity and width of the velocity spectrum. Our approach is new in the sense that we apply clipping to enhance the estimation of the total power; we combine clipping with a further processing step to correct for the reduction in backscattered power.

Section 4.2 will give an introduction to spectral processing of cloud data using clipping. The derivation of a clipping correction function for the measured radar reflectivity and the results are presented in section 4.3. As the correction for clipping depends on the target and the data processing, a generally applicable correction function cannot be given. Instead, this work gives a recipe to derive a clipping correction for a specific situation. After our conclusions (section 4.4), in section 4.5 suggestions are made for future research to improve the clipping algorithm.

4.2 Radar data processing

The outline of the radar data processing with clipping is as follows: For each radar range cell a velocity spectrum (distribution) is computed with an FFT over N complex voltages. To reduce the variance of the signal and the noise, four of these velocity power spectra – consisting of N velocity cells – are averaged. This averaged spectrum is smoothed to further reduce the variance before clipping. The chosen clip level for one velocity cell is a few times the noise level per velocity cell. The velocity cells with a power below the clip level are ignored in the calculation of the three moments: radar reflectivity, velocity, and spectral width. Before calculating the moments, we shift the peak power to the middle to reduce problems with velocity aliasing and remove clutter from ground reflections.

The effect of clipping on radar cloud measurements made with the Delft Atmospheric Research Radar, DARR, is studied. DARR is a 9-cm radar with a high velocity resolution of 3.5 cm/s. Normally 256 velocity cells make up one velocity spectrum. This spectrum is clipped at 7 dB above the noise per velocity cell. The velocity width (standard deviation) for the clouds in this study is between 11 and 28 cm/s, i.e. be-

tween 3 and 8 velocity cells. This means that 95 percent of the power is distributed over 12 (5 %) to 32 (13 %) velocity cells (4 times the standard deviation). The improvement in detection capability comes from this small spectral width of the clouds compared to the width of the spectrum. If the width of the measured object is wider – when the power is distributed over most of the spectrum – the spectral processing with clipping will decrease the sensitivity of the radar.

To be able to correct the measured reflectivity for clipping, one must know the statistical properties of the cloud signal. The velocity spectrum of clouds have a non-zero natural spectral width. The main interest of this study is non-precipitating stratocumulus water clouds, which have a low SNR. Turbulent motion of the atmosphere mainly determines the velocity spectrum for these clouds; the fall velocity of cloud droplets is negligible. The turbulence in a large radar cell is the result of many independent processes, so by the central limit theorem a Gaussian distribution is a good approximation for the shape of the cloud spectrum.

The shape and width of the smoother for the velocity spectrum should be optimised for the spectral width of the cloud: A wide smoother is desirable as it reduces the variance strongly and thus enables us to decrease the clip level. However, this will also broaden the cloud peak in the velocity spectrum and thus reduce the SNR in the velocity cells with the highest values, which can make the radar less sensitive. For cloud measurements with DARR, a Gaussian smoother with a width of 14 cm/s is used. Note that the smoothing will increase the measured width, especially for spectra with a small width. For a target of which the shape of the velocity spectrum is known, this can easily be corrected for, using:

$$\sigma^2_{measured} = \sigma^2_{original} + \sigma^2_{smoother} \tag{4.1}$$

The clip level is normally chosen to be a few times the noise level per velocity cell. If the level is too low, a lot of noise and other system disturbances will still pollute the measurement, whereas if the clip level is too high, too much of the signal will be removed. The optimal solution will depend on the properties of the target, especially its spectral width. Simulations show that a clip level that is 3 times the noise level (or 5 dB) should be sufficient to suppress the noise. Gordon (1995) also used this as minimum clip level. However, we found experimentally that a clip level of 7 dB (5 times the noise level) was needed to get clean measurements. This discrepancy is probably due to all sorts of system effects that are also clipped away. We consider the latter empirical method the best method to determine the clip level.

Clipping removes the noise in the velocity cells where the power is below the clip level. In order to remove the noise from velocity cells where the power is above the noise level, the average noise level should be subtracted before clipping. This was not

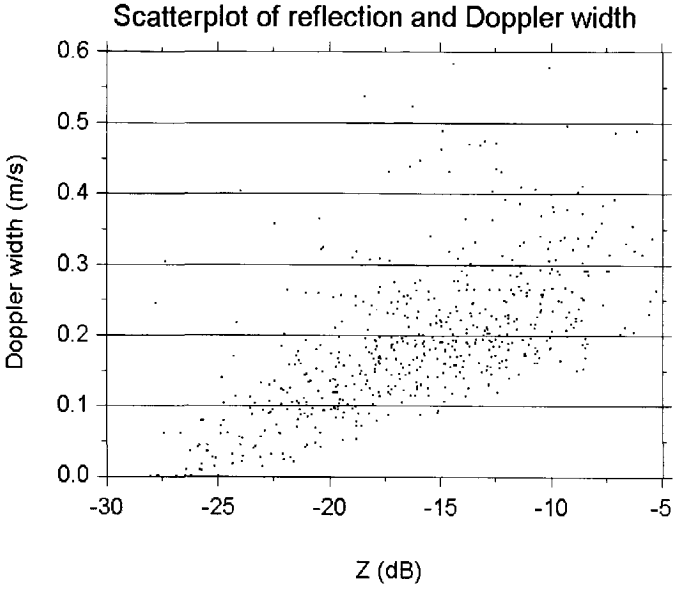

Figure 4.2. Scatter plot of reflection and spectral width for stratocumulus cloud. Clipping reduces the measured width for weak signal by removing power from the tails of the distribution.

done in the processing for the results shown in this study. The clipping correction functions shown this chapter therefore also correct for this effect.

The effect of clipping on the measured radar reflectivity and spectral width is seen in Fig. 4.2, a scatter plot of these two variables. This plot was made selecting data points from a thin stratocumulus cloud. The natural width of the velocity spectrum of this cloud, which originates mainly from turbulence, can be estimated using the minimum measured width at high SNR (around –5 dB), which is in this case about 18 cm/s. This width (after processing) corresponds to a spectral width of the cloud signal (before smoothing) of 11 cm/s for a Gaussian spectrum. Based on similar case studies of two stratocumuli and two ice clouds we estimate that this measured width (i.e. the standard deviation) varies between 11 and 28 cm/s.

Note that in Fig. 4.2 the minimum measured spectral width decreases with the radar reflectivity; at the lowest measurable reflectivities (–25 dB) it has been reduced completely to zero width. In simulations of the data processing with just a cloud signal and noise the scatter plot looks similar as Fig. 4.2. However, it contains only the data points from Fig. 4.2 with the lowest width for a specific SNR. The points with a larger width in Fig. 4.2 do not occur in the simulation, so they are probably caused by system disturbances or other non-cloud signals.

4.3 Clipping correction function

As the correction for clipping depends on the properties of the target and the data processing applied, a generally applicable correction function to restore the measured power cannot be given. Instead, in section 4.3.1 a recipe will be given to derive a clipping correction for a specific situation. And in section 4.3.2 this recipe will be followed to derive a clipping correction function for our radar set-up. This function will be applied to a radar measurement of a stratocumulus cloud to show the results.

4.3.1 Recipe for correction

In this section a recipe is given to derive a clipping correction function to correct the measured SNR to the real SNR. This clipping correction function will be different for every radar set-up and type of target.

Step 1: Determine the shape of the spectrum. The clipping is corrected by calculating what the radar processing does to a known signal. Therefore, a good knowledge of the real velocity spectrum is paramount. This shape can be obtained from theoretical considerations or from dedicated measurements with a high SNR.

Step 2: Build a data processing simulator. Next a simulator of the radar data processing has to be built. Input of this simulator is a noisy velocity spectrum and output is the three moments. This simulator can be used as a tool to find a good data processing for a specific task.

Step 3: Simulate signals with various SNRs. The algorithm for calculating the clipping correction is very simple, though computationally intensive. Signals having SNRs between –20 and 10 dB should be used as input, to cover the entire range where correction may be needed. To this signal noise has to be added and it should be put through the normal processing steps, including the calculation of the moments.

Step 4: Derive clipping corrections from simulations. The scatter plot of input and output SNR can then be fitted to a polynomial function. Take care not to use this function outside the fitting limits. The measured values with high SNR should not be corrected. It is probably best to refrain from correcting values close to the detection limit to avoid amplifying residual noise and other impurities.

4.3.2 Results

The above recipe has been followed to compute a few clipping correction functions. In the data processing simulator the following variables are used: a Gaussian smoother with a width of 14 cm/s and a clip level of 7 dB times the noise level per velocity cell.

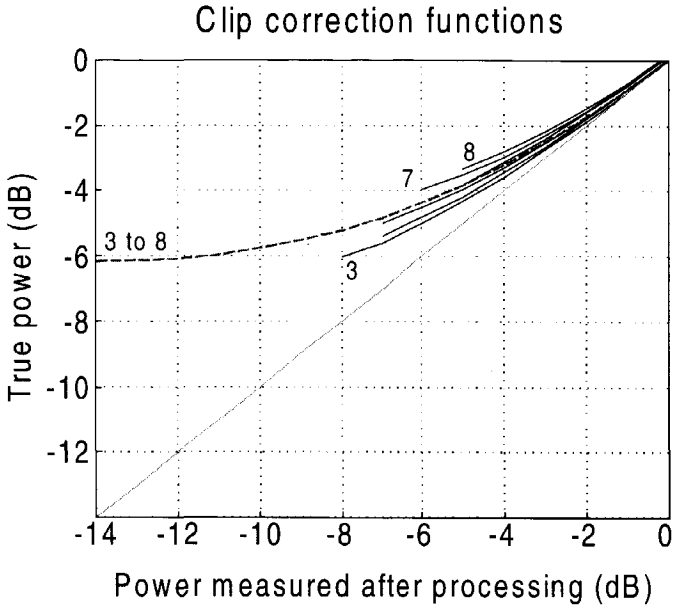

Figure 4.3. The clipping correction function for the DARR processing. The thin black lines are made using a Gaussian signal with one width of 3, 4, 5, 6, 7 and 8 Doppler cells. The lowest line is the one for the smallest width, etc. The grey striped line was made using Gaussian signal with a uniform distribution of widths between 3 and 8 velocity cells.

The cloud was assumed to have a Gaussian spectrum. The clipping correction functions for spectral widths 3 through 8 cells (11 to 28 cm/s) are plotted in Fig. 4.3 as black lines. It can be seen that the width of the spectrum influences the strength of the smallest detectable signal and that the spread is about 2 dB. Because the nature of the real signal is unknown, the error in the clipping correction may be much larger. Determining the spectral width for every (part of a) cloud can be unpractical for large data-sets. So we calculated a 'general' clipping correction function using as input signal a uniform distribution of widths between 3 and 8 cells. The computed function is shown in Fig. 4.3 as a grey striped line.

In Fig. 4.3 one can see that cloud signals with a SNR of –6 dB or higher can be measured. The lowest measured SNR using the usual settings for DARR is –17 dB. If the signal power would be confined to one velocity cell the 'Doppler' gain is 24 dB for a spectrum with 256 velocity cells; from this the clip level of 7 dB should be subtracted to get the lowest measured SNR. With these settings DARR is 11 dB (–17 – –6) less sensitive to clouds than to a target with a constant radial velocity. Given the

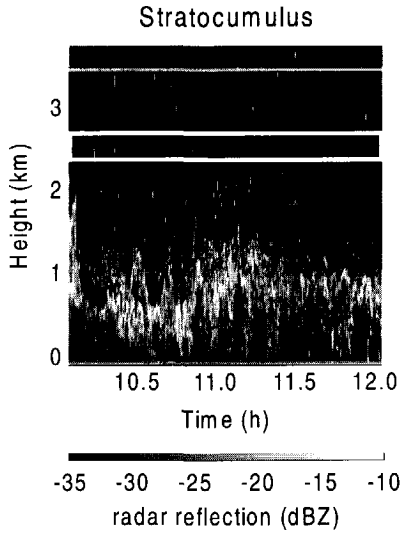

Figure 4.4. Measurement by DARR of a stratocumulus cloud at 2.6 km, with clear-air scatter in the boundary layer below 1.5 km (Fig. 4.4a). The histograms in Fig. 4.4b and 4.4c are made from the data in the box around the cloud. Fig. 4.4b shows a histogram of measurement points for each reflection value. In the corrected values there is a sharp cut-off at -27 dBZ (-6 dB SNR). Figure 4.4c shows how much the points have been corrected.

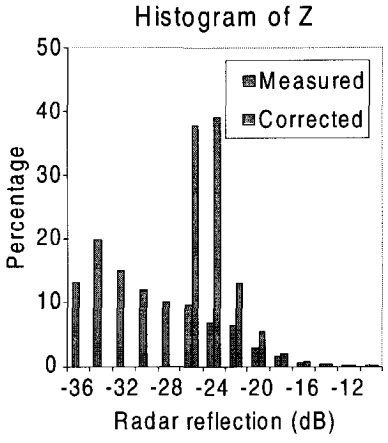

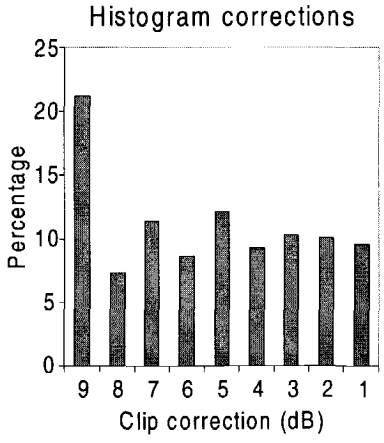

shape of the correction function, a small error in measured power is not very important for a low SNR, if a clip level is used that is higher than 5 dB. If, for example, the noise would increase the measured SNR from –16 to –10 dB, the corrected SNR would still be about –6 dB.

Without this correction function, cloud measurements with DARR below a SNR of about 0 dB are erroneous. Using the clip correction function, signals down to -6 dB can be reliably measured; the correction thus improves the performance of the radar by about 6 dB.

As an example, the measured radar reflections from a stratocumulus cloud are shown in Fig. 4.4a, a histogram of the measured and the corrected values is shown in Fig. 4.4b (using the general correction function). The reflections from this stra-

tocumulus cloud are just above the detection level, as they often are. So the reflection values have to be corrected considerably (Fig. 4.4c). The clipping corrections are around 4 dB in the middle of the cloud, up to 10 dB at the edges. There is a clear cutoff in the corrected radar reflection (Fig. 4.4b) and at the minimum SNR of -6 dB. This indicates that in this case the radar does not see the entire cloud. This was also found in the lidar radar synergy study of a stratocumulus cloud [Venema et al., 2000]. The study showed that a large part of the bottom of the stratocumulus cloud is not detected by DARR, but can be seen with lidar. Values close to the detection limit have been ignored, i.e. no correction of more than 10 dB are made. The histogram with the percentage of cloud pixels corrected a certain amount (Fig. 4.4c) shows a larger first bin (from 10 to 9 dB correction) than the others. Thus maybe some noise still was erroneously enhanced.

The clipping correction seems to work fine and the corrected data looks reliable. But one should remember that corrected values can be up to 10 dB higher than the measured values, which means that just 10 percent of the power was measured. The correction function has to be very accurate to obtain reasonable values.

4.4 Conclusions

Data spectral processing can enhance the sensitivity of a cloud radar considerably. Due to the distributed nature of clouds this enhancement bears, unfortunately, much less effect on clouds than on targets with just one radial velocity. Clipping of the velocity spectra is effective in reducing the noise, but it can also reduce the measured power of cloud signals with a low SNR and a relatively high spectral width. It is possible to correct for this undesired effect if the shape of the original signal is known. The result for a stratocumulus cloud shows a sharp cutoff, which indicates that only part of this cloud is measured.

More work is needed to make a good error estimate. What errors are made, for example, if the width of the velocity spectrum, which is used for the correction, is wrong, or if the spectrum has a different shape?

4.5 Improved clipping

The clipping correction function needs information on the shape of the spectrum as input; A velocity spectrum the SNR of which is much better (more than 10 dB) than the spectra from which the moments were calculated would therefore allow a very reliable clipping correction. Such a velocity spectrum could be stored a lower rate than the moments. The magnitude of the variations in the moments, which are stored at a high rate, could indicate if the averaged velocity spectrum is a reliable

information source. The full velocity spectrum gives information as well as on clutter, disturbances in the system, and bimodal or multimodal spectra. For this reason alone it would already be useful to store the complete velocity spectrum as well.

There may be other ways to improve the clipping process which should be studied. The decision to clip is now only based on the signal-to-noise ratio. Other criteria for clipping could complement SNR, e.g. the standard deviation of a time series of the power in a velocity cell, the cross correlation with another polarisation state or whether a cell was clipped in previous spectra.

Using information on the number of clipped cells could be useful to improve the reliability of the clipping correction. The correction could then become a function of SNR and the number of clipped cells. A simulation study would be interesting to estimate how much this could improve the clipping correction.

The clipping method could be used as a first step in a more sophisticated processing method, given enough calculation power. The calculated velocity (and possibly the spectral width) could, for example, be used to define a clipping region: Only values from the original velocity spectrum within this clipping region should then be used in the calculation of the moments.

Reference

Boers, R., H.W.J. Russchenberg, J.S. Erkelens, V.K.C. Venema, A.C.A.P. van Lammeren, A. Apituley, and S. Jongen. Ground-based remote sensing of stratocumulus properties during CLARA-1996. *J. Appl. Meteorol.*, **39**, no. 2, pp. 169–181, 2000.

Clothiaux, E.E., K.P. Moran, B.E. Martner, T.P. Ackerman, G.G. Mace, T. Uttal, J.H. Mather, K.B. Widener, M.A. Miller, and D.J. Rodriguez. The Atmospheric Radiation Measurement Program Cloud Radars: Operational Modes. *J. Atmos Ocean. Technol.*, **16**, July, pp. 819-827, 1999.

Frisch, F.G., C.W. Fairal, and J.B. Snider. Measurement of stratus cloud and drizzle parameters in ASTEX with a Ka-band Doppler radar and a Microwave radiometer. *J. Atmos. Sci.*, **52**, pp. 2788-2799, 1995.

Gordon, W.B. Estimation of Doppler parameters using a thressholding technique. *27th Conf. on radar meteorol.*, pp. 753-755, 1995.

Sassen, K., and V.I. Khvorostyanov. Radar probing of cirrus and contrails: Insights from 2D model simulations. *Geophys. Res. Let.*, **25**, April, no. 7, pp. 975-978, , 1998.

Sassen, K., G.G. Mace, Z. Wang, and M.R. Poellot. Continental Stratus Clouds: A Case Study Using Coordinated Remote Sensing and Aircraft Measurements. *J. Atmos. Sci.*, **56**, 15 July, pp. 2345-2358, 1999.

Sirmans, D., and B. Bumgarner. Numerical Comparison of Five Mean Frequency Estimators. *J. Appl. Meteorol.*, **14**, Sept., pp. 991-1003, 1975.

Venema, V.K.C., H.W.J. Russchenberg, A. Apituley, A. van Lammeren, and L.P. Ligthart. Cloud boundary height measurements using lidar and radar. *Physics and Chemistry of the Earth.*, **24**, no. 2, pp. 129-134, 2000.

Weitkamp, C., H. Flint, W. Lahmann, F.A. Theopold, O. Danne, M. Quante, and E. Raschke. Radar and Lidar Cloud Measurements at Geesthacht. *Phys. Chem. Earth (B)*, **24**, no. 3, pp. 163-166, 1999.

Chapter 5

Coherent scattering of microwaves by particles: Evidence from clouds and smoke

Abstract. *Many radar measurements of the atmosphere can be explained in terms of two scattering mechanisms: incoherent scattering from particles, and coherent scattering from variations in the refractive index of the air, commonly called clear-air or Bragg scattering. Spatial variations in the liquid water content of clouds may also give a coherent contribution to the radar return, but it is commonly believed that this coherent scattering from the droplets is insignificant, because variations in humidity have a much larger influence on the refractive index than equal variations in liquid water content. We argue that the fluctuations in water vapour mixing ratio in clouds can be much smaller than those in liquid water mixing ratio.*

In this chapter an expression for the strength of the coherent scattering from particles will be derived for fluctuations caused by turbulent mixing with clean (i.e., particle-free) air, where it will be assumed that the particles follow the flow, i.e., their inertia is neglected. It will be shown that the coherent contribution adds to the incoherent contribution, the latter always being present. The coherent particle scattering can be stronger than the incoherent scattering, especially at longer wavelengths and high particle concentrations.

Recently published dual-frequency measurements of developing cumulus clouds and smoke show a correlation for which no explanation has been found in terms of incoherent particle scattering and coherent air scattering. Scatterplots of the reflectivity factors at both frequencies show a clustering of points in between the values that correspond to pure clear-air and pure incoherent scattering. Those differences in the radar reflectivity factors could be due to a mixture of Bragg scattering and incoher-

ent particle scattering, but then no correlation is expected, because the origin of the scattering mechanism that dominates at each wavelength is different.

However, coherent scattering from the particles can cause the radar reflectivities of dual-wavelength radar measurements to become correlated with each other. It may explain the slopes and the differences seen in the scatter plots of the radar reflectivities of cloud and smoke measurements, with reasonable values of the parameters involved. However, the correlation between the radar reflectivities is very tight near the cloud top and seems to be present in adiabatic cores as well. This is an indication that, apart from mixing with environmental air, the inertia of the droplets could also be important for the creation of small-scale fluctuations in droplet concentration.

5.1 Introduction

The field of cloud research develops rapidly at the moment, because climate researchers need more knowledge on clouds to understand how the climate changes as a result of human activities. The cloud feedback in different climate models causes a large part of the differences found in the predictions of future climates [Kattenberg et al., 1996]. Radar plays a unique role in cloud research, as it is the only remote sensing instrument that can measure inside dense clouds. To be able to use the radar measurements in a quantitative way, one must understand the scattering mechanisms involved very well.

Two mechanisms explain most of the reflections measured by radar in the troposphere: incoherent scattering, caused by randomly moving particles, and coherent air scattering, caused by variations in the refractive index of the air. Radar measurements of particles are normally performed in the Rayleigh regime, i.e., with a radar wavelength that is much larger than the particle size. Incoherent scattering in the Rayleigh regime by particles of a given size decreases strongly with radar wavelength. With increasing wavelength, the strength of both the incoherent and the coherent scattering decrease, but the incoherent Rayleigh scattering decreases at a much faster rate (see, e.g., Ottersten (1969)).

Coherent backscattering is caused by spatial variations in the atmospheric radio refractive index on a scale of half the wavelength. The fluctuations in the refractive index of the air can result from fluctuations in water vapour content, temperature and pressure. This coherent scattering from the air is usually called Bragg scattering or clear-air scattering, but these terms are somewhat deceptive. The mechanism is similar to that observed in Bragg scattering from crystals' lattices, but not exactly the same. Also, coherent scattering from fluctuations in the refractive index of the air can occur in clouds, so then the term clear-air scattering is misleading. We will there-

fore denote the coherent scattering from fluctuations in refractive index of the atmospheric gases by *coherent air scattering.*

Spatial variations in the mass concentration of particles can cause *coherent particle scattering,* in a way similar to that of coherent air scattering. This coherent particle scattering was long thought to be insignificant in clouds. Gossard (1979) has calculated that in a cloud, coherent air scattering should be 30 times as strong as coherent droplet scattering, under the assumption that the variations in the density of water vapour and liquid water, when expressed in the same units, are about equal. However, in this chapter it will be made plausible that variations in liquid water density inside clouds can be much larger than those in water vapour density. Furthermore, it will be argued that a correlation between the X-band and the S-band reflectivity factor in simultaneous measurements of developing cumulus clouds performed by Knight and Miller (1998) may be explained by the presence of coherent scattering from the droplets, although the explanation may not be complete yet. Rogers and Brown (1997) observed a correlation between the X-band and UHF radar reflectivities in dual-wavelength radar measurements of a smoke plume caused by an intense industrial fire. It will be shown that the coherent scattering theory may explain this correlation as well.

The outline of this chapter is as follows. In section 5.2, the scattering of radio waves by a volume with particles is discussed and an equation expressing the strength of the coherent backscattering is derived for the case that the spatial fluctuations are caused by turbulent mixing with particle-free air. The measurements of clouds are described and analysed in section 5.3, while those of the smoke are considered in section 5.4. Section 5.5 discusses the material presented in the earlier sections.

5.2 Scattering of radio waves

5.2.1 Coherent air scattering

The theory of scattering from turbulent fluctuations in the refractive index of the air is well developed. The radar cross section per unit volume η (*radar reflectivity*) is given by [Ottersten, 1969]:

$$\eta = \frac{\pi^2}{2} k^4 \varphi_n(\mathbf{k}) \tag{5.1}$$

$\varphi_n(\boldsymbol{k})$ is the space spectrum, i.e., the Fourier transform of the three-dimensional spatial covariance function of refractive index fluctuations. The vector $\boldsymbol{k}$ is the wave number vector in the radar radial direction. Its absolute value is related to the radar wavelength λ through $k=4\pi/\lambda$. Equation (5.1) expresses that the radar sees a narrow continuum of fluctuations on spatial scales around $\lambda/2$. (Not λ, but $\lambda/2$, because

*back*scattering is considered.) When the fluctuations are distributed isotropically in space, $\varphi_n(\boldsymbol{k})$ does not depend on the direction of $\boldsymbol{k}$. For homogeneous isotropic turbulence there exists an inertial subrange in which $\varphi_n(k)$ follows a power law [Tatarski, 1961]:

$$\varphi_n(k) = 0.033 C_n^2 k^{-11/3} \tag{5.2}$$

where C_n^2 is the *structure parameter* of the refractive index fluctuations and is a measure of the strength of the refractive index variations at all scales. Ottersten (1969) points out some other useful relations for isotropic turbulence, e.g., for the refractive index variance spectrum:

$$E_n(k)=4\pi k^2 \varphi_n(k) \tag{5.3}$$

En(k) follows the famous "−5/3-law" of Kolmogorov in the inertial subrange. Combining Eqs. (5.1) and (5.2) and substituting $k=4\pi/\lambda$ leads to the well-known expression:

$$\eta(\lambda) = 0.38 C_n^2 \lambda^{-1/3} \tag{5.4}$$

The coherent air scattering from refractive index fluctuations thus has a weak wavelength dependence in the inertial subrange. Variations in water vapour contribute most to the clear-air scattering in the lower atmosphere [Gossard and Strauch, 1981].

Equation (5.4) is valid for radar wavelengths larger than a critical wavelength λ_c, which is defined as $8\pi\eta_0$, where η_0 is the Kolmogorov microscale [Gossard, 1984a]. The Kolmogorov microscale varies over the range 0.4-1.25 mm in cumulus clouds [Shaw et al., 1999], so that λ_c varies over the range 1-3 cm. Under conditions of weaker turbulence λ_c can sometimes become larger than 10 cm [Gossard et al., 1984b; Gage et al., 1999]. The X-band radar wavelength will be sensitive to turbulence in cumulus clouds most of the time, but under conditions of weaker turbulence even S-band radars may measure outside the inertial subrange.

5.2.2 Particle scattering

If the wave transmitted by a radar goes through a volume containing particles, part of the energy is scattered back to the radar. The waves scattered back by the particles interfere with each other. If the particles are randomly spaced, then some configurations of particle positions will show a net constructive interference, while other configurations have a net destructive interference, but, on average, the interference is zero. The received power, when averaged over all possible configurations of the particle positions, is equal to the sum of the powers scattered back by the individual particles. There is no net interference and one speaks of *incoherent scattering*. The radar reflectivity for incoherent scattering from a volume V with N_v small spherical particles is given by [Battan, 1973]:

$$\eta = \frac{\pi^5 |K|^2}{\lambda^4} \frac{1}{V} \sum_{i=1}^{N_v} D_i^6 \tag{5.5}$$

This expression is valid for particles with diameters D_i much smaller than the wavelength λ. $K = (\varepsilon_r - 1)(\varepsilon_r + 2)^{-1}$, a constant that is determined by the relative permittivity of the particles (ε_r); ($|K|^2$ equals 0.93 for water and a wavelength of 10 cm.)

When the particles are not completely randomly positioned, a net interference may result and the radar reflectivity differs from Eq. (5.5). Several scattering theories are known in the literature that take interference into account. Two of these will be briefly reviewed below and compared with each other. They mainly differ in their way of modeling the coherent scattering.

Siegert and Goldstein (1951) treat the backscattering from ensembles of scatterers. For simplicity they assume that all the scattering particles return a signal of equal magnitude. Defining $N(r)dr$ as the number of scatterers between a distance r and $r+dr$ from the radar, they derive the following formula for the cross section σ:

$$\sigma = |p|^2 \int_0^\infty \bar{N}(r)dr + |p|^2 \left| \int_0^\infty \bar{N}(r) e^{-ikr} dr \right|^2 \tag{5.6}$$

In this equation, p is a proportionality constant that is assumed to be the same for all scatterers, k equals $4\pi/\lambda$, and the overbar denotes a time average. The first term is the *incoherent* contribution to the cross section. It results from the assumption that the scatterers are independent, at least in the sense that the presence of a certain scatterer in any interval does not prejudice the presence of other scatterers. The second term in Eq. (5.6) is called the *coherent* term. It expresses the coherent contribution to the cross section due to *deterministic* spatial variations in the concentration. For example, the backscattering due to large-scale gradients is included in this term. This term equals zero if the time-averaged concentration has no fluctuation on a spatial scale of half the wavelength. The term could be important when, for example, there are sudden spatial changes in refractive index of the atmosphere. The treatment of Siegert and Goldstein is incomplete in the sense that Eq. (5.6) does not include the coherent scattering from spatial fluctuations caused by, for example, turbulent mixing. Turbulent mixing can cause the scatterer concentration to vary both in space and time. This means that the time average of the concentration can be a constant, i.e., independent of position, but still at any particular time there can be a spatial correlation in the concentration, just as there can be a correlation in the values that the concentration has in time, at any given position. The spatial correlation can cause a coherent return. This fact is not included in Eq. (5.6).

Gossard and Strauch (1983) do take spatial correlations in concentration into account. Let $N(\mathbf{r})d\mathbf{r}$ be the number of drops in the position increment between $\mathbf{r}$ and $\mathbf{r}+d\mathbf{r}$. The radar backscattering is proportional to a factor I, which is given by:

$$I = \overline{\left| \int N(\mathbf{r}) \exp(-i\mathbf{k}\cdot\mathbf{r})\, d\mathbf{r} \right|^2} \tag{5.7}$$

The overbar denotes a time average. For backscattering, the wave-number vector $\boldsymbol{k}$ has an absolute value equal to $4\pi/\lambda$ and is directed from the scatterers to the radar. It is again assumed for simplicity that all the scatterers have the same cross section. Gossard and Strauch split $N(\boldsymbol{r})$ into two terms, a deterministic and a random part: $N = N(\mathrm{r}) + \delta N(\mathrm{r})$. The deterministic part gives a contribution identical to the second term on the right-hand side of Eq. (5.6) and will here be further ignored. The random part has a time average which is zero and gives the contribution:

$$I = \iint \overline{\delta N(\mathrm{r})\delta N(\mathrm{r}+\mathrm{l})}\,\mathrm{dr}\exp(-\mathrm{ik}\cdot\mathrm{l})\,\mathrm{dl} \tag{5.8}$$

If a spatial correlation function is defined as follows:

$$C(\mathrm{l}) = \frac{1}{V\cdot\overline{\delta N^2}}\int_V \overline{\delta N(\mathrm{r})\delta N(\mathrm{r}+\mathrm{l})}\,\mathrm{dr} \tag{5.9}$$

where V is the scattering volume, then Eq. (5.8) can be expressed as:

$$I = V\overline{\delta N^2}\int C(\boldsymbol{l})\exp(-\mathrm{i}\boldsymbol{k}\cdot\boldsymbol{l})\,\mathrm{d}\boldsymbol{l} \tag{5.10}$$

The integral in Eq. (5.10) is a Fourier integral and I can be written in terms of the three-dimensional spectrum $\varphi_N(\boldsymbol{k})$ of concentration fluctuations as follows:

$$I = (2\pi)^3 V\varphi_N(\boldsymbol{k}) \tag{5.11}$$

Gossard and Strauch argue that if there is no spatial correlation between neighbouring parcels, the backscattered power is proportional to the total number of scatterers in the scattering volume; the usual incoherent return. This is due to the fact that the number of scatterers in a parcel has a Poisson distribution and this distribution has a variance equal to the mean. The incoherent scattering is the same as the first term in Eq. (5.6). If there is a correlation between the concentrations in parcels that are a certain distance apart, then there will be a coherent contribution to the scattering expressed by Eq. (5.11), which we call the *stochastically coherent* contribution. Its strength depends on the amount of fluctuations on scales close to half a wavelength.

Gossard and Strauch do not mention that the incoherent term is always present, even when there is correlation between concentrations in neighbouring parcels [Erkelens et al., 1999a]. This is caused by the fact that the scatterers do not form a continuum, but are discrete points in space. The scatterer concentration is a function of space and time. Neglecting any large-scale gradients, there is a global mean of the concentration for the entire scattering volume. A process such as turbulent mixing can cause fluctuations in the concentration around the global mean. These fluctuations vary in space and time and show correlation between different parcels. Even when the total number of scatterers in a certain parcel is correlated with the total number in a parcel nearby, the exact position of each *individual* scatterer in the parcel

is random (unless the mutual distances between the particles are completely specified, but that is a deterministic case). Therefore, the number of scatterers in *small* parcels with dimensions of the order of the average distance between the scatterers or smaller has a Poisson distribution with an (ensemble) variance equal to the local expected number of scatterers in the parcels. This local expected value is determined by the physical process that creates the correlations between the number of particles in different parcels. In other words, the turbulence or some other physical process causes correlations between the particle concentrations of the parcels, but on top of that we have the Poisson statistics associated with the random nature of the individual scatterer positions. (This means that the total variance of the number of scatterers in a certain volume is larger than one would expect for completely randomly distributed scatterers, i.e., the scatterer distribution exhibits super-Poissonian variance. Kostinski and Jameson (2000) introduced super-Poissonian variance to describe variations in clouds.)

The incoherent backscattering, due to the random positions of the individual particles, and the coherent backscattering, due to the spatial correlations in locally mean scatterer concentration, are additive. Equation (5.11) describes the coherent backscattering for which the theory for scalar conservative passive additives in homogeneous, isotropic turbulence predicts a $k^{-11/3}$ dependence [Tatarski, 1961]. However, in the theory the concentration is considered as a continuous function in space and time. As explained above, the discrete nature of the particles is the cause why the usual incoherent scattering is also present, in addition to the coherent scattering.

5.2.3 Radar Reflectivity Factor

In this section an expression is derived for the total radar reflectivity factor for the case where fluctuations are caused by turbulent mixing and the particles can be considered as *conservative passive additives.*

The presence of scatterers changes the refractive index of a vacuum. If the particles are small compared with the wavelength, then the refractive index n of the medium as a whole is approximated by (see, e.g., Van de Hulst (1981), page 67):

$$n = 1 + 2\pi\alpha N \tag{5.12}$$

where N is the concentration of scatterers and α the polarizability of the scatterers. For small spheres, the polarizability is given by (Van de Hulst (1981), page 70):

$$\alpha = \frac{1}{8}\frac{\varepsilon_r - 1}{\varepsilon_r + 2} D^3 = \frac{1}{8} K D^3 \tag{5.13}$$

where ε_r is the permittivity of the material of the scatterer. The variance of the refractive index due to variations in scatterer mass concentration is given by:

$$\operatorname{var} n = \frac{\pi^2}{16} |K|^2 \operatorname{var}(ND^3) \tag{5.14}$$

To find an expression for the radar reflectivity for the coherent scattering, var n has to be related to C_n^2 and an expression for var(ND^3) is needed. For this, we make use of the fact that the three-dimensional spectrum of isotropic refractive index fluctuations is normalised such that [Ottersten, 1969]:

$$\int_0^\infty 4\pi k^2 \varphi_n(k)\, dk = \operatorname{var} n \tag{5.15}$$

If it is assumed that: 1) there are no variations on scales larger than L_0, the outer scale of the inertial subrange, and 2) the inner scale is much smaller than the outer scale, then, putting Eq. (5.2) into Eq. (5.15) and integrating from $2\pi/L_0$ to infinity, leads to [Gage and Balsley, 1980]:

$$C_n^2 = 5.5\, L_0^{-2/3} \operatorname{var} n \tag{5.16}$$

Because we want to derive an expression for the *coherent* contribution to the radar reflectivity factor, fluctuations in n due to the random positions of the individual particles are ignored for now. As explained in section 5.2.2, these fluctuations give rise to the usual incoherent scattering term.

Suppose there are two volumes with air containing different concentrations of scatterers, and the scatterers are randomly distributed. If the volumes are mixed by turbulence, spatial fluctuations in the concentration are generated. The strength of the fluctuations will be larger when the difference in initial concentrations is larger. In the extreme case that one of the volumes contains all the scatterers and the other none, both the mean concentration and the amplitude of fluctuations in the mixing region are proportional to the initial concentration. This may occur, for instance, in the case of mixing of cloudy air with clean air, as happens at the sides and top of convective clouds. One can assume that the standard deviation in the mass concentration of scatterers is proportional to the mean mass concentration, with a factor of proportionality that will be called β (i.e., the *relative standard deviation* of the mass concentration). It depends on the ratio of the volumes of environmental and cloudy air that mix, and on the rate with which fluctuations are created and removed. For the variance one can write $\operatorname{var}(ND^3)=\beta^2(\bar{N})^2D^6$, where it has been assumed for simplicity that all scatterers have the same diameter D. Equation (5.5) shows the incoherent radar reflectivity and combining Eqs. (5.4), (5.14), and (5.16) gives the coherent radar reflectivity. Combining incoherent and coherent terms and multiplying by $\lambda^4/\pi^5|K|^2$ gives the total *radar reflectivity factor* Z:

$$Z = \bar{N}D^6 + 4.2\times10^{-3} L_0^{-2/3} \beta^2 (\bar{N})^2 D^6 \lambda^{11/3} \tag{5.17}$$

The coherent backscattering depends on the square of the concentration. The incoherent radar return depends linearly on the concentration. Both the incoherent and coherent returns depend on the diameter to the power of six. The coherent term in Eq. (5.17) becomes increasingly important for longer wavelengths and higher particle densities. If we consider the following range of values of the parameters:

β: 0.05–1 (see section 5.3.2), L_0: 10–500 m, and N: 100–1000 cm^{-3}, then the ratio of the coherent to the incoherent term of Eq. (5.17) spans the following range: for a wavelength of 3 cm the ratio lies between −44 dB and +4 dB, for 10 cm between −24 dB and +23 dB, and for 30 cm between −7 dB and 40 dB. Hence, coherent particle scattering might in some cases be significant at X-band, it can very well be important at S-band, and even more so for UHF radars.

Equation (5.17) is applicable when the fluctuations in particle concentration are caused by mixing between air volumes having large differences in concentration. Several recent studies show that fluctuations in particle concentration can appear in turbulent flows due to the inertia of the particles, without the need for mixing with air with a different mean concentration (see, e.g., Squires and Eaton (1991), Vaillancourt (1998), Shaw et al. (1999)). The particles are preferentially concentrated by coherent turbulent structures. The importance of the effect in clouds is, however, still under debate (see, e.g., Grabowski and Vaillancourt (1999)). The fluctuations that are found with this *preferential concentration mechanism* generally appear on scales of a few centimetres. The mechanism works for a limited range of particle masses: very light particles just follow the flow, while for heavier particles gravitational sedimentation becomes important. If the particles are too heavy, they just fall through the turbulent structures and there is not enough interaction. The total radar reflectivity factor for a volume where the preferential concentration mechanism is operating will also have an incoherent component $\overline{N}\overline{D^6}$ and a coherent component proportional to $(\overline{N})^2\overline{D^6}$, but the wavelength dependence and the strength of the coherent component could differ much from Eq. (5.17).

5.2.4 *Dual-frequency measurements*

If dual-frequency measurements of purely coherent scattering are compared, a difference between the measured radar reflectivities will be found. If both wavelengths fall within the inertial subrange, this difference can be calculated from:

$$Z_1 = Z_2 + 10 \cdot \log\left(\frac{\lambda_1}{\lambda_2}\right)^{11/3} \tag{5.18}$$

Z_1 and Z_2 are the reflectivity factors for the two wavelengths, expressed in dBZ, and *log* is the logarithm of base 10. For example, in sections 5.3 and 5.4 dual-wavelength measurements of developing cumulus clouds and smoke are discussed. The wavelengths used are 3 cm and 10 cm for the clouds and 3.2 cm and 33 cm for the smoke. Equation (5.18) predicts differences of 19 dBZ and 37 dBZ for purely coherent scattering for these pairs of wavelengths.

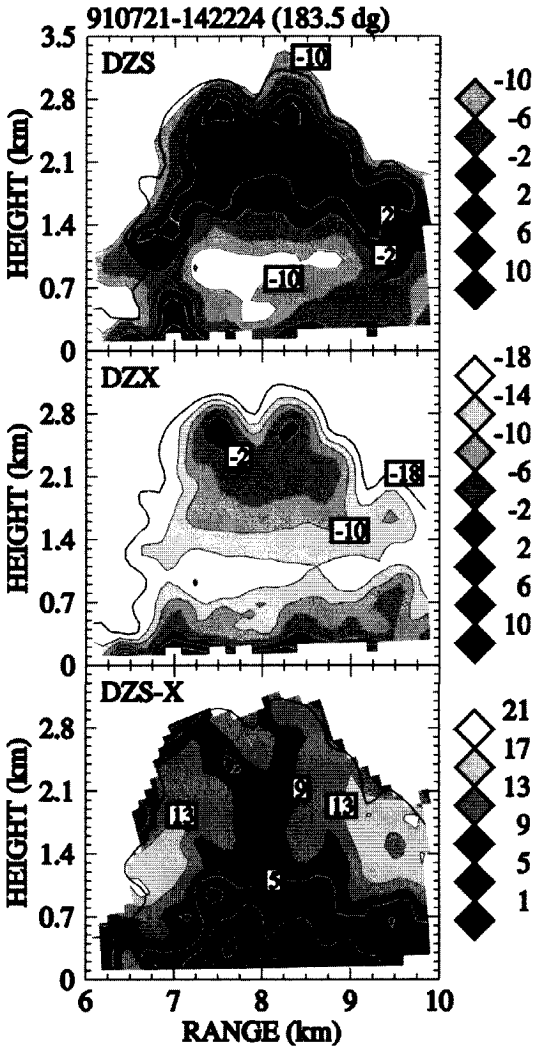

Figure 5.1. An example of a developing cumulus cloud. DZS and DZX are the S-band and X-band reflectivity factors, respectively, expressed in dBZ. DZS-Z is their difference. DZS shows a large weak-echo region near cloud base and some signs of a mantle echo. DZX shows very clear flat echo bases. (Fig. 12 from Knight and Miller (1998))

Dual-frequency measurements of purely incoherent scattering by small spheres should by definition give a difference of 0 dB. If both incoherent and coherent scattering contribute to the return, the measured difference should lie somewhere between 0 dBZ and the value predicted by Eq. (5.18). This happens, for example,

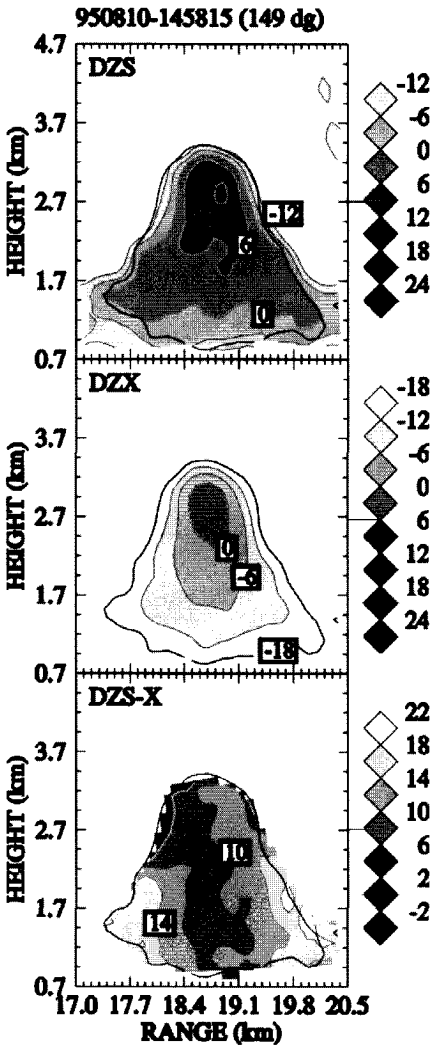

Figure 5.2. A developing cumulus cloud, showing a strong correlation between DZS and DZX, which cannot be explained in terms of the traditional scattering mechanisms of incoherent particle scattering and coherent air scattering. DZS-X is near 10 dBZ in a large part of the cloud. (Fig. 10 (c) from Knight and Miller (1998)).

when the radar return at the longer wavelength is dominated by coherent scattering from humidity and temperature variations and the return at the shorter wavelength by incoherent scattering from particles.

Values between the limits are observed for the majority of the measurements of developing cumulus clouds [Knight and Miller, 1998], and for smoke [Rogers and

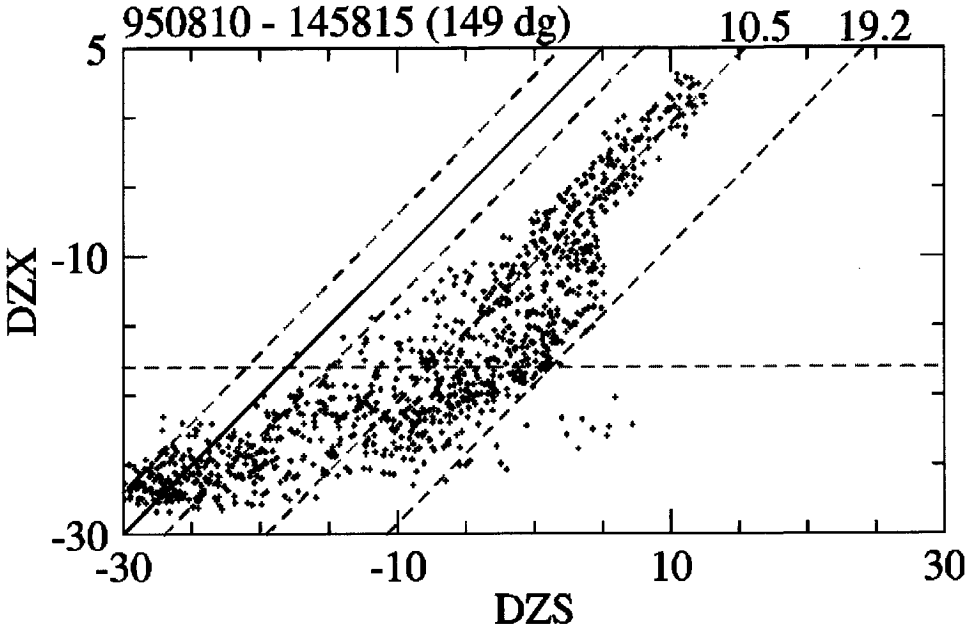

Figure 5.3. Scatterplot of DZS versus DZX for the cloud of Fig. 5.2. The dotted horizontal line at –18 dBZ is a conservative value of the noise level of the X-band radar (Figure 11(c) from Knight and Miller (1998)).

Brown, 1997]. The puzzling aspect of these measurements is that both sets of measurements show a correlation between the reflectivity factors at two wavelengths, which one does not expect when the origins of the radar returns are different. The measurements will be discussed further in the following sections.

5.3 Dual-wavelength measurements of cumulus clouds

5.3.1 Description of the measurements

In a recent article, Knight and Miller (1998) discuss measurements of developing cumulus clouds, performed with 2 radars: an X-band radar with a wavelength of 3-cm and an S-band radar with a wavelength of 10 cm. Two examples are shown in Figs. 5.1 and 5.2. The measurements were obtained during the CaPE and SCMS campaigns, Florida, in July and August 1991 and 1995. In these figures, DZS, DZX and DZS-X denote the radar reflectivity factor at S-band, at X-band and their difference, respectively. Most measurements could be explained by the traditional theory. For example: Coherent air scattering at the borders of the cumulus clouds is due to

mixing of the humid cloudy air with dryer environmental air and can cause *mantle echoes* with differences in the reflectivity factors close to 19 dBZ, the value expected for coherent scattering at these wavelengths; or, when drizzle or rain droplets are present, the Rayleigh scattering from them can dominate, causing equal reflectivity factors. In these cases there is a correlation in the returns, as the scattering process dominating both wavelengths is the same. Also cases were observed in which the 10-cm radar measured coherent scattering, while the 3-cm radar measured incoherent scattering, and there was no correlation between the reflections.

However, often there was a correlation in the X- and S-band reflectivity factors, but their difference was not equal to 0 dBZ (the value for purely incoherent scattering) or 19 dBZ (for purely coherent scattering). For example, in Fig. 5.3 some of the X- and S-band reflectivity factors lie on a line with a slope of one with a difference of about 10 dBZ (but other offsets have been observed as well). No simple explanation for this can be found from the conventional theories of incoherent droplet scattering and coherent air scattering. The phenomenon was especially noticeable on days where the air outside the cloud was very humid, because the effect was not obscured then by coherent scattering due to water vapour fluctuations at the borders of the cloud. In section 5.3.2, a possible explanation for this correlation will be presented in terms of coherent scattering from the droplets.

At the cloud bases of the developing cumulus clouds, Knight and Miller reported two important features: *flat echo bases* and *weak-echo regions*. Flat echo bases are occasionally observed; they are very flat and horizontal bottoms in the X-band echo contours, similar to the visually flat cloud base at the condensation level. Figure 5.1 shows a clear example. Here the S-band reflectivity pattern also shows a flat echo base, but this is not always the case. Knight and Miller interpret the flat echo bases as the result of unmixed adiabatic ascent.

The base of the cloud in Fig. 5.1 is probably somewhere between 400 m and 700 m. Near the cloud base the S-band measurement shows a region with lower reflectivities. This region is called *weak-echo region* and is seen in nearly all the actively growing clouds. The bottom frame shows that the S-band reflectivity is dominated by coherent scattering, so the weak-echo region is a minimum in the coherent return at S-band. It is also sometimes present at X-band, but is then much less pronounced. The weak-echo region at S-band extends almost to the ground here. The weak-echo regions often have reflectivity factors in the order of -20 dBZ.

Another feature reported by Knight and Miller is that on some days it is fairly common that the difference in reflectivity factors in the mantle echoes is not 19 dBZ, but several dBs higher. This indicates a slope steeper than -5/3 for the variance spectrum of the refractive index variations. It may be that the X-band radar measured in the dissipation range, but a steeper slope may also be due to the effect of evaporation and condensation on the slope of the variance spectrum of humidity variations, as will be explained in section 5.3.3.

5.3.2 Coherent particle scattering in cumulus clouds

This section will show quantitatively that coherent droplet scattering in cumulus clouds can be significant compared to incoherent droplet scattering, and that coherent droplet scattering may explain the correlation in X- and S-band reflectivities that was found in the measurements of the developing cumulus clouds.

For the 10-cm radar used in the cumulus study Eq. (5.17) becomes:

$$Z(10\text{ cm}) = \bar{N}D^6 + 9.0\times10^{-7}\,\beta^2\,L_0^{-2/3}(\bar{N})^2 D^6 \qquad (5.19)$$

In-situ aircraft measurements of the droplet concentrations performed during CaPE in clouds very similar to the ones described above showed droplet concentrations reaching 800-900 cm^{-3} near cloud base [Paluch et al., 1996]. There is much uncertainty about the values of β and L_0, and they may be related. A value of 10 m for L_0 was used by VanZandt et al. (1978) for the free atmosphere, but this value is probably much too small for the developing cumulus clouds considered here. Davis et al. (1996) measured the spatial fluctuations of liquid water content in marine stratocumulus clouds using a King hot-wire probe and Davis et al. (1999) used a Particulate Volume Monitor for that purpose in broken stratocumulus decks with embedded towering cumulus. By dividing the standard deviation of the liquid water content measurements by their mean value, an estimate of the relative standard deviation β is obtained. This yields values between 0.05 and 0.58. A difference in the reflectivity factors of about 10 dBZ has been observed. Such a difference would result for example for L_0=150 m and β=0.6. This result shows that coherent droplet scattering *can be significant* in S–band measurements of cumulus clouds. In Fig. 5.2, the strongest correlation between the radar reflectivity factors at X-band and at S-band occurs for values of the X-band reflectivity factor that lie between about -5 dBZ and 2 dBZ. For a concentration of 800 cm^{-3}, this would mean droplet diameters between 27 μm and 35 μm (when the droplet size distribution is assumed to be mono-disperse).

Since both the incoherent term and the coherent term in Eq. (5.19) depend on D^6, we could explain the observed correlation by assuming that the differences between the measured data points are mainly due to an increase in the average diameter of the particles with height: the ascending air becomes colder and the droplets grow because of condensation.

Fluctuations on scales of about 5 mm to 5 cm have been found experimentally from FSSP data [Baker, 1992] in cumulus cloud regions which were picked by the eye to be homogeneous on large scales. Such cm-scale fluctuations might be caused by the preferential concentration mechanism mentioned earlier. The coherent scattering from such fluctuations can already be significant for very small values of the relative standard deviation β, if the fluctuations appear only on the small scales and not on larger scales. A very rough estimate can be obtained by assuming that the $-5/3$ law is valid for these cm-scale fluctuations. Then one may set L_0 in Eq. (5.19) equal to 5 cm

to compute a coherent contribution that is about 10 dB stronger than the incoherent contribution for β as small as 0.04.

5.3.3 Coherent air scattering in clouds

In addition to the incoherent and coherent contributions to the radar reflectivity from particles, the air also supplies a coherent contribution. The refractive index of clear (i.e., particle-free) air depends on pressure, temperature and humidity. Fluctuations in water vapour concentration dominate the scattering by clear air in the lower atmosphere [Gossard and Strauch, 1981]. Gossard (1979) has compared the relative magnitudes of coherent scattering from water vapour fluctuations in clouds with that of coherent scattering from droplets. He derives for the variations in refractive indices n_v (due to vapour variations) and n_l (due to liquid variations):

$$\begin{aligned} \operatorname{var} n_v \times 10^{12} &\approx 58.5 \operatorname{var} Q_v \\ \operatorname{var} n_l \times 10^{12} &\approx 2.09 \operatorname{var} Q_l \end{aligned} \tag{5.20}$$

respectively.

Q_v and Q_l are the water vapour and liquid water mixing ratios (grams per kilogram of dry air) and "var" designates the spatial variance. Gossard and Strauch (1983) state that within a cloud in steady state at saturation with no precipitation removing water from the cloud and minimal entrainment, it seems reasonable to assume that var Q_v is equal to var Q_l. Since the coherent scattering is proportional to var n, the contribution to coherent scattering from water vapour fluctuations is about 30 times stronger than coherent scattering from droplets for equal variations in water vapour content and liquid water content (see Eqs. (5.4) and (5.16)).

There are several mechanisms that influence the strength of the water vapour and liquid water fluctuations [Erkelens et al., 1999b] and it will be argued below that, in clouds, the variations in water vapour can be much smaller than those in liquid water. Consequently, in some cases coherent scattering from the cloud droplets can dominate coherent scattering from water vapour, contrary to common belief.

At the top and sides of convective clouds the cloudy air mixes with environmental air, leading to *mantle echoes* on the reflectivity patterns for longer wavelengths [Knight and Miller, 1998]. The environmental air does not contain water droplets, so mixing can cause large fluctuations in liquid water content. If, in addition, the air outside the cloud is very humid, the resulting fluctuations in the water vapour content can be smaller than those in the liquid water content. Environmental air may penetrate deeply into the cloud, indicated by the thickness of mantle echoes on dry days. The mantle echoes can sometimes be as thick as 1 km at the top of cumulus clouds.

Condensation and evaporation also influence fluctuations in the water vapour content and liquid water content. Condensation and evaporation will always tend to

bring the relative humidity toward about 100% and are more effective for larger deviations from saturation. So this will reduce fluctuations in water vapour content but not necessary the fluctuations in liquid water content. Rogers et al. (1994) report a case where the clear-air echo of a turbulent layer intensified when light rain fell through the layer. They analyse in detail the effect of evaporation of rain on C_n^2 and conclude that the thermodynamic effect of the rain on the layer is to reduce the reflectivity, contrary to what is observed. We wonder whether a coherent scattering contribution from the smallest rain droplets may cause the observed intensification.

The wavelength dependency of $\lambda^{-1/3}$ in Eq. (5.4) is valid for any *conservative passive additive* (CPA) in homogeneous isotropic turbulence in equilibrium [Tatarski, 1961]. For a CPA, the theory says that the fluctuations are generated at large scales and are passed on completely to smaller scales. Only at the smallest scales they are removed (by molecular diffusion). An interesting effect of condensation and evaporation is that it may affect the slope of the spatial spectrum of water vapour and liquid water fluctuations. (Water vapour content and liquid water content are not CPAs and the "-5/3 law" may not be valid.) Condensation and evaporation tend to reduce fluctuations in water vapour content. (This will happen at all scales, but more strongly at larger scales, because the largest deviations from saturation appear at the largest scales). Due to this sink, not all of the fluctuations will be passed on to smaller scales. This means that the slope of the water vapour spatial spectrum could be steeper than that of a CPA.

An updraft may also reduce humidity fluctuations. If there is a mean upward motion of the air then the relative humidity in initially droplet free air will increase until saturation is reached. Then new droplets may form due to condensation. The cloudy air will remain at saturation, but the droplets will grow due to condensation. So, the effect of an updraft would be to reduce fluctuations in water vapour and at the same time increase fluctuations in liquid water, until saturation is reached in the clear air. This may lead to large fluctuations in liquid water concentration and slopes of the spatial variance spectra that differ from –5/3.

It is interesting to note that changes in the slope of the variance spectra can also occur when chemical reactions take place [Corrsin, 1961; Pao, 1964]. The methods used in these references to compute the changes in the spectra might be applied to the clouds, but that is outside the scope of this work.

There are also experimental indications of a deviation from the –5/3 law. Indications of a flatter slope have been found in a forward scattering experiment performed by Gossard and Strauch (1981). The dual-wavelength measurements of Gage et al. (1999) also show signs of a flatter slope. Davis et al. (1999) performed measurements of the liquid water spatial variance spectrum with a Particulate Volume Monitor in stratocumulus clouds. The spectrum shows a slope that is less steep than –5/3 for scales smaller than a few meters.

Diffusion and sedimentation influence fluctuations in water vapour content or liquid water content as well. Diffusion reduces small-scale fluctuations in water vapour content, but this mechanism is negligible for water droplets. However, fluctuations in liquid water content may be removed by droplet sedimentation. The broader the droplet size distribution is, the larger the differences in fall velocities of the droplets, and the more effective sedimentation is in reducing variations in liquid water content.

All the mentioned processes can influence the strength of the fluctuations in water vapour content and liquid water content. A quantitative estimate of the effects is difficult because each of the processes involved has its own time scale. Estimates for some of the time scales involved can be found in, e.g., [Grabowski, 1993].

Due to the effects discussed above, fluctuations in liquid water content may exist for longer times than those in water vapour content and may be much stronger. They may therefore penetrate the cloud more deeply. Mixing could be effective over larger parts of the clouds than might be concluded on the basis of the thickness of the mantle echo. For, the mantle echo mainly represents the area where fluctuations in water vapour content contribute strongly to the S-band reflectivity. Its apparent thickness, however, depends on the contrast in humidity between the saturated cloudy air and the subsaturated environmental air, on how fast humidity variations are reduced, and on the strength of the incoherent contribution.

Simultaneous measurements on centimetre scales of the water vapour and liquid water concentrations are needed to prove that the fluctuations in water vapour are really much smaller than those in liquid water. For a complete description, also the covariances between humidity, temperature and liquid water content should be measured.

Some experimental evidence exists on the possibility of significant coherent particle scattering. Politovich and Cooper (1988) performed measurements of supersaturation in 147 cloud regions. The average supersaturation was near 0 %, with relative standard deviations of 0.4 % in 80 percent entrained air and 0.1 % in the core of cumulus clouds. The regions giving a high correlation between S- and X-band reflectivities in the article by Knight and Miller (1998) are about 2 km above cloud base. An *adiabatic* cloud with a temperature of 25 degrees Celsius and a pressure of 930 mb at cloud base will have a water vapour content of about 17 g/m^3 and a liquid water content of about 6 g/m^3 at 2 km above cloud base. Equations (5.4), (5.16) and (5.20) show that if coherent particle scatter is to dominate coherent air scatter the spatial standard deviations of the variations in liquid water content should be $\sqrt{(58.5/2.09)} = 5.3$ times as large as those in water vapour content. The measurements of Politovich and Cooper would mean that the relative variations in liquid water content should dominate the scattering when they are above 6 % for the entrained region and about 1.5 % in the core of cumulus clouds. (Lower in the cloud the ratio of water vapour content to liquid water content will be higher, thus coher-

ent *air* scatter will be more important near the cloud base.) Davis et al. (1996, 1999) found relative liquid water variations in stratocumulus clouds between 5 % and 58 % of the mean value. It is therefore very well possible that the coherent droplet scattering is stronger than the coherent air scatter in clouds, except close to the cloud base. Venema et al. (1999) have analysed in more detail for which radar frequencies, how often and in which types of clouds coherent particle scattering may be important.

5.4 Dual wavelength measurements of smoke

5.4.1 Description of the measurements

Another measurement showing a puzzling correlation between the radar measurements at two wavelengths was reported by Rogers and Brown (1997). They measured a smoke plume from a large industrial fire with two vertically pointing radars, a UHF profiler (wavelength 33 cm) and an X-band radar (3.2 cm). The smoke was caused by a burning paint factory, located 10 km away from the radars. The factory was burnt to the ground. The plume was overhead the radars about 20 minutes after the fire started.

With these wavelengths, purely coherent scattering would give a 37 dBZ difference in the reflectivity factors. A scatter plot of the reflectivity factors shows that the majority of the points lie between the 0 dBZ difference line and the 37 dBZ difference line, see Fig. 5.4. There is a correlation between the reflectivity factors of both radars. The points lie roughly on a line of slope one half (a least-squares linear fit gives a slope of 0.4). These measurements may also be explained in terms of coherent particle scattering (section 5.4.2). Curiously, a Vaisala CT-12K ceilometer detected little or nothing of the smoke plume.

5.4.2 Coherent particle scattering in smoke

Rogers and Brown (1997) investigate two possible explanations for the difference in the observed reflectivity factors: 1) the presence of cm-sized particles and 2) a strongly perturbed structure of atmospheric refractivity.

Large particles: There are indications that the smoke plume contained a small number of large particles. These indications are: a grainy pattern of high-resolution X-band reflectivity, a predominance of downward velocities in the order of 1 m/s and the fact that a Vaisala CT-12K ceilometer did not detect the plume. If the particles are so large that the Rayleigh approximation is not valid at X-band, then the UHF reflectivity will exceed the X-band reflectivity. Rogers and Brown show that a very small number of cm-sized particles can explain the magnitude of the differ-

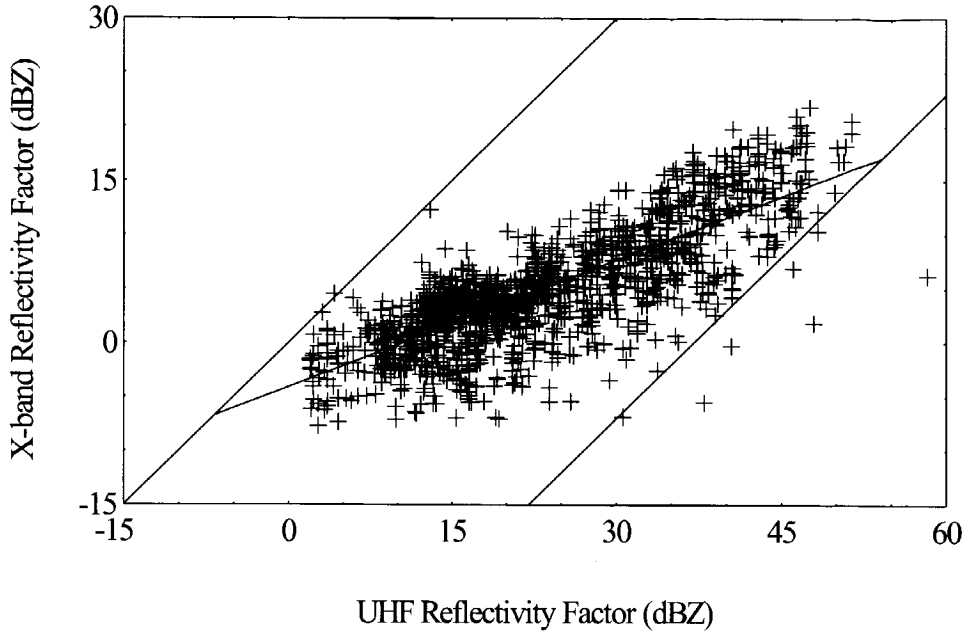

Figure 5.4. Scatterplot of UHF versus X-band reflectivity factors for the smoke measurement described in Rogers and Brown (1997). The reflectivity factors are correlated: they cluster around a line with a slope of about 1/2.

ences that occur if the particles are too large to satisfy the Rayleigh approximation at UHF, but in order to explain the correlation in the measurements the concentration of the particles must increase with their size, which seems unlikely.

It is puzzling that the ceilometer did not detect the plume, because even if the plume contained a small number of large particles, it would probably still contain small particles in much higher concentrations.

Strong clear-air scatter: The heat generated by the fire and gases that are produced could increase the value of C_n^2 to values considerably higher than ordinary observed in the atmosphere, but again it is difficult to explain the correlation.

We suggest that the correlation and the slope near one half can be explained by coherent particle scattering. For wavelengths of 3.2 cm and 33 cm, respectively, Eq. (5.17) becomes:

$$\begin{aligned} Z(3.2\text{ cm}) &= \bar{N}D^6 + 1.4\times10^{-8}\beta^2 L_o^{-2/3}(\bar{N})^2 D^6 \\ Z(33\text{ cm}) &= \bar{N}D^6 + 7.2\times10^{-5}\beta^2 L_o^{-2/3}(\bar{N})^2 D^6 \end{aligned} \tag{5.21}$$

Because the first term on the right-hand side of these equations is a linear function of number density and the second term a quadratic function of number density,

there will be some range of values of the number density, where the 3-cm signal is mainly due to incoherent scattering and the 33-cm signal is dominated by coherent scattering. If the number density varies within this range in the plume, then a slope of one half can be produced on a log-log scatter plot of UHF versus X-band reflectivity. Variations in the other variables could be responsible for the considerable scatter in the measurements shown in Fig. 5.4. There is some question about the origin of the variations in concentration. They could be due to spatial and temporal variations in turbulent mixing (in which case one may expect considerable variations in the parameters β and L_0). It could also be that the main variations in concentration are due to variations in the amount of smoke generated by the fire.

The order of magnitude of particle density and diameter can be estimated. If β is taken to be unity and L_0 equal to 10 m, then it can be calculated with Eq. (5.21) that concentrations ranging from 2 cm^{-3} to 60 cm^{-3} and a diameter of about 90 μm are needed to explain Fig. 5.3. This must be considered a very rough estimate, however, because of the uncertainty in the values of the parameters, but the numbers seem reasonable.

It is curious that the ceilometer detected little or nothing of the smoke plume. One would expect this lidar to detect a cloud consisting of particles with the calculated diameters and number densities. It could be that the lidar backscatter from the smoke plume was reduced because the particles were strongly absorbing at the lidar wavelength. Furthermore, the boundaries of the smoke plume are probably much less sharp than those of the bottom of a water cloud, so a significant part of the power may already have been attenuated before the light reached the position with a relatively high backscattering.

5.5 Discussion

Equation (5.17), which expresses the total equivalent radar reflectivity factor for incoherent and coherent scattering from particles, has been derived assuming that the fluctuations in particle mass density are due to the mixing with clean air. Coherent particle scattering may then explain the correlation in the cloud and smoke measurements with particle concentrations and diameters that are reasonable.

However, fluctuations in particle concentration may also arise due to the preferential concentration mechanisms without the need for mixing. The question is: what is the dominating mechanism causing the fluctuations in particle density?

Most of the points in the scatter plot of Fig. 5.4 show differences between X-band and UHF reflectivities that lie between 0 dBZ and 37 dBZ, the limiting values for purely incoherent and purely coherent scattering due to turbulent mixing, respectively. This is an indication that the variations are created at scales considerably

larger than half the wavelength of the UHF radar and thus mixing with clean air is probably the dominating mechanism for creating the fluctuations in smoke density.

For the clouds, the situation is less clear. The correlation in Figs. 5.2 and 5.3 is strongest near the cloud top, where the scattering from the droplets is largest. Mixing with environmental air could be important for the correlation between the X- and S-band reflectivities there, because the top of the cloud is exactly the place where strong mixing takes place as the thick mantle echoes on dry days indicate.

An argument against mixing being a dominant mechanism in the *core* of the clouds is the occurrence of flat echo bases in the lower parts of the clouds at X-band. These are interpreted as unmixed adiabatic ascent. The weak-echo regions at the base of the clouds could also be an indication of that.

The correlation near the top of the cloud in Fig. 5.3 is remarkably strong. Any fluctuations in the parameters β and L_0 would decrease the correlation if the S-band reflectivity is dominated by the second term of (5.17) and the X-band reflectivity by the first term. The combined variations in β, L_0 and concentration should not be larger than about a factor of 3 to explain the high correlation shown in Fig. 5.3. Variations in these parameters would *all* lead to a slope of 1, and a very strong correlation, if *both* DZS and DZX were dominated by coherent scattering. The problem becomes then to explain the 10 dBZ difference between DZS and DZX, which means a slope of the variance spectrum close to zero, at least at cm-scales.

The correlation in Fig. 5.3 is less strong for DZS smaller than about 5 dBZ. DZS–X has values larger than about 10 dBZ, due to the presence of coherent scattering from humidity fluctuations, but also values *smaller* than 10 dBZ are present. Unless this is caused by some artefact such as the presence of insects, it means that the phenomenon causing the peculiar correlation is less important near cloud base.

If the X-band return would also be dominated by coherent scatter, the droplet concentration estimated from a scatter plot of the X-band reflectivity versus height, assuming an adiabatic liquid water profile, would be underestimated, and the droplet diameters would be overestimated. In fact, there is some evidence for this. Knight and Miller estimate a concentration in the order of 100 cm^{-3} in one example, where they assume a narrow, symmetric droplet size distribution. Using an asymmetric distribution, such as a gamma or a lognormal distribution, would increase the estimated value, but an unrealistically broad spectrum has to be assumed to get a value as high as the 800-900 cm^{-3} found with an FSSP in some of the clouds of CaPE [Paluch et al., 1996].

5.6 Summary and concluding remarks

Besides coherent scattering from variations in refractive index of the air (clear-air/Bragg scattering) and incoherent particle scattering (Rayleigh scattering), coher-

ent scattering by ensembles of particles may also be important in explaining radar measurements of the atmosphere. Coherent particle scattering can considerably enhance the reflections from small cloud droplets and aerosols. Scattering from variations in humidity is probably less important in clouds than was thought until now.

In parts of cumulus clouds coherent scattering from the droplets may be a dominating scattering mechanism, especially at long wavelengths. Two possible mechanisms for creating fluctuations in particle mass density have been considered: mixing with environmental air and the preferential concentration mechanism. The former can create fluctuations on a wide range of scales, while the latter is believed to create fluctuations only on small scales. There are indications that coherent droplet scattering is important even at X-band and also in the core of the clouds. This is an indication that the preferential concentration mechanism plays a role. Measuring also with a radar with a longer wavelength would provide information about the range of scales involved, while a radar with a shorter wavelength could tell whether coherent scattering is present at X-band.

Big fires are known to be very efficient radar scatterers [Rogers and Brown, 1997; Banta, 1992]. This may be due to coherent scattering by the smoke particles. Mixing with clean air is likely of importance for creating spatial fluctuations in smoke density.

For the development of a more complete theory of coherent particle scattering, in-situ measurements of fluctuations on small scales are needed. Also simulations with cloud models with a solid physical basis can help improve the understanding of the scattering of radar waves by clouds. Together, theory, measurements and modelling may contribute to an improved understanding of processes in clouds such as turbulence, entrainment and mixing, the evolution of cloud droplet size spectra and warm rain formation.

Acknowledgement

We are indebted to R.R. Rogers, W.O.J. Brown, C.A. Knight and L.J. Miller for useful discussions and providing us with data and figures. We thank W. Klaassen for carefully reading an early version of the manuscript. This research was supported by the Dutch Technology Foundation and the Dutch national research program on global air pollution and climate change.

References

Baker, B.A. Turbulent entrainment and mixing in clouds: a new observational approach. *J. Atmos. Sci.*, **49**, pp. 387-404, 1992.

Banta, R.M., L.D. Olivier, E.T. Holloway, R.A. Kropfli, B.W. Bartram, R.E. Cupp, and M.J. Post. Smoke-column observations from two forest fires using Doppler lidar and Doppler radar. *J. Appl. Met.*, **31**, pp. 1328-1349, 1992.

Battan, L.J. *Radar Observation of the Atmosphere.* University Chicago Press, 324 p., 1973.

Corrsin, S. The reactant concentration spectrum in turbulent mixing with a first-order reaction. *J. Fluid Mech.*, **11**, pp. 407-416, 1961.

Davis, A., A. Marshak, W. Wiscombe, and R. Cahalan. Scale invariance of liquid water distributions in marine stratocumulus. Part I: spectral properties and stationarity issues. *J. Atmos. Sci.*, **53**, pp. 1538-1558, 1996.

Davis, A.B., A. Marshak, H. Gerber, and W.J. Wiscombe. Horizontal structure of marine boundary layer clouds from centimetre to kilometer scales. *J. Geophys. Res.*, **104**, pp. 6123-6144, 1999.

Doviak, R.J., and D.S. Zrnic. *Doppler Radar and Weather Observations.* Academic Press, San Diego, 562 p., 1993.

Erkelens, J.S., V.K.C. Venema, and H.W.J. Russchenberg. Coherent particle scatter in smoke and cumulus clouds. *Proc. IEEE Geosci. and Remote Sensing Symp.*, 28 June – 2 July, Hamburg, Germany, pp. 687-689, 1999a.

Erkelens, J.S., V.K.C. Venema, and H.W.J. Russchenberg. Coherent particle scatter in developing cumulus clouds. *Proc. Int. Conf. Radar Meteorology*, American Meteorological Society, 12 – 16 July, Montreal, Canada, pp. 904-907, 1999b.

Gage, K.S., and B.B. Balsley. On the scattering and reflection mechanisms contributing to clear air radar echoes from the troposphere, stratosphere, and mesosphere. *Radio Sci.*, **15**, pp. 243-257, 1980.

Gage, K.S., C.R. Williams, W.L. Ecklund, and P.E. Johnston. Use of two profilers during MCTEX for unambiguous identification of Bragg scattering and Rayleigh scattering. *J. Atmos. Sci.*, **56**, pp. 3679-3691, 1999.

Gossard, E.E. A fresh look at the radar reflectivity of clouds. *Radio Sci.*, **14**, pp. 1089-1097, 1979.

Gossard, E.E., and R.G. Strauch. The refractive index spectra within clouds from forward-scatter radar observations. *J. Appl. Met.*, **20**, pp. 170-183, 1980.

Gossard, E.E., and R.G. Strauch. *Radar Observation of Clear Air and Clouds.* Elsevier Science Publishers, Amsterdam, 280 p., 1983.

Gossard, E.E., R.B. Chadwick, T.R. Detman, and J.E. Gaynor. Capability of surface-based clear-air Doppler radar for monitoring meteorological structure of elevated layers. *J. Appl. Meteor*, **23**, pp. 474-485, 1984a.

Gossard, E.E., W.D. Neff, R.J. Zamora, and J.E. Gaynor. The fine structure of elevated refractive layers: Implications for over-the-horizon propagation and radar sounding systems. *Radio Sci.*, **19**, pp. 1523-1533, 1984b.

Grabowski, W.W. Cumulus entrainment, fine-scale mixing, and buoyancy reversal. *Q. J. R. Meteorol. Soc.*, **119**, pp. 935-956, 1993.

Grabowski, W.W., and P. Vaillancourt. Comments on 'Preferential Concentration of Cloud droplets by Turbulence: Effects on the Early Evolution of Cumulus Cloud Droplet Spectra.' *J. Atmos. Sci.*, **56**, pp. 1433-1436, 1999. See also reply on pp. 1437-1441.

Kattenberg, A. et al. Chapter 6 in *Climate Change 1995,* J.T. Houghton et al. (Eds.), Cambridge University Press., 1996.

Knight, C.A., and L.J. Miller. Early radar echoes from small, warm cumulus: Bragg and hydrometeor scattering. *J. Atmos. Sci.*, **55**, pp. 2974-2992, 1998.

Kostinski, A.B., and A.R. Jameson. On the spatial distribution of cloud particles. *J. Atm. Sci.*, pp. 901-915, 2000.

Ottersten, H. Radar backscattering from the turbulent clear atmosphere. *Radio Sci.*, **4**, pp. 1251-1255, 1969.

Paluch, I.R., C.A. Knight, and L.J. Miller. Cloud liquid water and radar reflectivity of nonprecipitating cumulus clouds. *J. Atmos. Sci.*, **53**, pp. 1587-1603, 1996.

Pao, Y.-H. Statistical behavior of a turbulent multicomponent mixture with first-order reactions. *AIAA J.*, **2**, pp. 1550-1559, 1964.

Pinsky, M.B., A.P. Khain, and Z. Levin. The role of inertia of cloud drops in the evolution of the spectra during drop growth by diffusion. *Q. J. R. Meteorol. Soc.*, **125**, pp. 553-581, 1999.

Politovich, M.K., and W.A. Cooper. Variability of the supersaturation in cumulus clouds. *J. Atmos. Sci.*, **45**, pp. 1651-1664, 1988.

Rogers, R.R., S.A. Cohn, W.L. Ecklund, J.S. Wilson, and D.A. Carter. Experience from one year of operating a boundary-layer profiler in the center of a large city. *Ann. Geophysicae*, **12**, pp. 529-540, 1994.

Rogers, R.R., and W.O.J. Brown. Radar observations of a major industrial fire. *Bull. Amer. Meteor. Soc.*, **78**, pp. 803-814, 1997.

Shaw, R.A., W.C. Reade, L.R. Collins, and J. Verlinde. Preferential concentration of cloud droplets by turbulence: effects on the early evolution of cumulus cloud droplet spectra. *J. Atmos. Sci.*, **55**, pp. 1965-1976, 1998.

Siegert, A.J.F., and H. Goldstein. Coherent and incoherent scattering from assemblies of scatterers. Appendix B in: *Propagation of short radiowaves*, D.E. Kerr (Ed.), Dover, New York, 1951.

Squires, K.D., and J.K. Eaton. Preferential concentration of particles by turbulence. *Phys. Fluids A*, **3**, no. 5, pp. 1169-1178, 1991.

Tatarski, V.I. *Wave Propagation in a Turbulent Medium.* McGraw-Hill, New York, 285 p., 1961.

Vaillancourt, P.A. Microscopic approach to cloud droplet growth by condensation. Ph.D. dissertation, McGill University, Canada, 174 p., 1998.

Van de Hulst, H.C. *Light Scattering by Small Particles.* Dover, New York, 470 p., 1981.

VanZandt, T.E., J.L. Green, K.S. Gage, and W.L. Clark. Vertical profiles of refractivity turbulence structure constant: comparison of observations by the Sunset radar with a new model. *Radio Sci.*, **13**, pp. 819-829, 1978.

Venema, V.K.C, J.S. Erkelens, H.W.J. Russchenberg, and L.P. Ligthart. Some notes on scattering of radio waves by clouds. *Proc. Symp. Remote Sensing of Cloud Parameters*, 21-22 October, IRCTR, Delft, The Netherlands, ISBN: 90-804551-6-4, pp. 63-70, 1999.

Chapter 6

The contribution of coherent particle scattering to the reflections of radio waves by clouds

Abstract. *Well-known scattering mechanisms in clouds are Rayleigh scattering by individual droplets and clear-air scatter by spatial humidity variations. This chapter discusses the importance of these two mechanisms compared to a third scattering mechanism: coherent particle scattering by spatial variations in the liquid water content of the clouds. We will argue that for radars using a wavelength larger than a centimetre coherent particle scatter can dominate Rayleigh scattering from individual droplets, both for cumulus and stratiform clouds. Furthermore, this work will show that "clear-air" scatter is probably less important in clouds than previously thought. These conclusions are somewhat tentative, as there is an enormous lack of quantitative data on the spatial variations in humidity and liquid water content for the various cloud types. Especially simultaneous measurements of these spatial variations are needed.*

6.1 Introduction

Radars are much used in cloud research for the measurement of macroscopic and microscopic cloud properties, often in combination with other instruments like a lidar, or a radio wave radiometer. For most of these applications the scattering mechanism of the radio waves has to be understood well. Well-known mechanisms are incoherent particle scatter and coherent air scatter.

Incoherent particle scatter comes from particles (e.g. cloud droplets) which are randomly distributed within the radar volume. For small particles it is normally called

Rayleigh scatter, for larger ones Mie scatter. Incoherent particle scatter is most important for atmospheric radars with a small wavelength.

Coherent air scatter is caused by variations in the refractive index of atmospheric gases. This type of scatter is often called Clear-air scatter or Bragg scatter. In this thesis it will be called coherent air scatter. Coherent air scatter is normally dominated by spatial variations in humidity, but also variations in temperature and pressure can play a role, as well as the co-variances between these three variables [Gossard and Strauch, 1980]. Coherent air scatter occurs mainly in radar measurements using a long wavelength (cm-waves or longer).

Chapter 5 showed showed that a third scattering mechanism may be important in clouds: coherent particle scatter by variations in the liquid water content (LWC) of clouds. Just as coherent air scatter, this mechanism is mainly important for atmospheric radars with a long wavelength. Chapter 5 showed that coherent particle scatter (scatter of radio waves by spatial variations in particle mass density) can explain the dual-wavelength radar measurements of cumulus clouds performed by Knight and Miller (1998) and those of a smoke plume by Rogers and Brown (1997). Chapter 5 also showed quantitatively that for an S-band radar, coherent particle scatter can be stronger than incoherent particle scatter in a cumulus cloud. Moreover, it showed that coherent particle scatter can be stronger than coherent (clear-) air scatter at the top of a cumulus cloud.

We argue that together the measurements and theory offer a strong case that coherent particle scatter is significant in S-band radar measurements of cumulus clouds. That is why in this work we will explore the importance of this scattering mechanism for other radar systems and cloud types. As quantitative data is sparse, the discussion must be labelled as tentative, but this is not continuously stressed for readability.

In the second part of this chapter we will indicate for which radar wavelengths, cloud types and atmospheric conditions one can theoretically expect coherent particle scatter to be significant (section 6.6). In this section coherent particle scattering is compared in strength to the other two scattering mechanisms. To make the discussion less theoretical, we will refer to some cloud measurements presented in section 6.5. The first part of the chapter (sections 6.2 through to 6.4) serves as a background for this discussion. In section 6.2, the theory of coherent particle scatter will be presented and extended to allow for different slopes of the variance spectrum of the LWC variations. Section 6.3 will give a small literature survey of what is already known about spatial variations in humidity and LWC from in situ measurements. To be able to extend these sparse measurements to other situations, the sources and sinks of the LWC and humidity variations have to be understood; therefore these are discussed in section 6.4. In the last sections conclusions are drawn and some recommendations for further research are made.

6.2 Theory of coherent particle scatter

When particles in some volume have a completely random distribution in space (the so-called Poisson distribution), the average reflected power is simply the sum of the squared amplitudes from the individually reflected waves:

$$\overline{P}_{inc} = \tfrac{1}{2}\sum_n \alpha_n^2 \tag{6.1}$$

In this case the average incoherent particle return ($\overline{P}_{inc}$) is only determined by the amplitude (α_n) of the reflected waves; the phase (or position of the particle relative to the radar) can be ignored in this case. For some particle configurations the interference will be constructive, but for others destructive. For example, in the case of two particles, the reflected power could be 4 times the power of one particle when they are close together and the power could be almost zero when they are about $\lambda/4$ apart as seen by the radar. On average, however, the interference between the waves reflected by the particles can be ignored. When for simplicity we assume that all the N_V particles reflect with the same amplitude (α), the average returned power is $\frac{1}{2}N_V\alpha^2$. For small particles with number density (N) the average radar reflectivity factor is ND^6 (Rayleigh scatter).

When there are spatial correlations in the measurement volume, the phase cannot be ignored. For example, in the extreme case that all particles are confined to a volume much smaller than the wavelength, all amplitudes add up and the returned power is $\frac{1}{2}N_V^2\alpha^2$, which is much larger than in the incoherent case.

The spatial correlations in clouds can be depicted as lumps of particles and/or voids of particles, with sizes from millimetres to kilometres; they are clearly visible in optically thin clouds, see Fig. 6.1. Because there is structure in clouds (voids and particle lumps), the presence of a particle will enlarge the chance of finding another particle in a volume close by, compared to a remote volume. Such spatial correlations give rise to extra reflections, called coherent particle scatter. Cloud structures with all physical sizes influence the radar backscatter, but mathematically only the Fourier component on a scale of $\lambda/2$ is taken into account. When in the remainder of this chapter variations at a certain scale are mentioned, the Fourier component at this scale is meant.

The radar backscatter for a cloud volume with droplets will be both coherent and incoherent. If we assume a cloud with a mono-disperse drop size distribution with diameter (D) in which the particle mass variations are transported from large scales to small scales by isotropic homogeneous turbulence, the radar backscatter is given by [chapter 5]:

$$Z = ND^6 + 4.2\times10^{-3}\beta^2 L_0^{-2/3} N^2 D^6 \lambda^{11/3} \tag{6.2}$$

Figure 6.1. Clouds have spatial structures on many different scales. The Liquid Water Content variations are clearly visible in this optically thin cloud. These structures can give strong radar reflections.

with N the ensemble average particle number density, L_0 the outer scale length of the inertial subrange of isotropic homogeneous turbulence, and λ the radar wavelength. The first term is the incoherent backscatter and the second term the coherent backscatter; for both Rayleigh scatter is assumed. The standard deviation of the spatial Liquid Water Content (LWC) variations is assumed to be a fraction (β) of the total LWC.

The derivation of Eq. (6.2) consists of two steps. 1) Relate the refractive index variations to the liquid water variations. 2) Relate the radar reflectivity to the spatial variations in the refractive index. The treatment of the derivation will be kept short in this chapter, as chapter 5 already discussed it at length. New in this derivation is that we allow the slope of the LWC variance spectrum to assume various values.

Step 1. In Van de Hulst (1981) the refractive index (n) of air with many small spheres is formulated as:

$$n = 1 + \frac{\pi}{4} K D^3 N \tag{6.3}$$

with $K = (\varepsilon_r-1)(\varepsilon_r+2)^{-1}$, a constant that is determined by the relative permittivity of the particles (ε_r); the absorption is neglected. Equation (6.3) is valid if the second term on the right-hand side is small compared to unity, and when the particles are far apart compared to their size, but close together compared to the wavelength. These assumptions are true for a homogeneous cloud and should also hold for the small spatial LWC variations considered in this thesis. For mm-waves this treatment of the discrete particles as a continuous refractive index is not completely justified.

Assuming that the standard deviation of the variations is a fraction of the mean LWC, i.e. $\sigma_{LWC} = \beta \cdot LWC$, or $\mathrm{var}(ND^3) = \beta^2 (ND^3)^2$, one can write:

$$\mathrm{var}\, n = \frac{\pi^2}{16} |K|^2 \, \mathrm{var}(ND^3) = \frac{\pi^2}{16} |K|^2 \, \beta^2 N^2 D^6 \tag{6.4}$$

This variance in refractive index is only the variance of the continuous refractive index field. The variance due to the discrete nature of the droplets is not taken into account.

Step 2. The radar backscatter is determined by the energy of the three-dimensional power density spectrum ($\phi_n(\boldsymbol{k})$). The backscatter is proportional to the power in a small spectral band around half the radar wavelength in the direction ($\hat{\mathbf{k}}$) of the radar beam. Note that variations at scales larger than $\lambda/2$ can also contribute when they are not parallel to the radar beam, as the projection on the unit vector $\hat{\mathbf{k}}$ is the variable of interest. Following Ottersten (1969) we assume that the spatial variance spectrum integrated over the entire wave number (k) space is equal to the total spatial variance of the refractive index (var n). To compute this three-dimensional power density integral, an assumption has to be made about the shape of the power density spectrum. A common assumption is that the energy spectrum of the LWC variations follows the well-known $-5/3$ law for homogeneous isotropic turbulence in the inertial subrange.

Slopes different from $-5/3$ have been measured in clouds, see section 6.3. That is why an equation for coherent particle scatter for slopes between -1 and -3 will be derived here. According to Tatarski (1961) the three-dimensional spectral density (ϕ(k)) for isotropic turbulence spectrum is given by:

$$\phi(k) = \frac{\Gamma(p+1)}{4\pi^2} \sin\left(\frac{\pi(p-1)}{2}\right) C_n^2 k^{-(p+2)} \tag{6.5}$$

with Γ(..) the gamma function, $-p$ the slope of the (LWC) variance spectrum. The structure constant of the refractive index (C_n^2) is a measure of the total amount of refractive index variations per unit volume. The function is only defined for $1<p<3$. For a slope in k-space with $p<1$, the LWC field in physical space will be stationary, but discontinuous. For slopes with $p>1$, the LWC field will be continuous but non-

stationary. However, the increments $[\xi(x+r)-\xi(x)]$, which are needed to calculate a structure function, are stationary as long as $p<3$ (Davis, 1996).

The relation between the variations in k-space and the physical space is given by:

$$\int_{-\infty}^{\infty} \phi(\mathrm{k}) d\mathrm{k} = \mathrm{var}\, n \tag{6.6}$$

The largest scale and the smallest scale of the inertial subrange are designated by L_0 and ℓ_0, respectively. In the inertial subrange the above integral can be computed by using Eq. (6.5) and by assuming that there are no variations at scales above L_0 or below ℓ_0. C_n^2 is then given by:

$$C_n^2 = \frac{p-1}{2\Gamma(p+1)\sin\left(\pi(p-1)/2\right)} \frac{(2\pi)^p}{\left(L_0^{p-1} - \ell_0^{p-1}\right)^{-1}} \mathrm{var}\, n \tag{6.7}$$

In clouds there will also be variations at scales above L_0. The comparison between measurements and calculations will be most accurate when these variations at large scales are removed from van n, e.g. by choosing some L_0 in the inertial subrange and only using the variance of the scales smaller than L_0. The relation between C_n^2 and the radar reflectivity can be if the expression,

$$\eta = \frac{\pi^2}{2} k^4 \varphi(k) \tag{6.8}$$

from Ottersten (1969) is combined with Eq. (6.5):

$$\eta = \frac{\Gamma(p+1)}{8} \sin(\pi(p-1)/2) k^{-p+2} C_n^2 \tag{6.9}$$

Combining the above with Eq. (6.7) and substituting k by $4\pi\lambda^{-1}$ (the length scale of interest is $\lambda/2 = 2\pi/k$) yields the radar reflectivity as a function of var n:

$$\eta = \frac{(p-1)\pi^2}{2^p} \left(L_0^{p-1} - \ell_0^{p-1}\right)^{-1} \lambda^{p-2}\, \mathrm{var}\, n \tag{6.10}$$

The radar reflectivity factor is defined by:

$$Z = \frac{\lambda^4}{\pi^5 |K|^2} \eta \tag{6.11}$$

Finally, by combining (6.4), (6.10), and (6.11), we find the radar reflectivity factor for coherent particle scatter for a variance spectrum with $1<p<3$:

$$Z = \frac{p-1}{16\pi\ 2^p} (L_0^{p-1} - \ell_0^{p-1})^{-1} \lambda^{p+2} N^2 \beta^2 D^6 \tag{6.12}$$

which will reduce to the second term on the right-hand side of Eq. (6.2) for p=5/3 and $\ell_0 << L_0$. For most slopes the term with the inner scale (ℓ_0) can be ignored, as the outer scale (L_0) is normally much bigger. However for p→1 the inner scale will become increasingly important.

6.2.1 Coherent and incoherent particle scatter

There are two ways to distinguish coherent from incoherent scatter. The first method uses the difference in wavelength dependence of the coherent and incoherent backscatter. The incoherently reflected power from droplets strongly depends on the wavelength, whereas the coherent backscatter from turbulent variations is less wavelength dependent. The radar reflectivity factor corrects for the incoherent wavelength dependence. Therefore the radar reflectivity factor of a coherently scattering volume becomes wavelength dependent, while the radar reflectivity factor of an incoherently scattering volume is the same for two radars with different wavelengths. The incoherent radar reflection is given by:

$$Z = ND^6 \tag{6.13}$$

For a coherently scattering volume the radar reflectivity factor measured by two radars differs by a factor. For a given slope of the variance energy spectrum, this factor depends on the ratio of the two wavelengths,

$$d = \frac{Z_{coh,1}}{Z_{coh,2}} = \left(\frac{\lambda_1}{\lambda_2}\right)^{p+2} \tag{6.14}$$

For example, the difference in radar reflectivity factor between a 10-cm and a 3-cm radar is 19 dB if the slope ($-p$) of the spectrum is $-5/3$. Details can be found in, e.g., appendix A of Knight and Miller (1998). A disadvantage of this dual-wavelength method is that the slope of the energy spectrum has to be known accurately. There are indications that the $-5/3$ law is not always valid, see section 6.6.1 Using for one of the radars a very small wavelength, which will only see incoherent scatter, could circumvent this.

Another method is to look at the angular dependence of forward scatter using a bi-static radar. For radar scatter under an angle, the effective wave number (κ) is given by [Gossard and Strauch, 1980]:

$$\kappa = 2k\sin(\theta/2) \tag{6.15}$$

with k the absolute wave number of the transmitted wave, and θ the angle between the transmitted and scattered wave (θ=0 for forward scatter). Incoherent scatter does not depend on the azimuth for vertically polarised radio waves, whereas coherent scatter will change as given by Eq. (6.15). The advantage of this method is that the

coherent scatter can be determined for a range of wave number values and it becomes possible to estimate the slope of the variance spectrum within this range. However, because scanning is necessary to determine the angular dependence, this method can only be used for homogeneous clouds.

6.2.2 Coherent air and coherent particle scatter

In general it is not possible to distinguish coherent particle scatter from coherent air scatter by measuring with a radar. In some special cases it can be possible to indicate which of these scattering mechanisms dominates the radar return. For example, a correlation between the incoherent particle scatter (the reflections from a short-wavelength radar) and the coherent scatter (long wavelength) is an indication that the coherent scatter is from particles and not from the air, see Chapter 5. Such a correlation has been observed in S- and X-band measurements of cumulus clouds.

However, there does not have to be a correlation between incoherent and coherent particle scatter. First of all, if a correlation is to become noticeable, one variable has to vary much more (the droplet diameter in the case of this cumulus measurement, due to condensational growth) than the other variables in Eq. (6.12).

Secondly, the drop size distribution has to be well behaved: There has to be a stable relation between the smaller and the larger particles of the drop size distribution, as the coherent particle scatter is more sensitive to small drops and incoherent scatter to large drops. This is due to the fact that coherent particle scatter in clouds is proportional to N^2D^6 (or LWC^2) and the incoherent particle scatter to ND^6, and generally there are more small particles. For example, for drizzling clouds the correlation between coherent and incoherent particle scatter is likely to be poor.

For cumulus clouds there is a strong relation between the smaller drops and the larger drops: based on in situ measured (FSSP) drop size spectra Paluch et al. (1995) estimate that using the incoherent particle scatter (sensitive to the larger drops) the LWC (sensitive to the smaller drops) can be estimated with an error of just 13 %. In stratocumulus clouds the relation between LWC and the incoherent particle scatter can be very weak [Fox and Illingworth, 1997; De Wit et al., 1999]. For these clouds the correlation between incoherent and coherent particle scatter is also likely to be poor.

In some cases coherent air scatter can be distinguished from particle scatter (either coherent or incoherent) based on the Doppler velocity, see e.g. Cohn et al. (1995) who are able to distinguish between coherent air scatter and reflections from rain. Other instruments can help to determine the dominant coherent scattering mechanism. An example is using a lidar to ascertain whether particles are present in the first place. Coherent air scatter in clouds will be strongest (or weakest) when the air outside the cloud is relatively dry (or humid). An instrument capable of measuring humidity (radiosonde, microwave radiometer, etc.) can therefore be of help.

6.3 Measured spatial variations

The magnitude of the spatial variations in LWC determines the strength of coherent particle scatter, while the spatial humidity variations determine the coherent air scatter. In their comparison of coherent particle and coherent air scatter Gossard and Strauch (1981) state that within a cloud in steady-state at saturation with no precipitation removing water from the cloud and minimal entrainment it seems reasonable to assume that the variance of humidity is about the same as that of the LWC. This is a logical assumption for the *temporal* variance of an isolated cloud volume as a change in humidity must result in an equal change in LWC. The radar backscatter is determined by the *spatial* variance, however. It is theoretically possible to change the spatial variance of the LWC without affecting the spatial humidity variance. Furthermore, for many (parts of) clouds the assumption of minimal entrainment will not be valid. Therefore, one will have to look for the sources and sinks of spatial variations to estimate the magnitude of humidity and LWC variations (see section 6.4), or directly use the measurements of those variations. That is why in this section some of the literature on in situ measured spatial variations will be reviewed.

In literature a large set of in situ measurements of spatial variations are described, the latest at very small scales. Often just measurements of spatial variations in *number density* are tested for *statistical* significant deviations from the Poisson statistics. However, for coherent scatter *physically* significant spatial variations in *liquid water content* and *humidity* are of interest. Variations in number density are not readily translated into LWC variations. Furthermore, a volume with statistical significant LWC variations may not have physically significant LWC variations, i.e. give little coherent particle scatter.

Davis et al. (1999) measured spatial LWC variations down to scales of 4 cm with a Particulate Volume Monitor (PVM-100A) probe in broken stratocumulus clouds with embedded towering cumulus clouds as a part of the Southern Oceanic Cloud EXperiment (SOCEX). The average LWC in the cloud is 0.290 ± 0.167 g/m^{-3}, so the relative standard deviation is 58 percent. They find a significant change of the slope (a scale break) of the LWC variance spectrum at scales of 2 to 5 m. At longer scales, the slope is close to $-5/3$ (-1.6 ± 0.1), but at smaller scales there are more variations than expected from the $-5/3$ slope as here the slope is -0.94 ± 0.10. These extra variations at small scales correlate with spikes occurring in the LWC time series (voids or blobs at most a few 4-cm pixels wide). Davis et al. attribute the extra spatial variations below 2 to 5 m to these spikes.

In an earlier article with LWC measurements of stratocumulus from the FIRE87 campaign Davis et al. (1996) also find spikes in some parts of the LWC time series. Other parts are relatively smooth. These measurements with a King probe have a resolution of 5 m. The average relative standard deviation was about 19 %, but it varied highly per measurement; the lowest value found was 5 % and the highest

25 %. The average slope of the LWC variance spectra from all flights was -1.36 ± 0.06, significantly flatter than $-5/3$.

One of the first measurements of cm-scale variations was done by Baker (1992). Measurements of cumulus clouds at all heights were performed with a Forward Scattering Spectroscope Probe (FSSP) with a spatial resolution of about 0.32 mm. Baker tested the variance of the number of droplets relative to the mean. This way he found statistically significant spatial correlations in number density on cm-scales in the majority of cloud penetrations. However, statistically significant variations on all measured scales were only observed in small parts (often near edges) of many clouds and throughout a few clouds.

Malinowski et al. (1994) observed that entrained air contained filaments of cloudy air with droplet concentrations close to those observed in the clouds. Furthermore, they suggest that the distribution of these filaments is anisotropic.

Jameson et al. (1998) performed measurements using the Particle Measurement System (PMS): two-dimensional optical array probes with a resolution of 130 m in a tropical warm precipitating cumulus about 1 km above the cloud base. The main conclusion of these authors is that spatial variations in drop counts are statistically significant from 130 m up to 2 km scales (variance is much larger than the mean). Besides that they also found variations down to 5 cm scales, using the distribution of the interdrop distance.

Korolev and Mazin (1993) have carried out extensive measurements with an FSSP-100 of stratiform clouds (stratus, stratocumulus, altostratus, altocumulus, and nimbostratus). In total 50 cloud with a total length of 1710 km were measured layers on 20 different days. On the basis of this data set they conclude that cloud holes occur most frequently in the vicinity of the upper and lower boundaries of the cloud, but also in parts removed from the upper and lower boundary by hundreds of meters. About 80 percent of these holes was of the smallest size (up to 10 m). On average the holes (defined as volumes with less than 50 percent of the average number density) occupied about 7 percent of the cloud volume. However, this number varies highly: in some clouds it was 20 percent and sometimes no holes were found for dozens of kilometres. Also regions with an increased droplet number concentration were found. However, these were mainly due to the appearance of a large number of small droplets, so these may not be that important for the spatial variations in LWC.

Kozikowska et al. (1984) made a hologram of 22.5 cm^{-3} in fog to measure the three-dimensional droplet distribution on the smallest scales. The distribution of the number density in this one sample is significantly not a Poisson distribution.

Humidity variations have been measured by Politovich and Cooper (1988). They estimate the supersaturation in cumulus clouds with a resolution of 10 m by measuring the vertical velocity (Rosemount 858 gust probe) and the drop size distribution

(FSSP). The supersaturation was estimated to be in the range of −0.5 to 0.5 % for all cloud regions during 147 cloud penetrations of 13 clouds on 8 days. In the entrained regions the standard deviation was below 0.4 % and in the core of the cloud around 0.1 %.

Concluding, measurements of cumulus, stratus clouds and fog with a variety of instruments indicate that non-Poisson distributed droplets occur regularly. However, Poisson distributions are found as well. Especially the presence of spatial variation in the adiabatic cores of cumulus clouds is still under debate, see Grabowski and Vaillancourt (1999) and references therein. The structure of the variations is described as spikes [Davis, 1996] and anisotropic filaments [Malinowski et al., 1994]; the theory of coherent particle scatter may have to be modified to account for such strong variations.

Unfortunately quantitative measurements of spatial LWC variations could only be found for stratocumulus (with embedded cumulus), whereas for some cloud types no measurements of spatial variations could be found at all. Only one indirect measurement of spatial humidity variations was found in literature. No simultaneous measurement of humidity and LWC variations was found in literature. The strength of the coherent backscatter can only be estimated using the available quantitative measurements, which is done in section 6.6.

6.4 Sources and sinks of spatial variations

To be able to extrapolate the sparse measurement data to other cloud types and atmospheric conditions, one needs to know the sources and sinks of these variations. We identify a number of possible sources for spatial variations of LWC.

At the base of the cloud, differences in the condensation level of the air parcels can create variations due to differences in the temperature and humidity of the initial air parcels. Korolev and Mazin (1993) estimate that the variations in the condensation level which are caused by this lie in the order of tens of meters. This fits with their observation that a relatively higher number of cloud holes occur in the lowest 100 m of stratiform clouds compared to the middle of the cloud.

Spatial variations can also be caused by vertical movements in a sub-adiabatic cloud. For a typical stratiform cloud, Korolev and Mazin estimate that a descending movement of 60 m can create a cloud hole.

Spatial LWC variations may also be created by the inertia of the droplets in a turbulent field, often called preferential concentration of droplets, see e.g. Squires and Eaton (1991), Shaw et al. (1998), Vaillancourt (1998) and Pinsky et al. (1999). In a vortex particles are propelled outward by the centrifugal force, so after some time the vortex is particle-free; the particles have moved to quiet areas with low vorticity.

(For an introduction to vortices in turbulence see e.g. the textbook by Frisch (1998) in section 8.9). It is still under discussion whether the right conditions are present in (cumulus) clouds, as realistic modeling of turbulence in clouds is still too difficult. Important unknown factors are the lifetime of the vortices, their volume fraction and the influence of sedimentation due to gravity. Preferential concentration could be an important mechanism as it can also act in the adiabatic cores of clouds.

Entrainment of dry and droplet-free air from outside the cloud is especially important at the cloud top, amongst others due to loss of stability of air parcels by radiative cooling. Entrainment or mixing can also be important at the sides of cumulus clouds. The spatial humidity variations caused by mixing give rise to mantle echoes at the cloud edges on dry days. These mantles can be up to 1 km thick at S-band, see, e.g., Knight and Miller (1998).

When making statements about (the absence of) mixing, one has to remember that an adiabatically ascending air parcel is an idealisation. A parcel always has some heat exchange; whether this is a significant deviation from adiabaticity will depend on the research question. For example, the S-band reflectivity in one of the examples in the paper of Knight and Miller (their Fig. 6) shows a 500 m thick mantle echo caused by coherent air scatter (humidity variations). This coherent air scatter is thought to be caused by *mixing* with environmental air. The X-band reflectivity shows flat echo bases at already a few tens of meters from the cloud edge, however, and these echo bases are interpreted by Knight and Miller as *unmixed* ascent of the cloud air parcel. These two statements do not contradict each other since the amount of mixing to create coherent scatter is probably less than the mixing needed to get a significant decrease in average LWC.

Sinks for LWC variations at large scales are turbulence (which transfers the variations to smaller scales) and a sink for LWC variation at small scales is sedimentation.

Concluding, all the above mechanisms – entrainment, parcel differences at cloud base, vertical movements in sub-adiabatic clouds, and preferential concentration – depend on the strength of the turbulence. The first three effects become stronger in a more turbulent situation. For preferential concentration the relation with the turbulence strength may be more complex. As mixing with environmental air is an important mechanism at cloud edges and the gradients are high at the top and sides of the clouds, the spatial variations are expected to be largest at these cloud edges. For stratiform clouds this is confirmed by Korolev and Mazin (1993), who state that cloud holes are found more often at cloud tops. For cumulus clouds this is confirmed by the mantle echoes.

Less is known about the sources and sinks of humidity variations in clouds. Sources should be entrainment, the finite relaxation time of evaporation and condensation after the temperature of the parcel has changed due to turbulence or an updraft or

downdraft. Sinks should be turbulence, diffusion and evaporation and condensation. Thus also humidity variations are expected to be largest at the cloud boundaries. Evaporation and condensation are expected to be important sinks of humidity variations in clouds.

In theory it could be possible that a cloud has a lower radar reflectivity than its surroundings when the reflectivity from the surroundings comes from humidity variations. In the case of small fair-weather clouds in the convective boundary layer one may be able to measure such a effect with a windprofiler (for coherent scatter) and a lidar ceilometer (for cloud detection). If this effect were to occur, this would provide evidence that evaporation and condensation are important sinks for humidity variations. Care has to be taken as big clouds will also decrease the coherent air scatter in the boundary layer by reducing the solar flux, however.

6.5 Radar measurements

This section presents some radar cloud measurements in which coherent particle scatter may play a role. They will be used in section 6.6 for a quantitative discussion. There are also strong indications of coherent particle scatter in a dual-wavelength measurement of a smoke plume, see chapter 5.

In a recent article, Knight and Miller (1998) discuss a large number of measurements of developing cumulus clouds, performed with 2 radars: an X-band radar and an S-band radar with wavelengths of 3 and 10 cm, respectively. Most measurements could be explained by using the traditional theory. However, on humid days, the patterns for both radars looked similar, resulting in a correlation between the S- and the X-band reflectivity factors. This correlation is puzzling in cases where the difference in reflectivity factors is not equal to 0 dBZ (for purely incoherent scattering) or 19 dBZ (for purely coherent scattering). In some measurements the X- and S-band reflectivity factors lie on a line with a slope of one, with a typical difference of about 10 dBZ; other offsets have been measured as well. The phenomenon is mostly confined to the core of the reflectivity pattern and its nearby surroundings and to the region near the cloud base.

A similar correlation in a cumulus cloud was measured by Baker et al. (1998), who already speculated that the droplets may scatter coherently. A quantitative explanation for these correlations in cumulus clouds in terms of coherent particle scatter can be found in chapter 5. Knight and Miller also observed cases in which the difference between the reflectivity factors was more than 19 dB (up to 22 dB) in the mantle echo. This indicates that the slope of the humidity spectrum is steeper than $-5/3$. For instance, in the case the difference is 22 dB, the slope is -2.2. Knight and Miller give another possible explanation for the large difference in reflectivity factors: the

spatial variations measured by the X-band may not be in the inertial subrange, but in the dissipation range (below ℓ_0)

By measuring the forward and the backward scattering with two X-band radars Gossard and Strauch (1980) were able to separate coherent from incoherent scatter and to measure the coherent scatter as a function of wave number, see also section 6.2.1. During clear-air situations they found a slope of the energy spectrum of −1.7, near −5/3. However, in a cloudy situation in winter the slope was less steep: −0.9. Unfortunately there is no information on the type of clouds measured and other atmospheric conditions (e.g. humidity outside the clouds). For this measurement the nature of the coherent scatter is unknown.

Gage et al. (1999) have performed 3 weeks of measurements with two windprofilers (wavelengths: 11 and 33 cm) of clouds during the Maritime Continental Thunderstorm EXperiment (MCTEX). For these wavelengths the difference in radar reflectivity factor is 18 dB for coherent scatter from a variance spectrum with a slope of −5/3. In the coherent scatter from clouds at 2 km height, they found that the difference is seldom 18 dB. Most differences are 15 to 16 dB. If this were caused by a flatter slope of the variance spectrum, the slope would be between −1.1 and −1.3. For this measurement it is not clear whether the coherent cloud reflection would come from humidity or LWC variations. Gage et al (1999) speculate that another cause of the 15 dB difference in reflectivity may be a difference in the beam widths of the windprofilers.

During the same campaign an ice cloud was measured with the windprofilers, as reported by Gage et al. (1999) and Ecklund et al. (1999). This ice cloud was observed at a height range of 6 to 18 km. The difference in radar reflectivity factor is zero; only Rayleigh scatter is present in this cloud.

A measurement during the Dutch CLARA (CLouds And Radiation) campaigns [Van Lammeren et al., 1999] of a stratocumulus cloud is shown in Fig. 6.2a. The radar reflectivity factor is measured by the 9-cm wavelength Delft Atmospheric Research Radar (DARR). A histogram of the maximum values of the reflectivity profiles is shown in Fig. 6.2b. Values above −20 dBZ are not uncommon, whereas in situ drop size distributions measured with an FSSP-100 never produce values above −25 dBZ for incoherent droplet scatter. The number density is in the order of 500 cm^{-3} and the diameter at the height of the radar reflections in the order of 10 μm. The large difference between the incoherent scatter calculated from the FSSP measurements and the measured radar reflectivity suggests that the scatter is enhanced by coherent scattering by humidity or droplets.

One can not draw a definite conclusion though, as a few large particles can enhance the radar reflectivity a lot [Fox and Illingworth, 1997; De Wit et al., 1999], whereas the FSSP may miss these particles due to the small sampling volume and the small maximum drop size. The aeroplane also did not fly at the height where the maximum reflectivity values occur at the time the highest values occurred. Still the

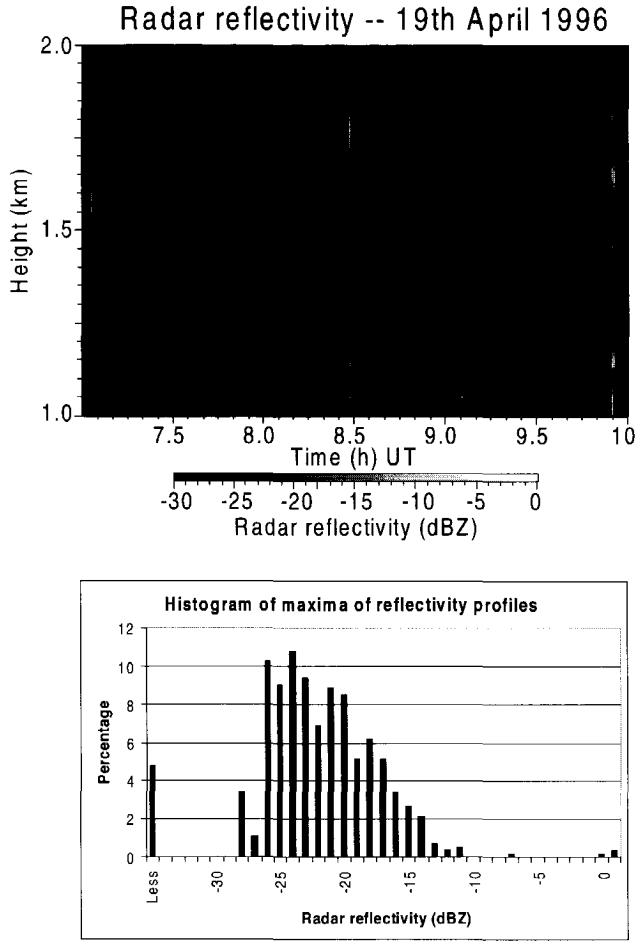

Figure 6.2. Measurement of stratocumulus cloud (6.2a) made on the 19th of April 1996 with the Delft Atmospheric Research Radar (DARR), a 9-cm FM-CW radar. The histogram (6.2b) shows the maximum values of the vertical radar reflectivity profiles between 8 and 9:30 hrs UT of the stratocumulus cloud shown in Fig. 6.2a. The perfectly straight vertical and horizontal lines should be ignored; they are not cloud related.

difference in the radar reflectivity values is intriguing, especially as coherent particle scatter at S-band in stratocumulus is theoretically likely to dominate incoherent scatter, see section 6.6.3.

6.6 Discussion of the measurements

In this section the strength of coherent particle scatter, coherent air scatter and incoherent particle scatter will be calculated for various values of the variables involved. As the slope of the variance spectrum is a complex variable, it will first be discussed in section 6.6.1. The radar measurements from the previous section will be discussed as special cases. The in situ measurements of section 6.3 are used as a reference for the characteristics of the spatial variations.

6.6.1 Slope of variance spectrum

Assuming fully developed isotropic turbulence, one gets a slope of $-5/3$ in the inertial subrange if the sources of the variations act on scales larger than the outer scale (L_0) and the sinks act on scales smaller than the inner scale (ℓ_0). For a passive *conservative* additive the slope of the variance spectrum of the additive is the same as the slope of the turbulent energy spectrum [Tatarski, 1961]. However, both the amount of water vapour and liquid water are not conservative in clouds. One can expect the slope of the humidity or LWC variance spectrum to become more flat (steep) if there is an additional source (sink) of variations within the inertial subrange. The various slopes that have been measured in situ (see section 6.3) or by radar (see section 6.5) are summarised in Table 6.1.

There is some evidence for a steeper slope for humidity variations and a flatter slope for LWC variations; both have been measured and there are mechanisms that may explain it. However, the amount of data is much too sparse for general conclusions, especially for extrapolations to different cloud types and atmospheric conditions.

The deviations in slope from $-5/3$ are important for the strength of coherent particle scatter compared to the other scattering mechanisms, as will be shown in

Cloud type	Slope		Measurement method	Source
Stratocumulus	-0.94 ± 0.10	LWC	In situ, at scales below 5 m	Davis et al. (1999)
Stratocumulus	-1.6 ± 0.1	LWC	In situ, at scales above 5 m	Davis et al. (1999)
Stratocumulus	-1.36 ± 0.06	LWC	In situ	Davis et al. (1996)
Cumulus	-2.2	Humidity	Dual-wavelength radar	Knight and Miller (1998)
Winter clouds	-0.9	Unknown	Forward scattering radar	Gossard and Strauch (1981)
Low level clouds	-1.1 to -1.3	Unknown	Dual-wavelength radar at 2 km	Gage et al. (1999)

Table 6.1. Slopes of the variance spectra in clouds.

section 6.6.2 for the coherent air scatter and in section 6.6.3 for incoherent scatter. For understanding the coherent scatter measurements with radar, the slope of the variance spectra must be measured – preferably simultaneous in situ humidity and LWC measurements – and the underlying mechanisms that influence the slope must be well understood.

6.6.2 Coherent particle scatter and coherent air scatter

Gossard and Strauch (1983) calculated that if the spatial variance of the water vapour content is equal to the spatial variance of the liquid water content, the radar reflectivity due to the humidity variations should be about 28 times larger. The quantitative relations are:

$$\begin{aligned} 10^{12} \cdot \mathrm{var}\, n_L &= 2.09 \cdot \mathrm{var}\, L \\ 10^{12} \cdot \mathrm{var}\, n_V &= 58.5 \cdot \mathrm{var}\, V \end{aligned} \qquad (6.16)$$

with, respectively, var n_L and var n_V as the variance of the refractive index due to Liquid water variations (var L) and water Vapour variations (var V). In other words, if the coherent particle scatter is to dominate the coherent air scatter, the standard deviation of the spatial LWC variations should be at least 5.3 times as large as the standard deviation of the spatial humidity variation. For the above statements about the radar backscatter the slopes of both variance spectra are assumed to be equal.

Using the measurement of spatial humidity variations by Politovich and Cooper (1988) we will show that coherent particle scatter can dominate coherent air scatter for cumulus clouds. The regions giving a high correlation between the S- and the X-band in the article by Knight and Miller (1998) are about 2 km above cloud base. An *adiabatic* cloud with a temperature of 25 degrees Celsius and a pressure of 930 mb at cloud base will have a water vapour content of about 17 g m^{-3} and a liquid water content of about 6 g m^{-3} at 2 km above cloud base. These cloud-base temperatures were observed by Paluch et al. (1996), who measured them during the CaPE-1991; the Knight and Miller radar measurements are from the same campaign. As in the region with the correlations in radar reflectivity the absolute amount of liquid water and water vapour are about equal, one can simply compare the relative variations.

The relative standard deviations in the spatial humidity variations measured by Politovich and Cooper (1988) are: 0.4 % in 80 percent entrained air and 0.1 % in the core of cumulus clouds. If the coherent particle scatter is to dominate coherent air scatter, the standard deviations of the spatial LWC variations should be 5.3 times bigger, so above 6 % for the entrained region and above 1.5 % in the core of cumulus clouds. These values are low compared to the measured LWC variations (5 to 58 % in stratocumulus) and compared to the LWC variations that are needed if co-

herent scatter is to be stronger than incoherent scatter at S-band. Furthermore, to explain the dual-wavelength radar measurements of Knight and Miller (1998), we needed about 25 % LWC variations [chapter 5]. Lower in the cloud the ratio of water vapour content and liquid water content will be higher, so coherent *air* scatter will probably be more important near the cloud base. Therefore it is likely that the scatter by the waterdroplets (either coherent of incoherent) should dominate coherent air scatter throughout cumulus clouds except close to the cloud base. The assumption made then is that the relative LWC variations in cumulus and stratocumulus are in the same order of magnitude.

In stratocumulus the LWC is generally much lower than near the top of large cumulus clouds. When the standard deviation in LWC is 0.167 g/m^{-3} as in Davis (1999), the standard deviation in humidity should be 0.03 g/m^{-3} to get the same amount of scattering from both mechanisms. This corresponds to a humidity of 7.5 g/m^{-3} (dew-point temperature: T_d = 6 °C) with 0.4 % standard deviation or to a humidity of 30 g/m^{-3} (T_d = 30 °C) with 0.1 % standard deviation. As these humidity values are of a natural order of magnitude, and no in situ humidity variation measurements are available in stratiform clouds, a conclusion about these clouds cannot yet be drawn. Simultaneous measurements of humidity and LWC variations are needed.

In the above calculations the slope of the LWC and humidity variations are assumed to be equal. When this is not the case, the results can be drastically different. Assuming that $\ell_0 << L_0$ one can derive using Eq. (6.10) that:

$$\frac{\eta_L}{\eta_V} = \frac{p_L - 1}{p_V - 1} 2^{-p_L + p_V} L_0^{-p_L + p_V} \lambda^{p_L - p_V} \frac{\text{var}\, n_L}{\text{var}\, n_V} \tag{6.17}$$

with η_L and η_V the radar reflectivity due to LWC variations and humidity variations, respectively, and $-p_L$ and $-p_V$ the slopes of the LWC and humidity variance spectra, respectively. Using Eq. (6.16) this becomes:

$$\frac{\eta_L}{\eta_V} = \frac{p_L - 1}{p_V - 1} 2^{-p_L + p_V} L_0^{-p_L + p_V} \lambda^{p_L - p_V} \frac{\text{var}\, L}{28\, \text{var}\, V} \tag{6.18}$$

In Fig. 6.3 η_L and η_V are compared for various slopes and wavelengths for identical variance of humidity and LWC and L_0 = 10 m. For a larger value of L_0 the differences will be larger. In Fig. 6.3 one can see that for equal slopes the coherent air scatter (drawn lines) is 15 dB larger than the coherent particle scatter (dashed lines), as expressed by Eq. (6.16). When the slope of the humidity variations is steeper than the one of the LWC variation the lines can cross and the LWC variation can reflect more power than the humidity variations.

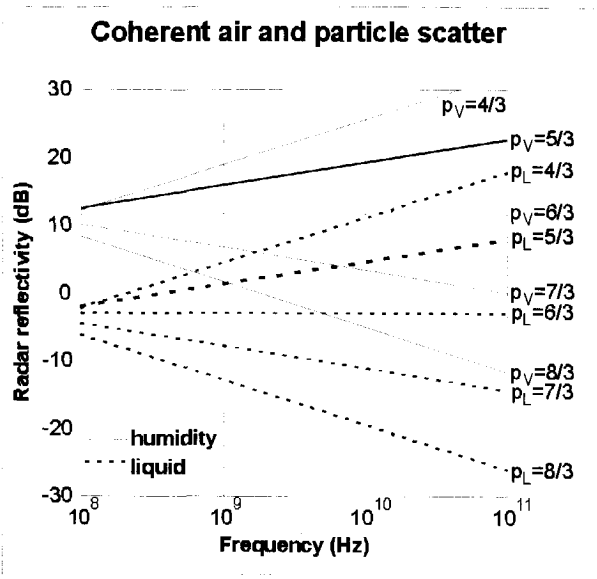

Figure 6.3. Calculation of the strength of coherent air and coherent particle scatter for different slopes of the humidity and LWC variance spectrum using Eq. (6.10) and (6.16). The dashed line is the radar reflectivity from LWC variations and the drawn line from the humidity variations. The variances in humidity and LWC are equal, and L_0 is 10 m.

As an example one can calculate (or read from Fig. 6.3) the radar reflectivity for equal variations in LWC and humidity (var L = var V), and a slope of the humidity variations ($-p_V$) of −2.2 and a slope of the LWC variations ($-p_l$) of −1.36 (see section 6.6.1 for the values of the slopes). For an S-band radar (λ=0.1 m) and L_0=10 m, the radar reflectivity due to LWC variations will now be almost equal to the radar reflectivity due to humidity variations, instead of 28 times smaller. These are preliminary calculations as the value of the outer scale (L_0) is important, but not well known, and the data on the slopes is insufficient. However, the calculations do show that the slope of the spectra can be a factor that may not be ignored when comparing coherent air and coherent particle scatter.

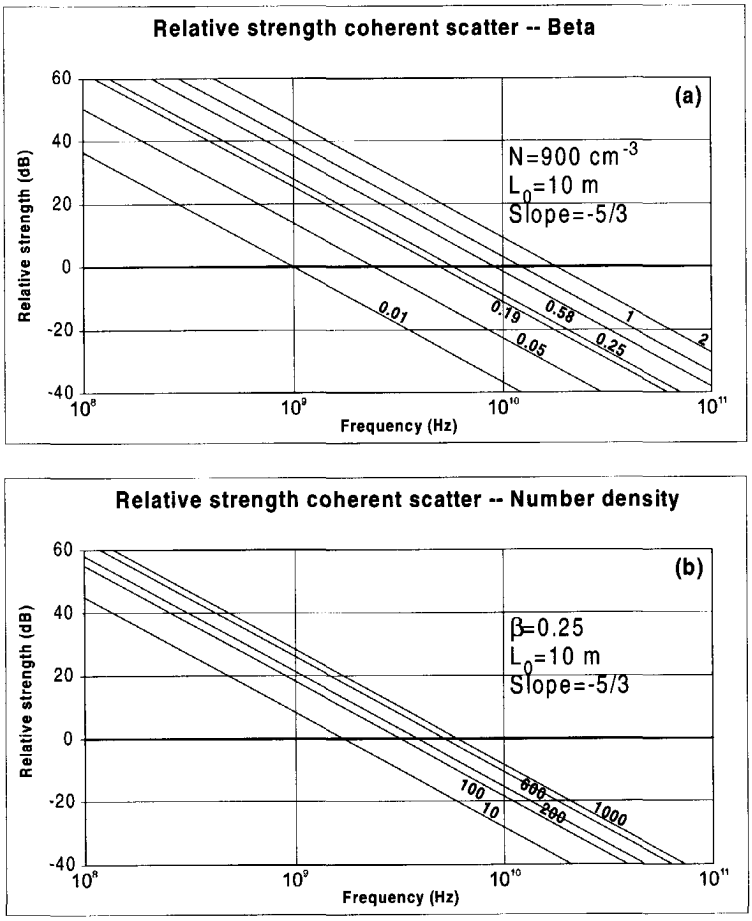

Figure 6.4a-b. Plots of the relative strength of coherent particle scatter compared to incoherent particle scatter as a function of radar frequency as calculated by Eq. (6.12). Fig. 6.4a shows the influence of the relative standard deviation of the LWC. Fig. 6.4b shows the influence of particle number density. See next page for Figures 6.4c and 6.4d.

6.6.3 Coherent and incoherent particle scatter

To see how important incoherent scatter is compared to coherent particle scatter, one has to compare the two terms in Eq. (6.2). Chapter 5, using values from literature, already showed that coherent particle scatter can dominate incoherent particle scatter for the cumulus cloud measurement by Knight and Miller (1998). Knight and Miller measured 10 dB more (coherent) backscatter at S-band than at X-band. To

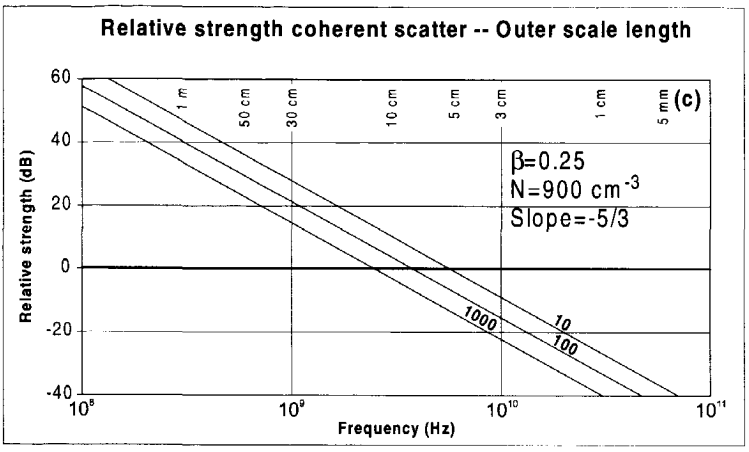

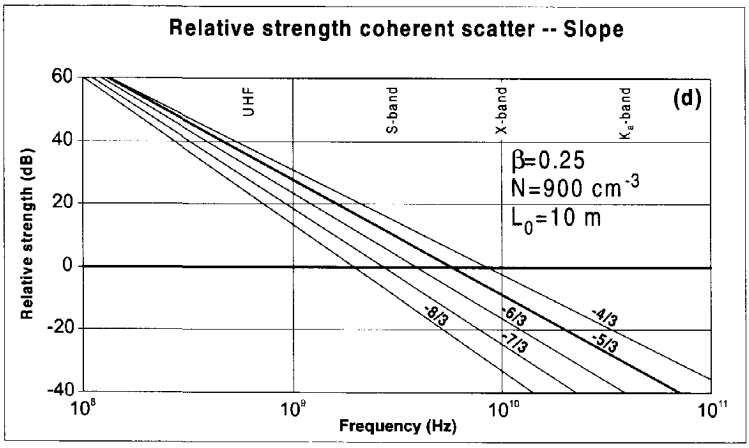

Figure 6.4c-d. Plots of the relative strength of coherent particle scatter compared to incoherent particle scatter as a function of radar frequency as calculated by Eq. (6.12). Figure 6.4c shows the relation for some values of the outer scale of the inertial subrange L_0. The slope dependence is shown in Fig. 6.4d. Figure 6.4a and 6.4b are on previous page.

explain this with coherent particle scatter chapter assumed the values: $L_0 = 10$ m (from VanZandt et al. (1978)), ℓ_0=0, $N = 800 \cdot 10^6$ m^{-3} (from Paluch et al. (1996)), $\lambda = 0.1$ m, and a slope of -5/3, to arrive at a relative spatial standard deviation of $\beta = 0.25$. With a flatter slope (p=1.36) and the other variables the same, β would have to be 0.14.

To explain the S-band radar reflectivity factor values of a stratocumulus cloud (Fig. 6.2) by coherent particle scatter one can use the number density

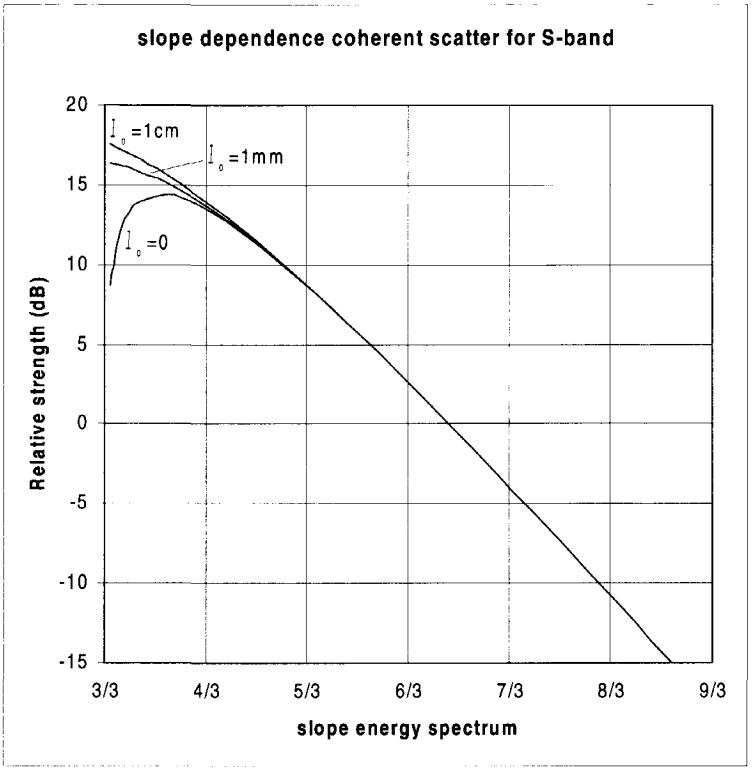

Figure 6.5. The relative strength of coherent particle scatter compared to incoherent particle scatter as a function of the slope of the variance spectrum for an S-band radar, using Eq. (6.12). The figure shows that for small slopes the inner scale of the inertial subrange becomes important. The relation is plotted for three inner scales: 0, 1 mm and 1 cm. Other variables used are L_0=10 m, β=0.25, N=900 cm^{-3}, λ=9 cm, and p=5/3.

(N=500·10^6 m^{-3}) and diameter (D=10 μm) from the FSSP measurements. Then, using the values L_0 = 10 m, ℓ_0=0, λ = 0.09 m, and p=5/3, one will get -20 dBZ scatter with β = 0.55 and -10 dBZ with β = 1.75. With a flatter slope (p=1.36) and the other variables the same, β would have to be 0.33 to get -20 dBZ and 1.03 to get -10 dBZ.

Unfortunately, it is not possible to calculate the backscatter for a slope with p=0.9, but β should be smaller in that case. The relative spatial standard deviations (β) calculated above are high, but may not be unreasonable for a thin cloud, which can be highly entrained.

To investigate this relation for other situations we illustrate the influence of the variables in Eq. (6.2) in a few graphs. Fig. 6.4a shows the relative strength of coherent particle scatter compared to incoherent particle scatter for different values of the relative standard deviation of spatial LWC (β). The other values are for a cumulus cloud case: $L_0 = 10$ m, $N = 900 \cdot 10^6$ m^{-3}. The values for β are taken from the previous discussion, including some more extreme examples. The high values may occur at cloud boundaries and the low ones in a quiet cloud.

In Fig. 6.4b the relative strength of coherent particle scatter compared to incoherent particle scatter is investigated in relation to the number density (N), where the other values are: $L_0 = 10$ m, $\beta = 0.25$. Measured number densities from literature are summarised in Table 6.2; there is a considerable spread in the naturally occurring number densities. A number density of 1000 cm^{-3} is a high value for cumulus, 200 to 500 cm^{-3} is representative for continental stratus clouds, the value of 10 cm^{-3} corresponds to some ice clouds.

That the outer length scale is relatively less important can be seen in Fig. 6.4c. The other values are taken to be: $N = 900 \cdot 10^6$ m^{-3}, $\beta = 0.25$. The value for the outer scale is uncertain. VanZandt et al. (1978) used 10 m and Crane (1980) estimated it to be 10-100 m in the free atmosphere. L_0 is largest in turbulent regions with low hydrostatic stability [Gage, 1999]. We included this graph with L_0 as independent variable to show that the spread is not very large compared to the other variables.

The relative strength of coherent particle scatter compared to incoherent particle scatter is plotted in Fig. 6.4d as a function of the slope (p) using Eq. (6.12). The

Cloud type	N (cm^{-3})	Comment	Source
water clouds			
Cumulus	800-900	Near cloud base.	Paluch et al. (1996)
Continental Cumulus	500-800	30 minutes of data in Montana.	Politovich and Cooper (1998)
Continental stratocumulus	200-500	One measurement.	Korolev and Mazin (1992)
Continental stratus	347	About 1.5 hrs of data.	Sassen et al. (1999)
Coastal stratus	75-150	One measurement.	Korolev and Mazin (1992)
Fog	50	One volume of 22.5 cm-3.	Kozikowska et al. (1984)
Fog	1 to few hundred		Pruppacher and Klett (1997)
ice clouds			
Altostratus	Up to 10		Pruppacher and Klett (1997)
Alto stratus Alto cumulus	75	One measurement.	Korolev and Mazin (1992)
Cirrus	0.05 to 0.5		Pruppacher and Klett (1997)
Cirrus	Up to 0.2	Model, highest N at top.	Sassen and Khvorostyanov (1998
Ice fog	100-200		Pruppacher and Klett (1997)

Table 6.2. Number densities found in clouds.

other values are taken to be: $\beta = 0.25$, $L_0 = 10$ m, $\ell_0 = 0$, $N = 900 \cdot 10^6$ m^{-3}. The influence of the slope will become stronger when a larger outer scale is chosen. Unfortunately, it is not possible to draw a line in the figure for the slope of −0.9 found by Davis et al. (1999), as Eq. (6.12) is only valid for $1<p<3$. Furthermore, for slopes between 1 and 1.3 the inner scale of the inertial subrange becomes important, and may no longer be neglected. This can be seen in Fig. 6.5, where the relative strength of coherent to incoherent particle scatter at S-band is plotted as a function of the slopes between 1 and 3. For slopes close to 1 a large part of the variance is distributed at very small scales when the inner scale is put to zero, thus reducing the variance at cm-scales.

Concluding, for an X-band radar, coherent particle scatter can dominate only for the highest values of β and number densities. For mm-wave radars coherent particle scatter is not likely, although given the uncertainty in the variables (especially β and p) it cannot be ruled out. For windprofilers coherent particle scatter will normally dominate incoherent particle scatter. For typical number densities and relative LWC variations in stratocumulus clouds, coherent particle scatter can dominate incoherent scatter for an S-band radar. Given the typical number densities in ice clouds one may need a windprofiler to have coherent scatter dominating. However, recently Baker et al. (2000) presented measurements of very strong spatial structures in ice clouds. They were only seen for the small particles. If there would be no large particles present, these spatial structures seen in the small crystals would highly likely produce coherent scattering as the spatial standard deviation was a few times the mean IWC. When the slope is flatter than −5/3, which may occur as indicated by measurements, this will make coherent particle scatter several dBs stronger at the radar wavelengths. Given the poor present state of knowledge the above conclusion may have to be modified in the future.

6.7 Summary and conclusions

This chapter explored the possibility of significant coherent particle scatter in clouds. Measurements in literature have shown significant spatial variations in liquid water content and humidity in stratus, stratocumulus and cumulus clouds. Unfortunately, quantitative measurements of spatial LWC variations and the slope of the variance spectrum are only available for stratocumulus (with embedded cumulus). Quantitative spatial humidity measurements exist only for cumulus clouds.

Dual-wavelength radar measurements of cumulus clouds show signs of coherent particle scatter at S-band. Radar measurements with a 9-cm wavelength of stratocumulus show some indications of coherent scattering. Furthermore, there is evidence from dual-wavelength measurements that the slope of the humidity spectrum can be

steeper and from in situ measurements that the LWC spectrum can be flatter than the standard value of $-5/3$, which can be very important for the radar reflectivity.

Theoretical calculations show that coherent particle scatter can dominate coherent air scatter in the top part of cumulus clouds. In stratiform clouds one cannot say whether coherent particle scatter or coherent air scatter is strongest given the large margin of error; simultaneous measurements of humidity and LWC variations will have to be made to determine which mechanisms will dominate. If possible deviations from the $-5/3$ slope of the variance spectra of humidity and LWC are taken into account, it is possible that coherent particle scatter is stronger than coherent air scatter when the total variance of the humidity and LWC are equal. This contradicts previous calculations with equal slopes, which indicated that coherent particle scatter should be insignificant for equal variations in humidity and LWC.

Incoherent particle scatter should theoretically dominate coherent particle scatter for a mm-wave radar. Which kind of scatter dominates for a cm-wave radar will depend on the cloud type and atmospheric conditions. For a dm-wave radar coherent particle scatter will almost always be more important than incoherent scatter. For an S-band radar coherent particle scatter of stratocumulus clouds can be significant compared to incoherent scatter. However, there is no reliable estimate of the relative strength of coherent air scatter for these types of clouds. When the slope is flatter than $-5/3$, as is indicated by measurements, coherent particle scatter will be several dBs stronger at wavelengths below 1 m.

6.8 Recommendations and outlook

Since until now not much attention was given to coherent particle scatter, still many questions remain. To test the theory of coherent particle scatter, simultaneous measurements of LWC and humidity variations should be compared to radar measurements of coherent scatter. Experiments on cumulus clouds similar to those of Knight and Miller but with a mm-wave radar as smallest wavelength or a bi-static forward scattering radar setup could confirm the theory if similar results are produced.

To develop the theory further, small-scale in situ measurements should be made of humidity, LWC and temperature spectra, both of the total variance and the slopes. These measurements should preferably be done in the same volume, so that the covariances at small scales can be determined as well. Measurements of the LWC and humidity spectra should be made for a range of different cloud types to determine which type of coherent scatter is important for which type of cloud. These spectra

should be measured at scales close to the radar wavelength, to reduce problems with the slope of the variance spectra. A theoretical expression for coherent particle scatter for LWC spectra with a slope flatter than −1 should be developed, since −0.9 has been observed.

If coherent particle scatter is often significant in clouds, this may open fascinating new areas for atmospheric radar research. Below some possibilities are given.

It may be possible to develop a method that uses the coherent particle scatter to measure the LWC of clouds. Such a method would have less problems with big drops in the cloud than methods using incoherent scatter. This method will only work if the big drops are not fully dominating the total reflection so much that the coherent term is too difficult to measure. Furthermore, one should be sure that coherent air scatter can be ignored for the cloud studied. The amount of spatial variations is unknown, thus the coherent scatter cannot be used directly. However, a method analogous to the method of Frisch et al (1995) may be applicable: to use a radiometer to restrain the total amount of liquid water in the column (LWP). An assumption about the shape of the relative variation (β) profile in the cloud would then be needed. For a thin cloud it may be allowed to assume β is constant with height.

In a similar way, the difference in the sensitivity of coherent and incoherent particle scatter to particle size may be usable for cloud boundary measurements during rain. Venema et al. (1999) showed with radar and lidar measurements that the radar reflectivity of clouds is insignificant compared to the radar reflectivity of even very light precipitation, which makes cloud boundary measurements using the *total* radar reflectivity impossible during rain. However by carrying out high-Doppler resolution measurements with two wavelengths it may be possible to distinguish between reflections of rain and cloud in a certain velocity and height cell. The cloud particles have a smaller velocity and may scatter a bit stronger (in dBZ) for the longest wavelength compared to the shortest. The precipitation will scatter equally in the Rayleigh domain and fall faster than the cloud droplets. Using only velocity information one can get difficulties with up- and downdrafts.

A radar with a long wavelength may detect some clouds more easily than a radar with a short wavelength of similar sensitivity expressed in radar reflectivity factor.

Radar measurements might contribute to the research on LWC and humidity variations, which are important for understanding the broadening of the drop size distribution during the development of cumulus clouds and consequently for warm-rain formation. The LWC can be determined by a radar in combination with other remote sensing instruments [Erkelens et al., 1999a; Boers et al., 1999; Frisch et al., 1995]. Given the LWC, the measured coherent particle reflection can then be used to estimate the magnitude of the spatial variations at scales close to half the radar wavelength.

References

Baker, B.A., P. Lawson, and C.G. Schmitt. Clumpy Cirrus. *Proc. 13th Int. Conf. on Clouds and Precipitation.* Reno, Nevada, USA, pp. 637-640, 14-18 August, 2000.

Baker, B., J. Brenguier, and W. Cooper. Unknown Source of Reflectivity from Small Cumulus Clouds. *Cloud Physics Conf.*, Everett, Washington, 1998.

Baker, B.A. Turbulent Entrainment and Mixing in Clouds: A New Observational Approach. *J. Atmos. Sci.*, **104**, no. 4, pp. 387-404, 1992.

Boers, R., H.W.J. Russchenberg, J.S. Erkelens, V.K.C. Venema, A. Van Lammeren, A. Apituley, and S. Jongen. Ground-based remote sensing of stratocumulus properties during CLARA-1996 *J. Appl. Meteorol.*, **39**, no. 2, pp. 169–181, 2000.

Cohn, S.A., R.R. Rogers, S. Jascourt, W.L. Ecklund, D.A. Carter, and J.S. Wilson. Interactions between clear-air reflective layers and rain observed with a boundary layer wind profiler. *Radio Sci.*, **30**, pp. 323-341, 1995.

Davis, A.B., A. Marshak, H. Gerber, and W.J. Wiscombe. Horizontal structure of marine boundary layer clouds from centimeter to kilometer scales. *J. Geophys. Res.*, **104**, pp. 6123-6144, 1999.

Davis, A., A. Marshak, W. Wiscombe, and R. Cahalan. Scale Invariance of Liquid Water Distributions in Marine Stratocumulus. Part I: Spectral Properties and Stationarity Issues. *J. Atmos. Sc.*, **53,** no. 11, pp. 1538-1558, 1996.

Ecklund, W.L., C.R. Williams, P.E. Johnston, and K.S. Gage. A 3-GHz Profiler for Precipitating Cloud Studies. *J. Atmos. Sci.*, **16**, pp. 309-322, 1999.

Erkelens, J.S., S. Jongen, H.W.J. Russchenberg, and M. Herben. Estimation of Cloud Droplet Concentration from Radar, Lidar and Microwave Radiometer Measurements. *Proc. Remote sensing of cloud parameters: retrieval and validation*, Delft, The Netherlands, 21-22 Oct, pp. 107-111, 1999a.

Erkelens, J.S., V.K.C. Venema, H.W.J. Russchenberg, and L.P. Ligthart. Coherent scattering of microwaves by particles, evidence from clouds and smoke. *J. Atmos. Sci*, in press, 1999b.

Fox, N.I., and A.J. Illingworth. The potential of a spaceborne cloud radar for the detection of stratocumulus clouds. *J. Appl. Meteorol.*, **36**, no. 6, pp. 676-687, 1997.

Gage, K.S., C.R. Williams, W.L. Ecklund, and P.E. Johnston. Use of Two Profilers during MCTEX for Unambiguous Identification of Bragg Scattering and Rayleigh Scattering. *J. Atmos. Sci.*, **56**, pp. 3679-3691, 1999.

Frisch, A.S., C.W. Fairall, and J.B. Snider. Measurement of stratus cloud and drizzle parameters in ASTEX with a Ka-band radar and a microwave radiometer. *J. Atmos. Sci.*, **52**, pp. 2788-2799, 1995.

Frisch, U. *Turbulence: the legacy of A.N. Kolmogorov.* Cambridge University Press, 296 p., 1998.

Gossard, E.E., and R.G. Strauch. *Radar Observations of Clear Air and Clouds.* Elsevier, 280 p., 1983.

Gossard, E.E., and R.G. Strauch. The Refractive Index Spectra within Clouds from Forward-Scatter Radar Observations. *J. Atmos. Sci.*, **20**, pp. 170-183, 1981.

Grabowski, W.W., and P. Vaillancourt. Comments on 'Preferential Concentration of Cloud droplets by Turbulence: Effects on the Early Evolution of Cumulus Cloud Droplet Spectra.' *J. Atmos. Sci.*, **56**, pp. 1433-1436, 1999. See also reply on pages 1437-1441.

Van de Hulst, H.C. *Light scattering by small particles.* p. 67 & 70, Dover, New York, 470 p., 1981.

Jameson, A.R., A.B. Konstinski, and R.A. Black. The structure of clouds. *J. Geophys. Res.*, **103**, pp. 6211-6219, 1998.

Lammeren, van, A., et al. Clouds and Radiation: Intensive experimental study of clouds and radiation in the Netherlands (CLARA). *Proc. Remote sensing of cloud parameters: retrieval and validation*, Delft, The Netherlands, 21-22 Oct, pp. 5-10, 1999.

Knight, C.A., and L.J. Miller. Early Radar Echoes from Small, Warm Cumulus: Bragg and Hydrometeor Scattering. *J. Atmos. Sci.*, **55**, no. 18, pp. 2974-2992, 1998.

Korolev, A.V., and I.P. Mazin. Zones of Increased and Decreased Concentration in Stratiform clouds. *J. Appl. Meteorol.*, **32**, pp. 760-773, 1993.

Kozikowska, A, K. Haman, and J. Supronowisz. Preliminary results of an investigation of the spatial distribution of fog droplets by a holographic method. *Quart. J R. Met. Soc.*, **110**, pp. 65-73, 1984.

Malinowski, S.P., M.Y. Leclerck, and D.G. Baumgardner. Fractal Analyses of High-Resolution Cloud Droplet Measurements. *J. Atmos. Sci.*, **51**, no. 3, pp. 397-413, 1994.

Ottersten, H. Radar Backscattering from the Turbulent Clear Atmosphere. *Radio Science*, **4**, no. 12, pp. 1251-1255, 1969.

Paluch, I.R., C.A. Knight, and L.J. Miller. Cloud liquid water and radar reflectivity of non-precipitating cumulus clouds. *J. Atmos. Sci.*, **53**, pp. 1587-1603, 1996.

Pinsky, M.B., A.P. Khain, and Z. Levin. The role of the inertia of cloud drops in the evolution of the spectra during growth by diffusion. *Quarterly J. Royal. Meteorol. Soc.*, **125**, pp. 553-581, 1999.

Politovich, M.K., and W.A. Cooper. Variability of the Supersaturation in Cumulus Clouds. *J. Atmos. Sci.*, **45**, no. 11, pp. 1651-1664, 1988.

Pruppacher, H.R, and J.D. Klett. *Microphysics of Clouds and Precipitation; second edition.* Kluwer, Dordrecht, 954 p., 1997.

Rogers, R.R., and W.O.J. Brown. Radar observations of a major industrial fire. *Bull. Am. Met. Soc.*, **78**, no. 5, pp. 802-814, 1997.

Sassen, K., G.G. Mace, Z. Wang, M.R. Poellot, S.M. Sekelsky, and R.E. McIntosh. Continental Stratus Clouds: A Case Study Using Coordinated Remote Sensing and Aircraft Measurements. *J. Atmos. Sci.*, **56**, pp. 2345-2258, 1999.

Sassen, K., and V. I. Khvorostyanov. Radar probing of cirrus and contrails: Insights from 2D model simulations. *Geophys. Res. Let.*, **25**, no. 7, pp. 975-978, 1998.

Shaw, R.A., W.C. Reade, L.R. Collins, and J. Verlinde. Preferential Concentration of Cloud Droplets by Turbulence: Effects on the Early Evolution of Cumulus Cloud Droplet Spectra. *J. Atmos. Sci.*, **55**, pp. 1965-1976, 1998. See also comment by Grabowski and Vaillancourt (and reply) in *J. Atmos. Sci.*, **56**, pp. 1433-1441, 15 May, 1999.

Squires, K.D., J.K. Eaton. Preferential concentration of particles by turbulence. *Phys. Fluids A*, **3**, no. 5, pp. 1169-1178, 1991.

Tatarski, V.I. *Wave propagation in a turbulent medium.* McGraw-Hill, New York, 285 p., 1961.

Vaillancourt, P.A. *Microscopic approach to cloud droplet growth by condensation.* Ph.D. dissertation, McGill University, Canada, 174 p., 1998.

VanZandt, T.E., J.L. Green, K.S. Gage, and W.L. Clark. Vertical profiles of refractivity turbulent structure function: Comparison of the observations by the Sunset radar with a new model. *Radio Sci.*, **13**, pp. 819-829, 1978.

Venema, V.K.C, H.W.J. Russchenberg, A. Apituley, A. van Lammeren, and L.P. Ligthart. Cloud boundary height measurements using lidar and radar. *Physics and Chemistry of the Earth.*, **24**, no. 2, pp. 129-134, 2000.

Wit, de J.J.M., R.J.P. Baedi, J.S. Erkelens, H.W.J. Russchenberg, and J.P.V. Poiares Baptista. Development of retrieval algorithms of cloud parameters from radar and lidar based on the CLARE data set. *Proc. Remote sensing of cloud parameters: retrieval and validation*, Delft, The Netherlands, 21-22 Oct, pp. 83-88, 1999.

Chapter 7

Cloud boundary height measurements using lidar and radar

Abstract. *When only lidar or radar is used, often obtaining an accurate cloud boundary height estimation is not possible. The combination of lidar and radar can give a reliable cloud boundary estimate in a much broader range of cases. However, this combination with standard methods still cannot measure the cloud boundaries in all cases. This will be illustrated with data from the Clouds and Radiation measurement campaigns, CLARA. Rain is a problem: the radar has problems to measure the small cloud droplets in the presence of raindrops. Similarly, few large particles below cloud base can obscure the cloud base in radar measurements. And the radar reflectivity can be very low at the cloud base of water clouds or in large regions of ice clouds, due to small particles. Multiple cloud layers and clouds with specular reflections can pose problems for lidar. More advanced measurement techniques are suggested to solve these problems. An angle scanning lidar can, for example, detect specular reflections, while using information from the radar's Doppler velocity spectrum may help to detect clouds during rain.*

7.1 Introduction

The main objective of the three Dutch Clouds and Radiation (CLARA) campaigns in 1996 was to increase the understanding of radiative processes in the atmosphere by making high-quality cloud measurements [Van Lammeren, 1998]. The instrumentation in Delft (close to the Dutch coast) included: lidars, radar, infrared radiometer, microwave radiometer, and radiosondes. During extended fields of water clouds an

aircraft performed in situ measurements of the drop size distributions with an FSSP-100.

For cloud boundary measurements a main advancement is the synergetic use of lidar and radar, a combination that is also planned to be used in e.g. the European Earth Radiation Mission. For water clouds the radar is normally best at measuring the cloud top and the lidar at measuring the base. However, there are still situations where cloud boundaries are difficult to measure. The problem is often that detectable cloud reflections lack in one of the instruments so that the synergy can not be used. When the lidar signal is totally attenuated, for example, the radar will have to measure both boundaries of possible higher clouds alone. Based on some case studies of low and mid-altitude clouds this chapter will argue that *current* radar measurements are not always up to this task, due to problems with very small or very large particles.

With the current measurement techniques radar cannot measure the radiatively most important (cloud) particles during rain, as the precipitating particles dominate the signal. In such a case lidar would have to measure both boundaries alone, which is often not possible. Ice clouds that produce specular reflections may lead to erroneous interpretations of the cloud boundaries by lidar. For all the above measurement problems new measurement techniques have to be developed and at least the difficulties should be recognised.

Ignoring the problems can lead to large errors and biases. For example, in the Netherlands it rains more than 0.1 mm/hr about 7 percent of the time [KNMI, 1992]. A measurement technique that does not recognise rain can make large errors and just ignoring the rain cases may introduce a bias.

This work aims at improving the understanding of the radar-lidar measurements of cloud boundaries. At least a qualitative understanding of the microphysical cloud properties and scattering is necessary to understand the cloud boundary measurements. This chapter will focus on some situations that can be difficult to measure, illustrate them with measurements and suggest a direction for new measurement techniques.

7.2 Instruments

7.2.1 Radar

The Delft Atmospheric Research Radar (DARR) is a 9-cm Frequency Modulated Continuous Wave (FM-CW) Doppler radar. The radar measurements are averaged over 5 s, the beam width is 1.8°, the sensitivity at half the maximum range is about -27 dBZ and the range resolution can be set to 15 or 30 m, giving a maximum range of respectively 4 or 8 km. For small randomly distributed waterdroplets the received power is proportional to the diameter to the sixth power. As the wavelength of

DARR is much longer than that of typical cloud radars, some of the reflections may be due to spatial refractive index variations, caused by turbulence. In the CLARA database we estimate that 13 % of the time the coherent air scatter (clear-air scatter) is more than -20 dBZ in the boundary layer. This means that it may be stronger than reflections from clouds, thus fair weather cumulus may be masked for cm-wave radar. Also variations in mass density of particles on a spatial scale of half the wavelength – coherent particle scatter – can enhance the reflection strength of these particles for cm-wave radars [Erkelens et al., 1999 and Venema et al., 1999]; this could especially be important at edges of clouds.

7.2.2 Lidars

Two different near-infrared backscatter lidar systems were used: The Vaisala CT-75k lidar ceilometer (wavelength 906 nm) and an experimental system (only the wavelength 1064 nm was used): the high temporal resolution lidar (HTRL lidar). The Vaisala is a commercial system, having a range resolution of 30 m and an integration time of 12 s, the pulse repetition rate is 5.1 kHz with an energy of 1.6 mJ. The HTRL lidar stores the single-shot returns at a rate of 1.6 Hz, the pulses of 10 ns have an energy of 0.3 J, and the lidar has a range resolution of either 1.5 or 7.5 m. More information on the HTRL lidar can be found in Apituley (1999). It would be preferable to use lidar to measure cloud boundaries, as it uses light. However, attenuation of the laser beam is very important for lidar. So for a cloud with a high optical depth (typically above about 3), radar measurements are needed, for instance to measure the cloud top height.

The range output of the Vaisala and DARR was intercalibrated on a far away chimney and was correct within one range cell. A comparison between the measurements of the lidar systems shows that the range of the HTRL lidar is equally accurate. The instruments were placed within 15 m of each other. The measurement times were synchronised afterwards. In all case studies presented in this study the instruments pointed to the zenith.

7.3 Observed phenomena

Ideally, the cloud boundary should be derived from the microphysical cloud properties (extinction coefficient or liquid water content) to be most useful for climate studies. At this stage, however, it is not feasible to routinely convert remote sensing measurements of clouds into microphysical cloud properties.

The approach taken in this chapter is to use the measured reflection profiles directly. The height at which the signal decreases considerably will be called cloud top or base. This qualitative approach is sufficient for this study, as the kinds of prob-

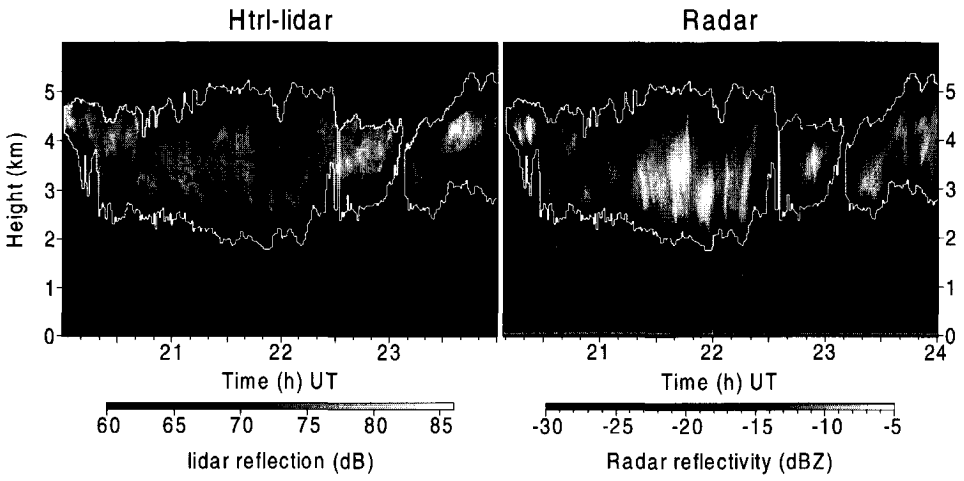

Figure 7.1. Measurement of the vertical reflection profiles of an ice cloud on the 18th of April 1996. Fig. 7.1a is the HTRL lidar range corrected backscatter in arbitrary dB units. Fig. 7.1b gives the equivalent radar reflectivity factor measured by DARR. To facilitate comparison, the contour of the cloud as measured by radar is plotted in both figures. The dots and vertical lines in Fig. 7.1b are point targets of unknown origin, also called angels. The horizontal line at 2.1 km in Fig. 7.1b are an effect of the radar system, and should be ignored.

lems treated are not solved by using a more refined algorithm on the same reflection profiles. Note that with this definition the cloud top and base do not have to correspond to the true (radiatively significant) cloud boundaries.

In this section five case studies with radar-lidar cloud measurements will be presented and qualitatively discussed in terms of the microphysical cloud properties that are relevant for the retrieval of cloud boundaries. Based on the interpretation of these cases some suggestions for new measurement techniques will be given in section 7.4.

7.3.1 Effect of particle size

In general, one can say that radar reflection measurements are dominated by the large particles, whereas the lidar measurements are dominated by the small particles. The importance of this depends on the width of the particle size distribution.

The radar receives reflections from below the cloud base that is measured by lidar in the ice cloud measurement shown in Fig. 7.1. The cloud base of the lidar is in this case likely to be representative. The cloud base measured by radar is thus probably 100 to 500 m too low. A likely cause of these radar reflections is some sparse falling

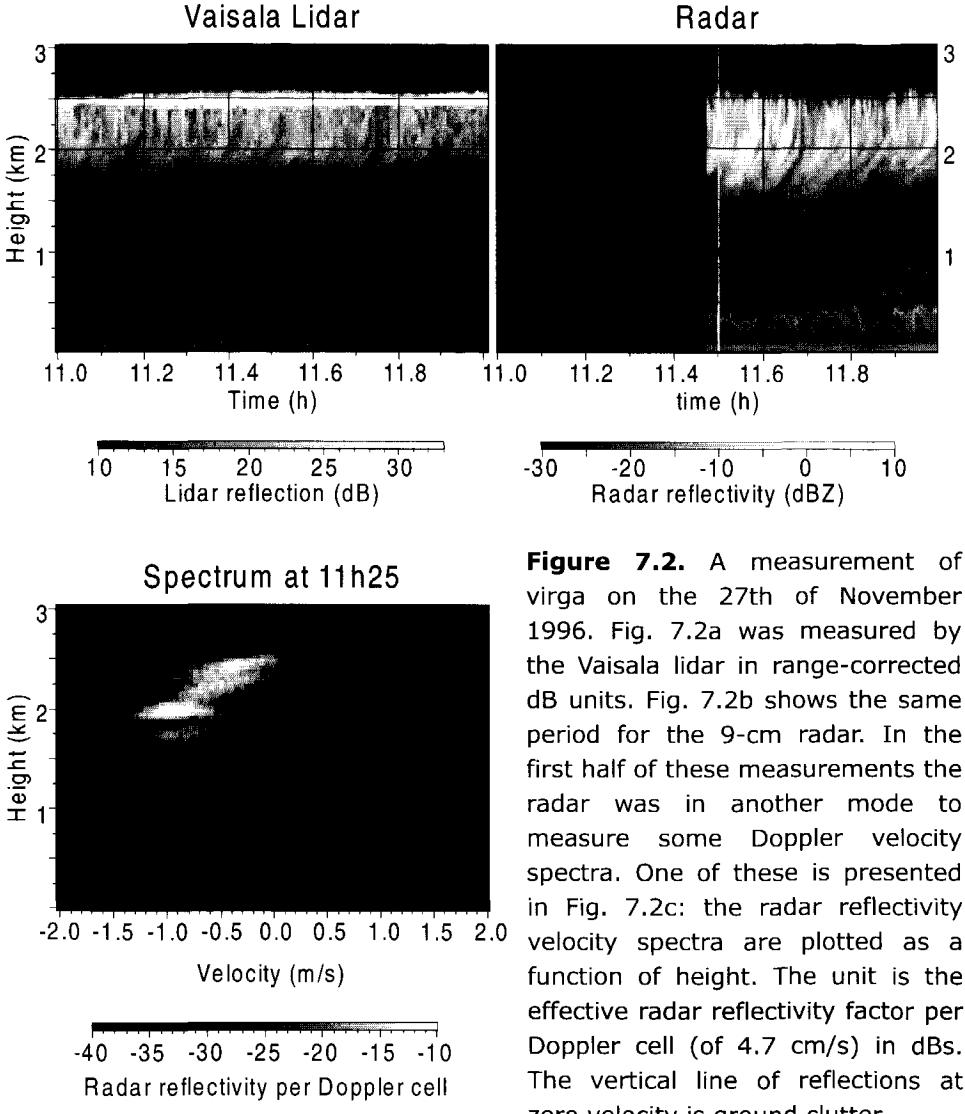

Figure 7.2. A measurement of virga on the 27th of November 1996. Fig. 7.2a was measured by the Vaisala lidar in range-corrected dB units. Fig. 7.2b shows the same period for the 9-cm radar. In the first half of these measurements the radar was in another mode to measure some Doppler velocity spectra. One of these is presented in Fig. 7.2c: the radar reflectivity velocity spectra are plotted as a function of height. The unit is the effective radar reflectivity factor per Doppler cell (of 4.7 cm/s) in dBs. The vertical line of reflections at zero velocity is ground clutter.

crystals (the radar velocity is between 0.5 and 1 m/s downward at the radar cloud base).

Weitkamp et al. (1999) also observed with their 3-mm wavelength cloud radar a base of an altocumulus, which was 100 to 600 m too low. The base measured by DARR of clouds containing ice is often observed to be lower than the base measured by lidar. It seems to be a typical error for ice clouds that the cloud base measured by radar is a few hundred metres too low. For DARR this may also be explained

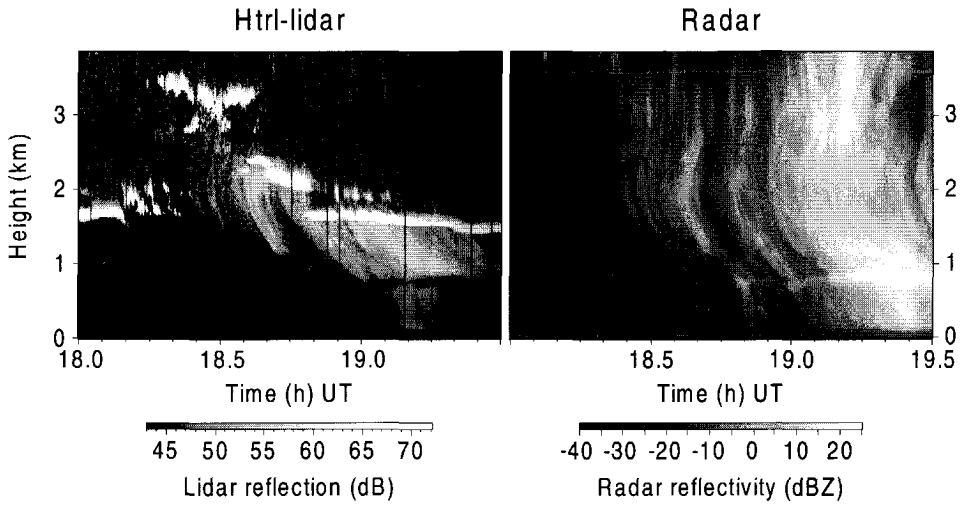

Figure 7.3. This measurement of light rain (on the 6th of December 1996) shows a large difference between the HTRL lidar (Fig. 7.3a) and the radar (Fig. 7.3b). The multiple stratus layers visible in the lidar measurement are not present in the radar, which only sees the reflections from the falling crystals. The 0-degree isotherm is at 800 m, which is revealed by the traditional bright band in the radar and a dark band in the lidar. This dark band is discussed in Venema et al. (1998) and Sassen and Chen (1995).

by coherent air scatter (Bragg), see Rogers and Brown (1998), but for this case that seems unlikely as coherent air scatter should have a Doppler velocity around 0 m/s. Note that the cloud (Fig. 7.1) is called an ice cloud because the radar reflection is dominated by ice crystals. However, it can also be a mixed cloud, and the lidar may receive backscatter from waterdroplets. In the entire cloud the structures seen by radar are more vertical – indicating large falling particles – and by the lidar more horizontal – indicating small floating particles.

Another example of the effect of large particles on radar measurements is shown in Fig. 7.2. This measurement of virga (precipitation that does not reach the ground) was made on November 27, 1996. The lidar backscatter (Fig. 7.2a) shows a thin stratus layer at 2.5 km, with ice crystals precipitating out of this cloud and evaporating above 1.5 km. The radar (Fig. 7.2b) only sees the reflections of the large falling ice crystals; the presence of the cloud at 2.5 km does not even increase the radar reflections significantly. The radar 'cloud base' is in this case placed almost one kilometre too low. A distinction between the small cloud particles and large falling crystals is possible if information present in the Doppler spectrum is used; a good example is Fig. 7.2c. The cloud seen by lidar at 2.5 km is revealed by the small radar reflections with a positive upward velocity.

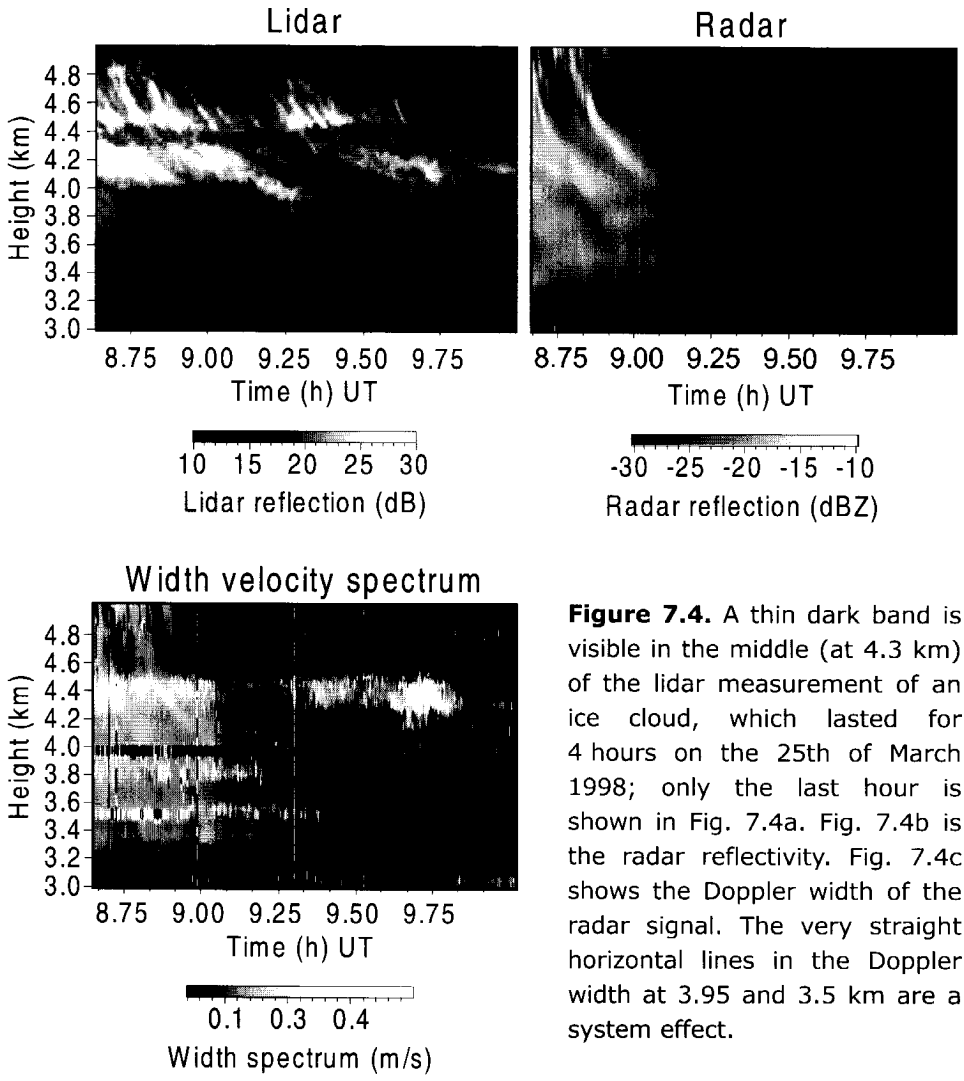

Figure 7.4. A thin dark band is visible in the middle (at 4.3 km) of the lidar measurement of an ice cloud, which lasted for 4 hours on the 25th of March 1998; only the last hour is shown in Fig. 7.4a. Fig. 7.4b is the radar reflectivity. Fig. 7.4c shows the Doppler width of the radar signal. The very straight horizontal lines in the Doppler width at 3.95 and 3.5 km are a system effect.

The contrast in particle size is also very large in rain. Figure 7.3 shows a very light rain event (December 6, 1996), which at its peak is no more than 1 mm/hrs and the drops have a maximum fall speed of 5 to 6 m/s. The three stratus clouds present in the lidar measurement (Fig. 7.3a) are not distinguishable in the radar measurement (Fig. 7.3b). In the measured velocity it can be seen that the reflections from the precipitation dominate the total reflection so strongly that the *average* velocity also does not reveal the position of the clouds. A retrieval of the cloud boundaries by current radar techniques is thus not possible.

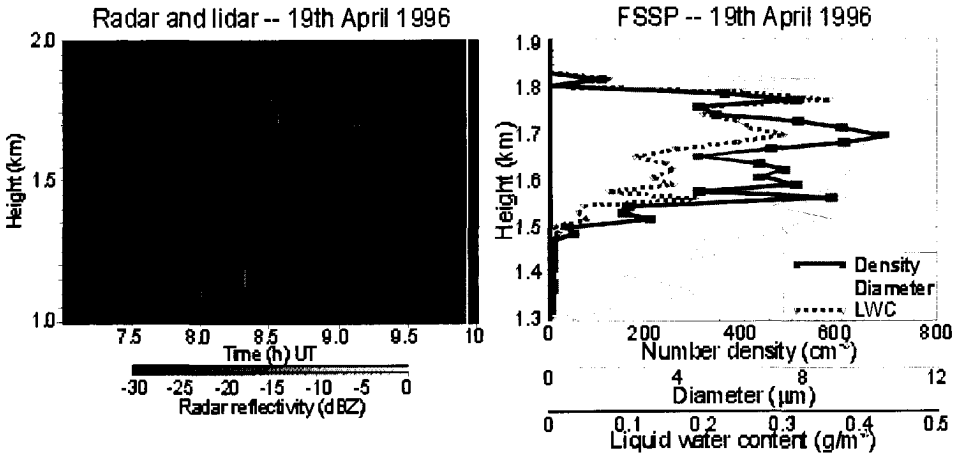

Figure 7.5. A stratocumulus cloud measured with radar and lidar (Vaisala) is shown in Fig. 7.5a. The background of the figure is the radar reflectivity and the contours the range-corrected lidar backscatter. The contours are 10 dB apart. The peak of the vertical profile of the radar is significantly above the peak of the lidar. The radar receives power from a region where the lidar does not receive any backscatter. Figure 7.5b shows the averaged number of droplets, the average drop size and Liquid Water Content as measured with an FSSP-100. For these profiles all data from a 3-hour measurement in a region 50 km around Delft was used.

Ice clouds can also contain very small ice crystals, especially at the cloud top. In the second part of the ice cloud radar measurement shown in Fig. 7.4a, the radar does not detect most of the cloud. This is probably because the particles are too small here, as the cloud is gradually decaying. The radar would make an error in both the cloud top and base in the last part of this measurement. Weitkamp et al. report a total multi-layered cirrus cloud that their cloud radar could not detect as the reflectivity was below -30 dBZ.

One CLARA measurement of stratocumulus is shown in Fig. 7.5a; for this cloud in situ FSSP data is available as well, see Fig. 7.5b. The cloud base as measured by lidar is about a 100 meters below the first radar signals from DARR. This is because the radar reflection from the small droplets (just 10 μm) at cloud base is much too small, which was confirmed by calculating the radar reflectivity belonging to the drop size distributions from Fig. 7.5b. Based on a simple model for a stratus water cloud Sassen et al. (1999) estimate that a radar with a minimum detectable signal of -30 dBZ will detect the first signals 200 m above the lidar cloud base.

7.3.2 *Effect of attenuation*

Although for 95 Ghz radar attenuation can be a problem [Danne et al., 1999], for cm-wave radars the attenuation can be neglected. In the case of lidar, it is common that the clouds (especially clouds containing water) are optically too thick for the light to penetrate to the cloud top. Another problem is that from the measured lidar backscatter profiles it is hard to determine whether the signal decreases towards the noise level due to total attenuation or because the top of the cloud is reached.

In the ice cloud shown in Fig. 7.1, the cloud 'top' measured by lidar is often a few hundreds of meters lower than the radar cloud top, especially between 21 and 22 hours. This height difference is likely to be caused by attenuation of the lidar signal.

In the lidar measurement of light rain (Fig. 7.3a) three cloud layers are present. The upper two layers are not visible in the last part of the lidar measurement due to attenuation by the lowest cloud, but at least the cloud producing the precipitation should still be present. As the radar cannot measure the clouds due to the rain, there is no information on the cloud base of the two upper clouds and no information on the cloud top of the lower two clouds.

The stratocumulus cloud measured on the 19th of April 1996 shows a peak at different heights for lidar and radar (Fig. 7.5a). During most of the measurement the lidar received no power from the region where the radar sees the cloud. The bumpy character of the cloud makes it hard to analyse. One can only speculate whether the lidar power was attenuated in the region of the radar reflections or whether the radar received reflections from above the cloud (maybe clear air scatter).

7.3.3 *Effect of specular reflections*

Non-spherical ice crystals can reflect light almost like a mirror; this can cause specular reflections in the vertical direction due to horizontally aligned ice crystals. The largest dimension of the crystal can be horizontally aligned due to aerodynamical forces. Thomas et al. (1990), for example, measured an angular dependence in lidar echoes of a cirrus cloud of just 0.3° around the zenith. Likewise, theoretically a decrease in the vertically backscattered power should result when the ice crystals are no longer aligned horizontally, compared to the aligned case.

A lidar measurement of an ice cloud on the 25th of March 1998 (Fig. 7.4) shows a dark band at about 4.3 km height. The cloud and its dark band (a layer of reduced backscatter) lasted about 4 hours. The dark band is about 10 dB deep. Only the last hour is shown, as for this part radar data was available as well. The first two hours the dark band was 200 to 300 m wide, the last two hours about 100 m. Fall streaks with high lidar and radar echoes fall from the top part, through the dark band into the lower part. The width (standard deviation) of the velocity spectrum is about

3 times larger in the dark band than in its environs; an indication of turbulence. At the height of the dark band itself there are still some radar reflections after 9.25 hrs (see Fig. 7.4b), which could either be some residual particles, or coherent scattering due to the turbulence.

Data from a radiosonde at 6 hrs UT revealed a strong change in wind direction. At 4 and 4.6 km the wind direction was North, but in the dark band it was East; In the dark band the wind direction was constant over 200 m, the wind speed 1 m/s and the temperature was -17 °C. The radiosonde recorded a relative humidity from 75% at 4 km to 90% at 4.5 km. The presence of liquid water is thus not likely.

A possible explanation of this measurement is that in the upper and lower part the lidar backscatter is high due to specular reflections from horizontally aligned ice crystals and that in the dark band these crystals are no longer horizontally aligned due to turbulence. Unfortunately, there were no lidar measurements with a beam that is directed a few degrees away from the zenith. These would be needed to ascertain whether or not the lidar backscatter was specular.

Another possibility is that it is a measurement of two separate clouds with a cloud-free region in between. The fall streaks could then connect the clouds by cloud seeding: crystals falling from the top cloud into the lower cloud. However, if this were true the lower cloud should contain water (because of the cloud seeding), which is unlikely, given the radiosonde data. Concluding, specular reflections seem most probable explanation, but it should be directly measured to be sure.

7.4 Proposed advanced measurement techniques

In a large number of cloudy conditions the current measurement techniques suffice to measure cloud geometry. For example, in the first case study of an ice cloud (Fig. 7.1) the cloud boundaries are probably representative for the true boundaries, if we take the lidar cloud base and the radar cloud top. However, to achieve representative operational measurements under more cloud conditions, this section gives some ideas for improved measurement techniques, which would have been useful in the previous case studies, with no attempt of being comprehensive.

7.4.1 Lidar

The measurement artefacts created by specular reflections should disappear when the lidar is tilted under a small angle. Tilting the lidar will also enhance the contrast between cloud droplets and raindrops due to the higher backscatter of raindrops in the vertical direction [Chapter 8]. For the measurement of the microphysical properties and process studies of clouds, specular reflections can be interesting. In these cases a lidar that can automatically scan in angle would be useful; in the case of the

dark band (Fig. 7.4) it could ascertain the specular character of the backscatter. Experiments with a scanning lidar would be needed to see if specular reflections are a significant problem for the measurement of the cloud geometry.

When a lidar receives molecular (Rayleigh) backscatter from a region above the cloud, this can be used to estimate whether the lidar was totally attenuated or not and thus whether the cloud top was measured reliably by lidar. Had Rayleigh scatter been measured above the stratocumulus cloud in Fig. 7.5, this would have simplified the interpretation.

7.4.2 Radar

Using radar for cloud geometry measurements during rain (including rain that does not reach the ground) is possible if information from the Doppler velocity spectra is used. In the case shown in Fig. 7.2c it would suffice to store the reflection of the particles going up. In the measurement of light rain (Fig. 7.3) the cloud may be made visible by looking at the power of the upward moving particles, even though the *average* velocity has not been changed by the presence of the cloud. But as updrafts and downdrafts easily perturb the velocity of the cloud particles, Doppler polarimetry or Doppler multi-frequency spectra may be needed to unambiguously identify the smallest particles. The radar should, furthermore, have a very high sensitivity: Sassen et al. (1999) estimated – based on a simple cloud model – that a radar with a sensitivity of -40 dBZ will give about the same cloud base height as a lidar for water clouds. For ice clouds the sensitivity sometimes needs to be even better [Sassen and Khvorostynov, 1998].

7.4.3 Sensor synergy

It would be useful to have a Doppler lidar next to a Doppler radar for some measurement campaigns. The fall velocity of the particles is a function of the size, next to the shape of the particles. The difference in fall speed between lidar and radar may serve as an indirect measure of the width of the particle size distribution. If both lidar and radar measure about the same particle speed, one would have more confidence in interpreting the combined measurements in terms of one effective particle shape and size. In case of a difference in fall speed, the fall velocity of the lidar (small particles) can be used by a algorithm that detects cloud boundaries in the radar Doppler spectrum.

7.5 Concluding remarks

To make accurate and useful cloud boundary measurements in a broad range of atmospheric conditions, one has to combine lidar and radar. This chapter presented a number of case studies to illustrate the physical processes important for measurements of cloud geometry: the influence of particle size, attenuation and specular reflections. The conclusion drawn from analysing these case studies is that the measurement techniques still have to be improved a great deal before representative operational cloud measurements under all atmospheric conditions are feasible. Difficult conditions are: rain and virga, ice clouds with a broad particle size distribution and ice clouds with specular reflections. How often these problems occur should be the subject of further studies and optimised measurement techniques have to be developed for these cases.

Acknowledgements

The authors would like to thank Christine Unal for calculating the Doppler spectra of virga, and Gerard Kos for carrying out the FSSP measurements. This work was partly funded by the Dutch National Research Programme on Global Air Pollution and Climate Change (NOP).

Reference

Apituley, A., A. van Lammeren, and H. Russchenberg. High time resolution cloud measurements with lidar during CLARA. *Physics and Chemistry of the Earth*, 24, no. 2, pp. 129-134, 2000.

Boers, R., H.W.J. Russchenberg, J.S. Erkelens, V.K.C. Venema, A. Van Lammeren, A. Apituley, and S. Jongen. Ground-based remote sensing of stratocumulus properties during CLARA-1996 *J. Appl. Meteorol.*, **39**, no. 2, pp. 169–181, 2000.

Clothiaux, E.E., T.P. Ackerman, G.G. Mace, K.P. Moran, R.T. Marchand, M.A. Miller, and B.E. Martner. Objective determination of cloud heights and radar reflectivities using a combination of active remote sensors at the ARM CART sites. *J. Appl. Meteor.*, **39**, no. 5, pp. 645-665, May 2000.

Danne, O., M. Quante, E. Raschke, and C. Weitkamp. Investigation of Cloud Layer Base and Top Heights from 95 GHz Radar Reflectivity Data. *Phys. Chem. Earth (B)*, **24**, no. 3, pp. 167-171, 1999.

Erkelens, J.S., V.K.C. Venema, and H.W.J. Russchenberg. Coherent particle scatter in developing cumulus clouds. *Proc. 29th Int. conf. Radar Meteorology*, Montreal, Canada, pp. 904-907, 12-16 July, 1999.

Frisch, F.G., C.W. Fairall, and J.B. Snider. Measurement of stratus cloud and drizzle parameters in ASTEX with a Ka-band Doppler radar and a Microwave radiometer. *J. Atmos. Sci.*, **52**, pp. 2788-2799, 1995.

Lammeren, van A., H. Russchenberg, A. Apituley, and H. Ten Brink. CLARA: a data set to study sensor synergy. *Proc. workshop on Synergy of Active Instruments in the Earth Radiation Mission*, 12-14 Nov. 1997, Geesthacht, Germany, ISSN: 0344-9629, pp. 157-160, 1998.

KNMI, *Climatological data of stations in the Netherlands. Normals and extreme values of the 15 principal stations 1961-1990*, publ. no. 150-27, ISBN: 90-369-2013-2, De Bilt, The Netherlands, 1992.

Rogers, R.R., and W.O.J. Brown. Interactions between scattering by precipitation and the Clear air. *Proc. of the 8th URSI Commission F Triennial Open Symp.*, 22 Sept., Universidade de Aveiro, Aveiro, Portugal, pp. 235-238, 1998.

Sassen, K., and T. Chen. The lidar dark band: An oddity of the radar bright band analogy. *Geophys. Res. Let.*, **22**, no. 24, pp. 3505-3508, Dec., 1995.

Sassen, K., and V.I. Khvorostyanov. Radar probing of cirrus and contrails: Insights from 2D model simulations. *Geophys. Res. Let.*, **25**, no. 7, pp. 975-978, Apr., 1998.

Sassen, K., G.G. Mace, Z. Wang, M.R. Poellot, S.M. Sekelsky, and R.E. McIntosh. Continental Stratus Clouds: A Case Study Using Coordinated Remote Sensing and Aircraft Measurements. *J. Atmos. Sci.*, **56**, pp. 2345-2258, 1999.

Thomas, L., J.C. Cartwright, and D.P. Wareing. Lidar observations of the horizontal orientation of ice crystals in cirrus clouds. *Tellus*, **42B**, pp. 211-216, 1990.

Venema, V.K.C., J.S. Erkelens, H.W.J. Russchenberg, and L.P. Ligthart. Some notes on scattering of radiowaves by clouds. *Proc. Symposium Remote Sensing of Cloud Parameters: Retrieval and Validation*, pp. 63-70, 21-22 October Delft, The Netherlands, 1999.

Venema, V.K.C., H.W.J. Russchenberg, A. Van Lammeren, A. Apituley, L.P. Ligthart. The melting layer: The radar bright band is dark for lidar. *Proc. of the 8th URSI Commission F Triennial Open Symp.*, 22 Sept., Universidade de Aveiro, Aveiro, Portugal, pp. 159-162, 1998.

Weitkamp, C., H. Flint, W. Lahmann, F.A. Theopold, O. Danne, M. Quante, and E. Raschke. Radar and Lidar Cloud Measurements at Geesthacht. *Phys. Chem. Earth (B)*, **24**, no. 3, pp. 163-166, 1999.

Chapter 8

Measurements of the melting layer using lidar and radar: the lidar dark band

Abstract. *The melting layer of precipitation is known for its high radar reflectivity, and is thus called the bright band. The lidar backscatter from the melting region, however, is much lower than that from the ice above and the rain below. One sees a lidar dark band. In this chapter case studies are analysed using lidar and corresponding radar measurements to gain more insight into this dark band. The dark band is 200 to 300 meters wide and the top of the dark band is above the height at which the radar velocity starts to increase. The difference in lidar backscatter between melting layer and its environs is defined as its depth and can amount up to 20 dB compared to the rain below and up to 30 dB compared to the ice precipitation above. Furthermore, the depth is not statistically related to the number density in the rain, as estimated by radar. Possible explanations of the dark band that are discussed are: crystal imperfections, particle aggregation and breakup, collapse of the particle, enhanced backscatter of raindrops for vertically pointing lidar, enhanced vertical backscatter of the ice precipitation, blockage of the backscatter from the rear surface of a drop by an ice nucleus, and absorption. A likely explanation of the reflectivity difference between the melting layer and the rain is the flattened shape of the raindrop due to the frictional force. For the explanation of the difference between the melting layer and the ice precipitation above several good candidates exist. The quantitative contributions of each of these possible mechanisms cannot be given yet, but some suggestions for research are made that can test and/or quantify these possibilities.*

8.1 Introduction

Midlatitude rain is mainly produced by the cold rain formation process. In this process water vapour is gathered on ice crystals that grow and subsequently fall down. While the crystals fall, the temperature increases and the ice crystals melt into raindrops. In stratiform rain this melting layer is at a well-defined height below the 0-degree isotherm.

The melting layer has been subject of much research. Amongst others it can be important for dynamic effects on the microscale, convective scale, and mesoscale due to the melting-induced air cooling [Szyrmer and Zawadzki, 1999]. In radar measurements the melting layer is visible as a layer with high reflections: the bright band. Because of these strong reflections the melting layer can introduce errors in the rain rate estimated by rain radars. The melting layer can, furthermore, attenuate and distort a polarised signal on a radio link through the layer [Goddard, 1996].

New and unexplained are measurements of the melting layer by lidar [Venema et al., 1998]. This optical instrument receives fewer reflections from the melting layer than from either the ice precipitation above or the rain below. To this phenomenon the name dark band was given. Sassen et al. (1995) published the first clear measurement of a dark band.

The radar bright band is usually explained by an increase of the radio refractive index of the melting particle at the top of the melting layer and a decrease of particle size and number density (both due to collapse of the melting particle) at the bottom of the melting layer (e.g. Russchenberg et al. (1996)). Aggregation (in the top) and breakup (bottom) work together to increase the particle size in the middle of the melting layer. This enhances the radar reflectivity of the melting layer as well. There is still an ongoing debate on in which cases this is significant [Szymer and Zawadski, 1999; Barthazy, 1998].

A full understanding of the dark band will require knowledge of both precipitation physics and scattering by melting particles. Both are still insufficiently known, as the nature of the precipitation particles is not known and scattering calculations on melting particles are computationally intensive. Instead this study will focus on the data analysis of lidar and radar measurements. The measured properties will serve as a constraint for possible explanations. These explanations are qualitatively discussed in relation to the data analysis. The measurements come from the CLARA (CLouds And RAdiation) database, an extensive multi-sensor field campaign of clouds in the Netherlands, held in 1996 [Van Lammeren et al., 1999; CLARA web pages]. As such they were not specifically optimised for studying the melting layer.

The instrumentation is described in section 8.2. The main part of this chapter is a detailed analysis of a few case studies with lidar/radar measurements: section 8.3. The measurements are summarised and discussed in section 8.4. The measurement analysis is used in section 8.5 and 8.6 to evaluate some possible explanations. To test

these explanations further, section 8.7 gives some recommendations for further work, together with the conclusions.

8.2 Instruments

8.2.1 Lidars

Two different near-infrared backscatter lidar systems were used: The Vaisala CT-75K lidar ceilometer (wavelength 906 nm) and the RIVM-High Temporal Resolution Lidar (HTRL lidar, using the wavelengths 1064 and 532 nm). The Vaisala is a commercial system made for operational use at airports, having a range resolution of 30 m and a beam width of 0.038° (0.66 mrad). The integration time is 12 s, the pulse repetition rate is 5.1 kHz with an energy per pulse of 1.6 mJ. Due to a beam splitter in the system, the Vaisala is 2.7 times more sensitive to the cross-polar return than to the co-polar return [Tanner, pers. comm., 2000].

The HTRL system stores the single-shot returns at a rate of 1.6 Hz; the pulses of 10 ns have an energy of 0.3 J. The lidar has a range resolution of either 1.5 or 7.5 m and a beam width of 0.029° (0.5 mrad). The sensitivity to both polarisation states is equal for this lidar system. More information on the HTRL system can be found in Apituley et al. (2000). All lidar backscatter profiles presented in this chapter are in a range-corrected arbitrary dB scale.

8.2.2 Radar

The Delft Atmospheric Research Radar (DARR) is a Frequency Modulated Continuous Wave (FM-CW) Doppler radar with a wavelength of 9 cm. The radar measurements are averaged over 5 s, the beam width (−3dB full width) is 1.8° (31 mrad), the sensitivity at half the maximum range is about −27 dBZ and the range resolution is typically set to 15 or 30 m, giving a maximum range of 4 or 8 km, respectively. The antennas can be steered in any direction, but for these measurements they always pointed to the zenith.

The range output of DARR and the Vaisala ceilometer were intercalibrated on a distant chimney and were found equal within one range cell. A comparison between the measurements of both lidar systems shows that the range of the HTRL lidar is equally accurate. The instruments were placed on a roof within 15 m of each other; the building is 100 m high. The heights presented in this work are relative to the roof and the measurement times were synchronised afterwards. In all case studies presented in this chapter the instruments pointed to the zenith, except where indicated.

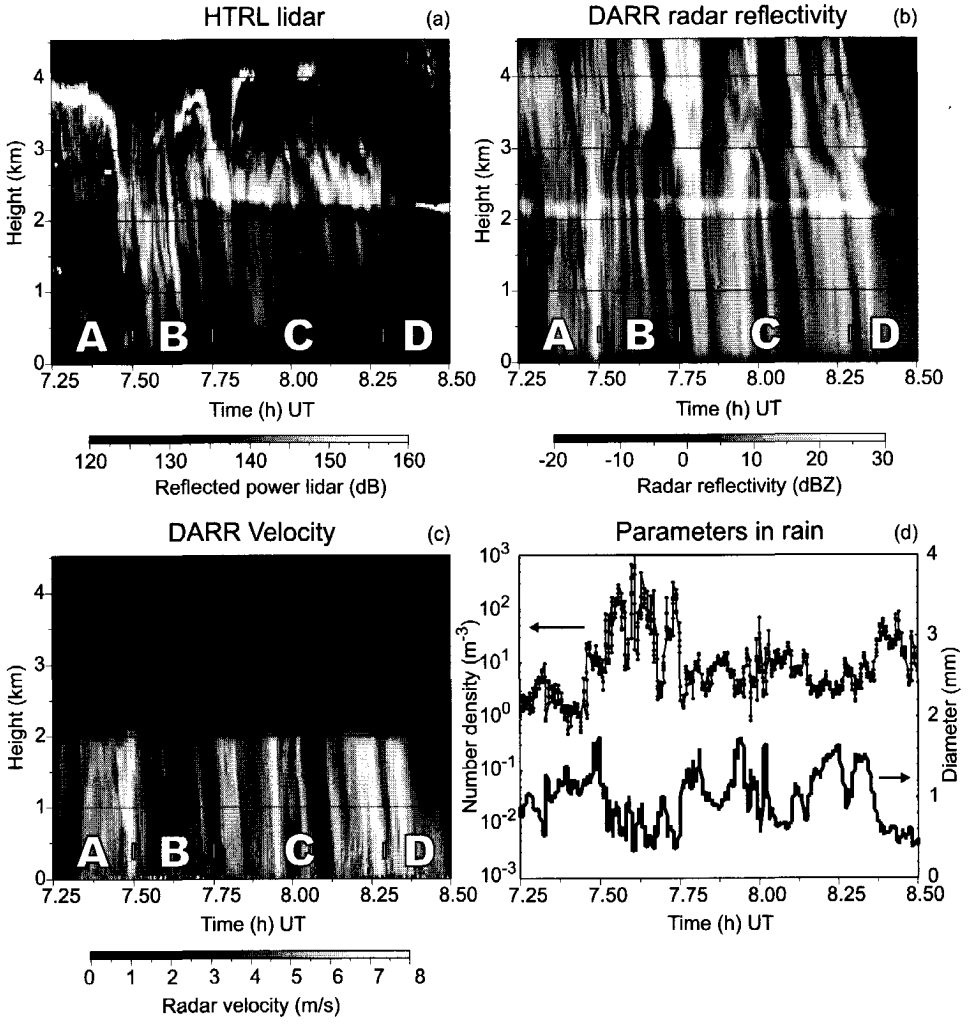

Figure 8.1. Lidar (HTRL lidar) backscatter (a) and radar reflection (b) on the 23rd of April 1996. The radar shows a bright band in the melting layer at 2.2 km. The lidar sees a dark band at this height. Fig. 8.1c shows the radar reflectivity weighted average velocity. From the velocity and radar reflectivity in the rain, the diameter and number density are calculated (Fig. 8.1d). Figure 8.1e and f are on the next page.

8.3 Measurements

A cursory look in the CLARA database (50 days of measurements) reveals that the dark band in the melting layer is common. In case the lidar was not attenuated too much at the height of the melting layer, most, though not all events showed a dark

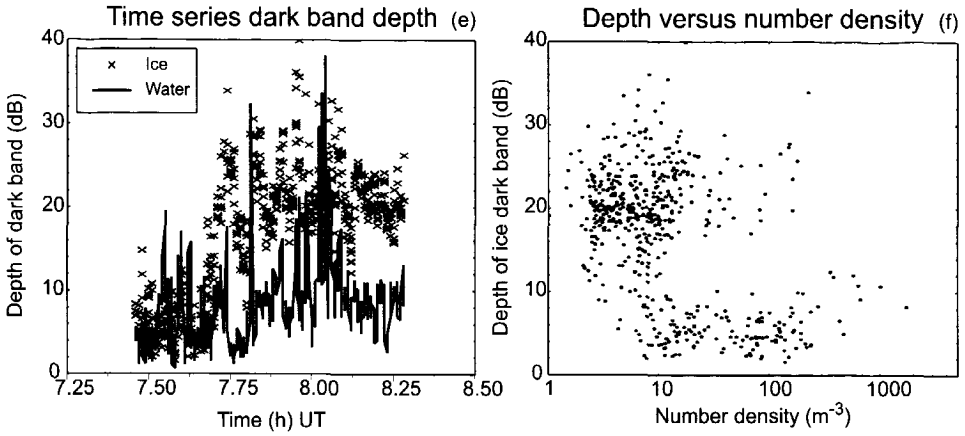

Figure 8.1. The depth of the dark band compared to the backscatter in the ice precipitation above and the rain below (water) are plotted in Fig 8.1e. Fig. 8.1f shows a scatter plot of the depth of the lidar ice dark band (relative to the cloud) as a function of the number density in the rain measured by radar. Figure 8.1a to d are on the previous page.

band. In this section three measurements from the CLARA campaigns will be presented in detail, together a measurement with the lidar and radar of the university of Bonn, and the main points from the measurements of K. Sassen.

8.3.1 Deep dark band

On the 23rd of April 1996 a measurement was made of quite showery, but still stratiform rain. This measurement is presented in Fig. 8.1. The lidar dark band for this case is remarkable as it is very deep, i.e. the difference in lidar backscatter between the melting layer and its environs is very large.

The range corrected HTRL lidar backscatter in an arbitrary dB scale is shown in Fig. 8.1a. The melting layer is at about 2200 m and is visible as a horizontal dark band with low lidar backscatter. In the first part (A), till 7.50 hrs, the rain is very light and evaporates before it reaches the ground. There is little attenuation of the lidar signal by the precipitation, as is indicated by the cloud layer with high reflections between 3.5 and 4 km. In most of this measurement the total attenuation in the thin dark band is probably small. The lidar backscatter from the rain is much stronger in the second part (B), from 7.50 to 7.75 hrs. The dark band is much less deep in this region. The dark band is most striking in part C, between 7.75 and 8.25 hrs UT. After 8.25 hrs, part D, the lidar signal becomes too low and a cloud starts to develop just above the melting layer.

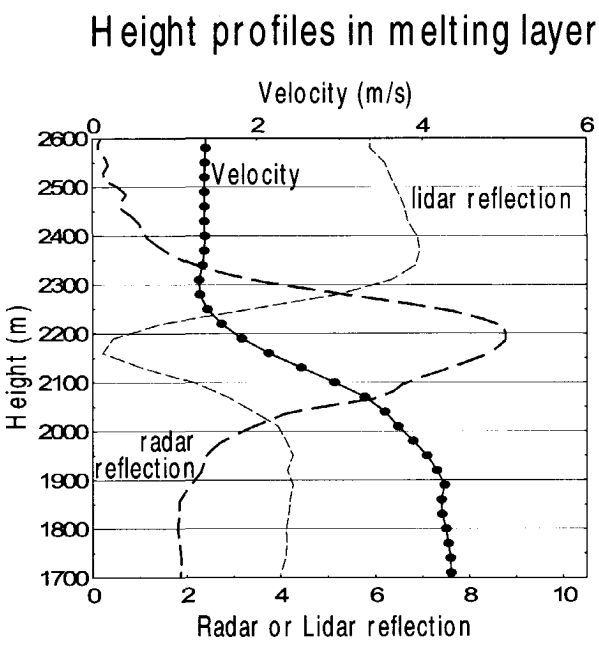

Figure 8.2. Average height profiles of the radar reflection, lidar backscatter (Vaisala) and radar velocity for the time period with the deepest dark band (7.7 to 8.2 h UT). The radar reflectivity is given in dBZ, the lidar backscatter is in a range corrected arbitrary dB scale.

The simultaneous radar measurement is shown in Fig. 8.1b (radar reflectivity factor) and 1c (radar reflectivity weighted average velocity). The radar reflection in the rain varied between 0 and 20 dBZ (which is typical for all dark bands seen in the CLARA database). The four regions seen by lidar come back in the radar data. Note that part B, with the strong lidar reflections in the rain, is characterised by relatively small velocities and lower radar reflectivities.

To investigate the dependence of the depth of the dark band on the microphysical properties of the rain, these properties are estimated in this section. The temporal behaviour of the diameter and the number density of the raindrops just below the melting layer are shown in Fig. 8.1d. They are calculated from the radar reflectivity and radar velocity, see the appendix for the method. The raindroplets have diameters in the order of 0.5 to 2 mm. During most of the measurement the number density in the rain is in the order of 10 m^{-3}; only in part B higher number densities occur. For these rain parameters the total area of the raindroplets can be calculated, which is proportional to the lidar backscatter. The difference in this total area between region B and C is consistent with the difference in lidar backscatter between

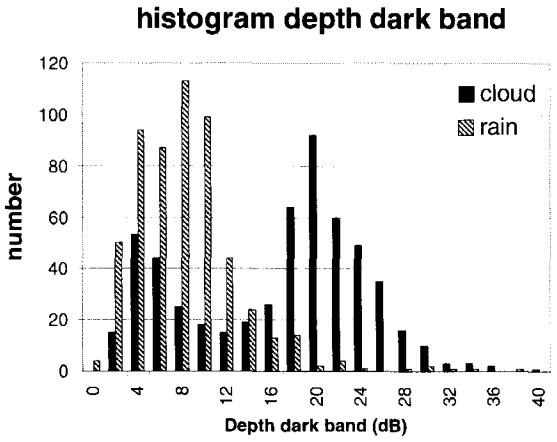

Figure 8.3. Histogram of the strength of the backscatter in the dark band (as measured by the HTRL-lidar) compared to the backscatter in the ice precipitation and in the rain. The distribution of the ice dark band depth has two peaks. The peak around 4 dB corresponds to region B in the measurement shown in Fig. 8.1 and the second peak mainly contains values from region C.

these regions. We expect that this calculated number density in the rain is related to the number density in the ice precipitation above the melting layer.

To compare these microphysical parameters to the depth of the dark band we must quantify this depth. We choose to base the depth directly on the measured backscatter profiles. The minimum backscatter in the melting layer is subtracted from the maximum backscatter in a region just above (ice) or below (water). In this work the former will be called *ice* dark band and the latter will be called the *water* dark band. The result of this exercise is plotted in Fig. 8.1e. Regions A and D and backscatter profiles with insufficient power have been removed.

A scatterplot of the calculated ice dark band depth and the number density is shown in Fig. 8.1f. This plot was made from all data in Fig. 8.1e. There are two groups in this plot. The group with the high number density (and small drops) and the shallow ice dark band depth comes mainly from part B and the group with the low number density and the deep dark band is mainly from part C. A high number density (and a small drop size) thus relates to a less deep dark band in this example.

In part C viewed separately, the dark band depth correlates 28 (ice) and 29 percent (water) with the diameter and the number density together. The main cause of

this correction comes from the negative correlation between dark band depth and the diameter of the particles; the contribution of the number density is not significant. Meaning that within region C smaller particles are statistically related to a deeper dark band. A reliable estimate of the correlation in part B is not possible as the rain rate fluctuates too much and the time period is small.

How the measured variables behave as a function of the height (and indirectly the melted fraction) can be seen in Fig. 8.2. Plotted in this figure are the average profiles from the period with the deepest dark bands. The heights of the significant features relative to each other as mentioned in the next section are also present in the non-averaged profiles.

The melting first affects the radar reflectivity, which starts to increase around 2500 m by increasing the radio refractive index. The lidar reflection decreases at 2350 m, whereas the velocity starts to increase 100 m lower, at 2250 m. This velocity change is an indication that at this height the external structure of the particles starts to change. At 2200 m the radar bright band reaches its peak and at 2150 m the dark band reaches its lowest value. The lidar backscatter remains more or less constant below 1950 m, whereas the radar variables attain their rain values somewhat lower, below 1900 m. In this average profile the width (height difference between top and bottom) of the dark band is about 400 m; in the individual profiles it is in the order of 300 m. The depth of the dark band is greatly reduced due to the averaging, as the height of the minimum backscatter varies.

In Fig. 8.3a histogram of the depth of the dark band from the values of Fig. 8.1e is presented. One can see that the dark band can be very deep. Compared to the backscatter in the rain the dark band is normally 4 to 10 dB, but values up to 20 dB have been measured. The depth of the dark band compared to the ice crystals has two modes. The peak around 4 dB corresponds to part B of the measurement, whereas part C is responsible for the peak around 20 dB, which contains values up to 30 dB.

Note that the method of data analysis used in this study can enhance the depth of the dark band. The depth of the dark band is operationally defined as the maximum minus the minimum of a part of the backscatter profile. This definition will give some depth for a fluctuating backscatter profile (due to natural variations and noise) without a dark band in it. For a backscatter profile with a dark band this can enhance the depth by a few dB.

Furthermore, the fall streaks in the measurements will spread the calculated values for the depth of the dark band. For example, when a low reflection value in the melting layer is compared to a high reflection value in the rain which comes from a high reflection fall streak with particles that were in the melting layer some time before. The highest (and the lowest) values found for the depth may thus be too high (or too low).

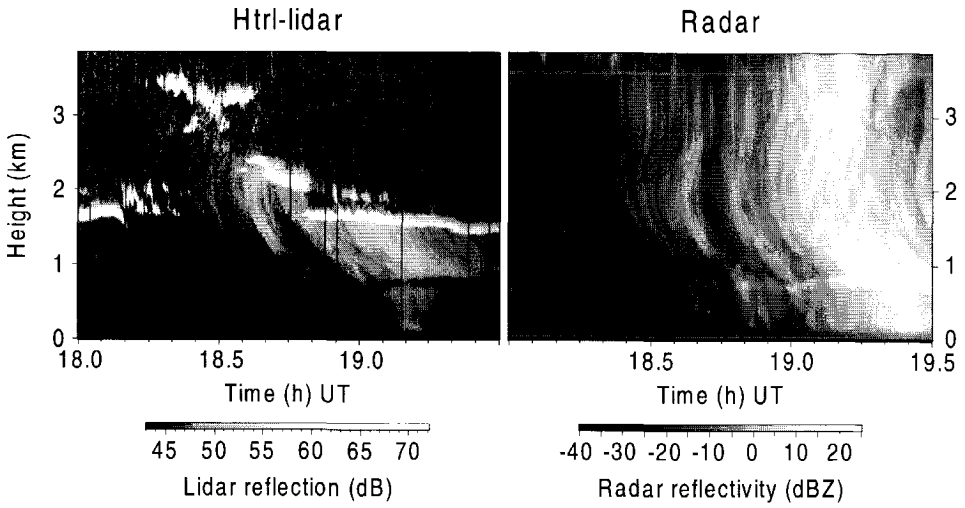

Figure 8.4. A measurement of light rain on the 6th of December 1996. In this case the melting layer is clearly separated from the clouds that are producing the ice precipitation. The fall streaks in the lidar and radar reflections of the ice precipitation below the cloud match very well in angle. The precipitating part is shown in more detail in Fig. 8.5.

Radiosondes were released at a site close to the radar and lidars. From the heights given by the radiosonde 100 m has been subtracted to make the values mentioned here comparable to the readings from the instruments on the roof. At 6.00 hrs UT the radiosonde measured a relative humidity at 2 km of about 70 % and the one at 12.00 hrs of 50 %. The zero-degree level at 6.00 hrs was 2260 m and at 12.00 hrs it was at 2380 m. The temperature in the middle of the melting layer (2200 m) was 0.5 °C (6 hrs) and 1.5 °C (12 hrs). All values have to be used with caution, as it is possible that the rain event changed the profiles of these variables.

8.3.2 Clouds high above dark band

During the rain event on the 6th of December 1996 there were multiple cloud layers, see Fig. 8.4. In this case it is clear that the clouds producing the ice precipitation (the lowest one at 1500 m) are well separated from the melting layer (at 800 m).

The zero-degree level was at 1500 m (!), 800 m above the melting layer, as indicated by a radiosonde released at 18 hrs UT in De Bilt, 50 km away from the measurements site. Between 1500 and 900 m the temperature rose very slowly to a value of about 1 °C at 900 m. The temperature at the radar maximum (800 m) was 1.6 °C and at the lidar minimum (700 m) 2.5 °C. The humidity dropped from 85 to 75 % between 1500 and 900 m and was around 73 % at the height of the melting layer

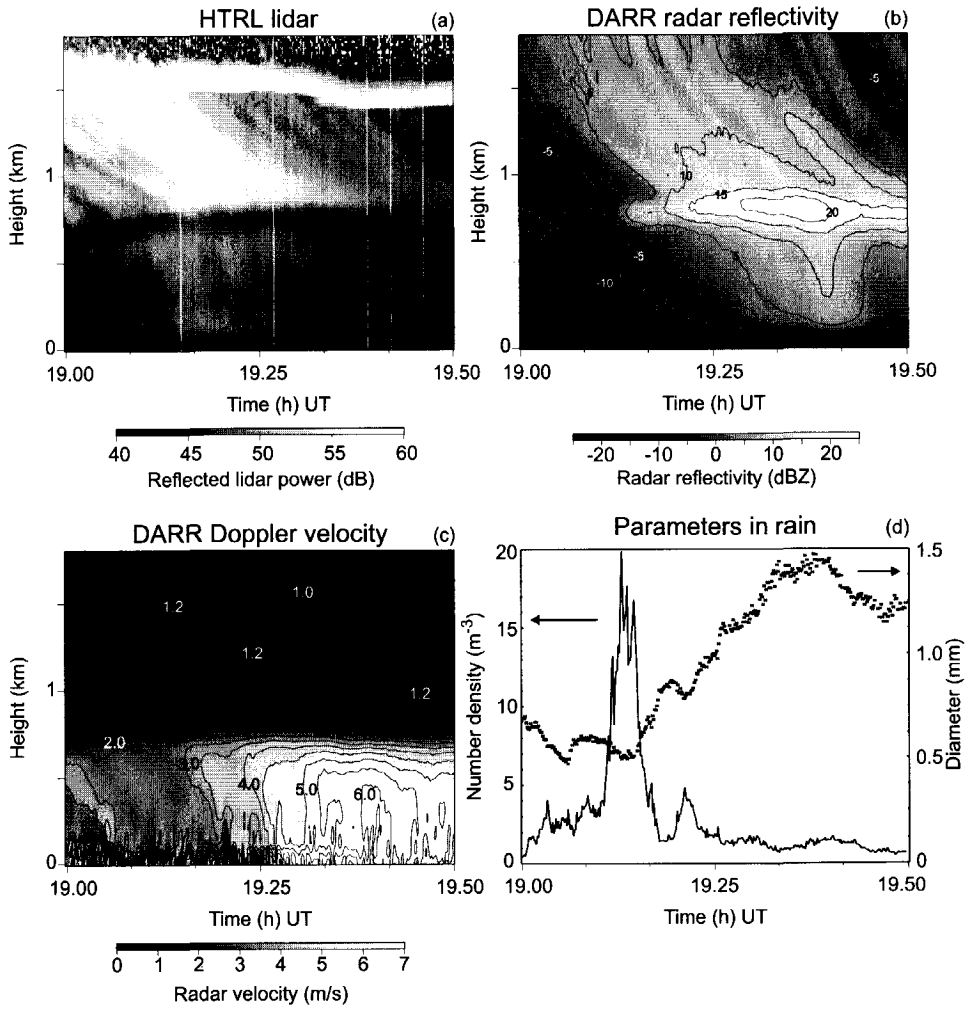

Figure 8.5. Lidar backscatter (a) and radar reflection (b) of the 6th of December 1996. The melting layer is around 800 m. Fig. 8.5c shows the radar reflectivity weighted average velocity. The diameter and number density from Fig. 8.5d are calculated from the average velocity and radar reflectivity in the rain. Figures 8.5e and f are on the next page.

In the region with falling crystals between the lowest cloud and the melting layer, the angle of the fall streaks seen by radar and lidar are almost the same. This indicates that the reflections of radar and lidar are dominated by particles with similar fall speeds. As fall speed is a function of size and shape, it is likely that both instruments see more or less the same particles. These falling crystals are relatively large compared to the cloud particles as they fall fast (radar) and the ratio between the

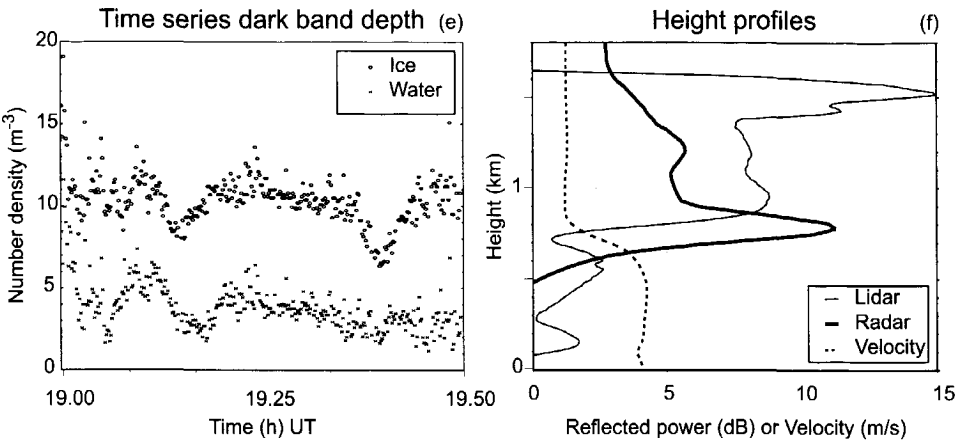

Figure 8.5. The depth of the dark band (Fig. 8.5e) is less than in the previous example. Fig. 8.5f shows the averaged profiles of the three measured variables. Figures 8.5a to d are on the previous page.

radar and lidar backscatter is much larger for these falling crystals than in the cloud layer at 1.5 km.

The rain period is shown in more detail in Fig. 8.5. Note that the lidar signal in the rain is highest in the first half of the measurement (Fig. 8.5a) and that the radar reflectivity is highest in the second half (Fig. 8.5b).

The radar velocity in the rain increases during the rain event from 2 to 6 m/s (Fig. 8.5c), indicating that the average raindrop size is increasing, which is shown in Fig. 8.5d. This change in particle size can qualitatively explain why the lidar-radar reflection ratio is high in the first half of the measurement and low in the second half, as the radar is more sensitive to larger drops compared to the lidar. The number density in the rain was mostly much less than 5 m^{-3}, Fig. 8.5d, except for one peak. At the time of this increase in number density the dark band is less deep.

The depth of the dark band is much less than in the previous example, around 10 dB for the ice dark band and 4 dB for the water dark band, see Fig. 8.5a and 8.5e. Note that the lidar backscatter in the rain is very low for the profiles at the edges of the figure. The dark band computed at the edges is mainly caused by the fluctuating character of the lidar profiles: a calculation of the difference between the maximum and minimum signal in the rain itself (well below the dark band) yielded similar values at the beginning and end of this measurement.

The profile of the variables (Fig. 8.5f) looks similar to the one of the previous example. Again the lidar backscatter drops above the height of the first velocity increase and the lidar dark band reflection minimum is in the lower part of the radar bright band.

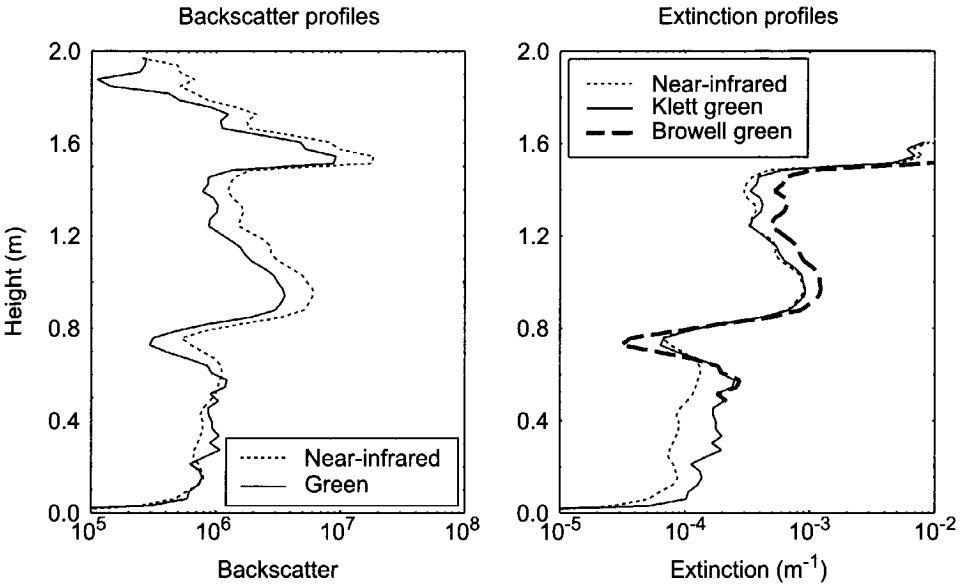

Figure 8.6. Backscatter and extinction profiles of the 6th of December 1996 at 19.15 hrs UT. The backscatter profiles are in an arbitrary range-corrected scale. The extinction profiles are derived from the HTRL lidar data using the algorithms of Browell and Klett. In near-infrared the results are almost identical as molecular backscatter is insignificant for this wavelength, therefore only the Klett result is shown.

To estimate the depth of the dark band accurately one must correct the backscatter signals from the lidar properly for attenuation/extinction. This requires an inversion of the lidar data, which is in fact an ill-posed problem and relies on a priori information. The reliability of the outcome of the inversion procedure therefore critically depends on the validity of the assumptions and the choice of the auxiliary information.

The RIVM-HTRL has a green and near-infrared beam. The backscatter and extinction values at both wavelengths cannot be compared directly as the lidar return at the green wavelength contains a contribution from molecular (Rayleigh) scatter. Accounting for this effect, the contribution to the extinction caused only by particulate matter (e.g. aerosols) is estimated (Fig. 8.6) using an algorithm by Browell at al. (1985). They originally derived it for removing the influence of aerosols on ozone DIAL measurements in the UV. In particular this calculation includes an inversion by a Klett-type backward integration with a constant lidar ratio (extinction to backscatter) set at 36 Sr [Browell et al, 1985]. The choice of the lidar ratio greatly influences the outcome of the extinction values. The calculated extinction profile is only indicative of the order of magnitude of the extinction, as some of the assumptions in

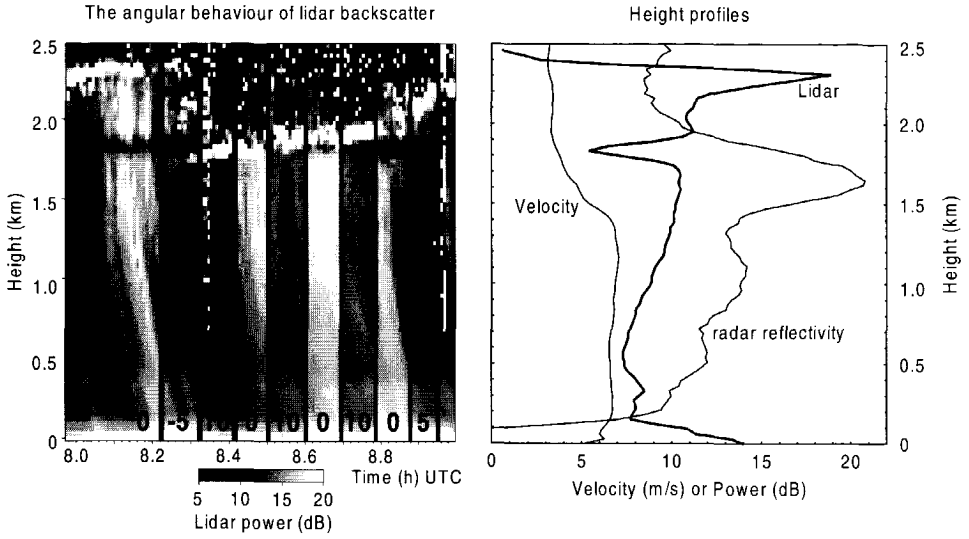

Figure 8.7. The lidar backscatter (Vaisala CT-75K) in the rain as a function of the pointing angle. The angle in degrees is indicated by the big number at the bottom (zenith = 0). The reflections in the rain are 6 to 8 dB lower when measured under a small angle compared to measurements with a lidar pointing at the zenith. The dark band at 1.8 km and the reflections from the ice crystals above it are obscured in the middle of the measurement by a cloud.

the method are unfulfilled. For instance, it is unlikely that the lidar ratio can be assumed constant with altitude in our observations. Furthermore, a constant ratio is in clear contradiction with the flat-drop hypothesis (see Sec. 5.2), which assumes that the backscatter is enhanced at the base of the melting layer, but that the attenuation does not change much here, thereby changing the lidar ratio. The deeper green dark band in the Browell extinction profile, for example, may therefore be an artefact caused by the violation of the assumptions.

8.3.3 Scanning elevation angle lidar measurement

Measurements made on the 1st of April 1998 show that the lidar reflections in the rain are very dependent on the pointing angle, see Fig. 8.7a. If the lidar is pointed to the zenith the reflections are in the order of 6 to 8 dB times as large as the measurement under a small angle with the zenith (–5°, +5°, +10°). Due to this decrease of lidar power in the rain, the depth of the water dark band is reduced. Both the ice and the water dark band are 5 to 10 dB in the beginning of the measurement, up to 8.2 hrs UT.

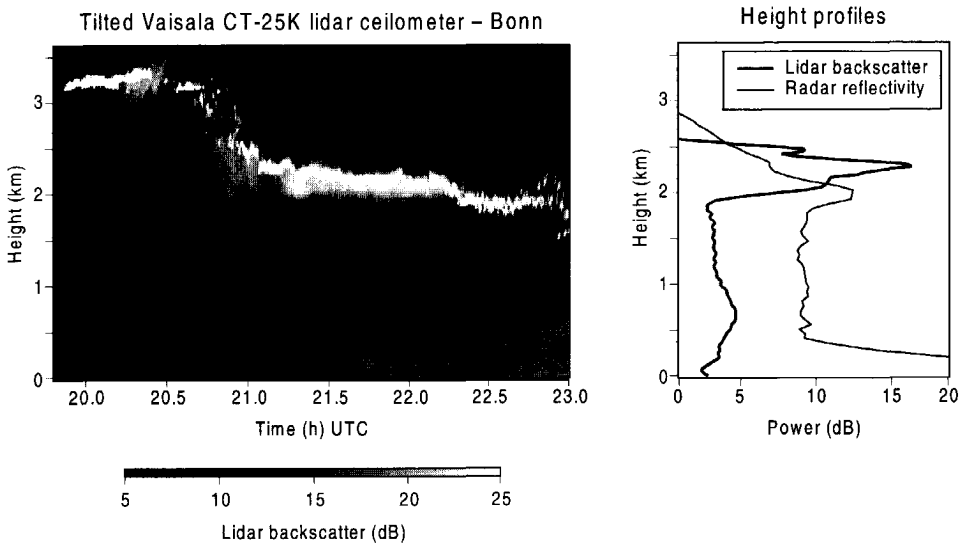

Figure 8.8. A lidar measurement of the melting layer with a Vaisala CT-25K that is tilted, Fig. 8.8a. The angle with the zenith is 26 degrees. The melting layer is between 1.8 and 2.3 km as inferred from an elevation scan with the X-band radar of the University of Bonn, Fig. 8.8b. The lidar reflection is seen to decrease in the middle of the melting layer, but hardly increases again at the base of the melting layer.

In the beginning of this measurement a cloud is seen to precipitate ice crystals, which melt a few hundred meters lower. In the middle of the measurement another cloud unfortunately obscures the melting layer. Because of this cloud only one change of lidar angle can be used to see if the reflections of the *ice precipitation* also depend on the pointing angle. There seems to be a decrease in reflected power above the melting layer at 8.22 hrs UT, when the lidar is tilted. However, this could just as well be a natural fluctuation.

Another interesting feature of this measurement is that the bright band is much wider than the dark band. The dark band is in de order of 200 meter whereas the bright band is 500 to 800 meters wide, see Fig. 8.7b. The dark band is in the upper half of the bright band, around 1800 m. The bright band extents between about 2000 and 1500 m.

8.3.4 Tilted elevation angle lidar measurement

The Vaisala CT-25K of the university of Bonn normally points 26 degrees away from the zenith. This provides us with the opportunity to further study the back-scatter as a function of the elevation angle. A clear measurement of the melting layer

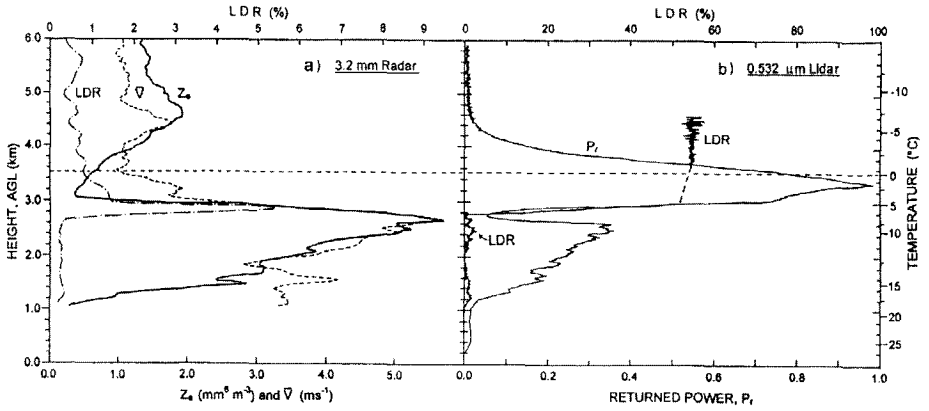

Figure 8.9. A comparison of 90-s averaged vertical profiles of the melting layer from a rain shaft measured by Sassen and Chen (1995). Fig. 8.9a is the W-band (3-mm wavelength) equivalent radar reflectivity factor, mean Doppler vertical velocity V, and linear depolarisation ratio L_{dr}. Figure 8.9b is the range-corrected 532 nm (green) lidar backscatter (in relative units) and linear depolarisation (L_{dr}). Note, that the dashed line in the L_{dr} profile marks a region where the depolarised signals exceeded the data digitizer range, such that the L_{dr} values are underestimated. (From Sassen and Chen (1995); by courtesy of K. Sassen).

is shown in Fig. 8.8. A decrease of lidar backscatter similar to the ice dark band is seen at about 1.9 km; just above it reflections come from the precipitating ice crystals, and above that high reflections come from a cloud layer. Unfortunately, after 22.3 hrs this cloud layer has descended to below the melting layer. In this tilted-angle measurement almost no dark band is seen, which is typical for these measurements, as was inferred from a cursory look at one month of data.

From an elevation scan with the X-band radar of the University of Bonn we estimate that the height of the melting layer was between 1.8 and 2.3 km, see Fig. 8.8b. The profile cannot be compared in detail with the lidar profile as it was composed from the reflectivity values, which are measured 5 to 10 km away from the radar (and lidar), with a range resolution of 450 m and a beam width of about 200 m. The reduction in scattered power occurs at a height of about 1.9 km in the middle of the radar bright band. Because there is a cloud just above the melting layer, an automated retrieval of the depth of the 'dark band' is not possible. The depth of the ice dark band is estimated as 7 to 10 dB. The lidar backscatter hardly increases again in the lower part of the bright band. There still seems to be a small water dark band, which is about 1 dB deep.

8.3.5 Polarisation measurements

Sassen et al. (1995) and Sassen (2000) studied the polarisation behaviour of the dark band lidar measurements. A measured profile of their polarisation diversity lidar is shown in Fig. 8.9b. The water dark band in this profile is about 7 dB deep and the ice dark band 13 dB. Fig. 8.9b shows that the optical linear depolarisation (LDR) is high above the minimum of the dark band and close to zero below. Well above the melting layer the depolarisation is above 50 %. As the digitizer was saturated, the exact values are not known. In another example in Sassen (2000) the LDR above the dark band is 45 to 50 %. Curious in this latter example is the fact that the LDR in the rain has values up to 20 %.

The lidar measurement is compared to a 3-mm radar measurement. In the radar reflectivity no bright band is present in the melting layer, which is typical for an mm-wave radar. The reflectivity does increase as the melting starts, but the slow decrease below 2.6 km is probably caused by evaporation of the raindrops (note that the velocity decreases as well). The radar depolarisation is in this case the best indication of the height of the base of the melting layer. The radar depolarisation peaks at the height of the minimum lidar reflection and is still high in the lower part of the melting layer.

During these measurements a plane equipped with a 2D-C probe made a spiral ascent above the measurement site. At the moment of the flight itself the lidar hardly detected any rain. The 2D-C images that Sassen (1995) shows have irregularly shaped ice crystals above the melting layer and small (less than 1 mm) drops below the melting layer. This plane measured the temperature scale of Figure 8.9 as well.

The melting layer is 750 m below the zero-degree level; the temperature in the melting layer is 6.3 °C. Sassen explains this by sublimation cooling, which is strong in this case as the humidity just above the melting layer is around 40 to 50 percent. This fits the observations of Mitra et al. (1990) that the melting is delayed by 100 m for each 10 percent of subsaturation.

8.3.6 Dark band in radar profiles

In the reflectivity profiles from short cm-wave and mm-wave radars sometimes a small dark band is visible. For example, Fabry and Zawadzki (1995) observed a dark band of 0.5 dB deep at the top of the bright band with an X-band (3.2 cm wavelength) radar during very light rain (the radar reflectivity in the rain was about 0 dBZ).

For mm-radar this dark band can be deeper and (almost) no bright band is present. By comparing radar reflectivity and velocity profiles of light rain measured by the mm-wave radar MIRACLE, kindly provided by GKSS, we conclude that the top of this dark band is located well above the melting layer. The decrease in radar re-

flectivity could be caused by a decrease in particle size due to sublimation, as the velocity also decreases in this dark band. The reflectivity increases again in the top of the melting layer as the radio refractive index increases due to melting.

8.4 Summary and discussion measurements

A significant number of measurements show a difference in lidar backscatter between the ice precipitation and the melting layer of more than 20 to 30 dB and a difference between the rain and the melting layer of 10 to 20 dB.

The dark band is thin. The widest dark band was 200 m to 300 m. This is even the case when the radar bright band is much wider. The decrease in lidar reflection in the top of the melting layer occurs between the start of melting (indicated by an increase in radar reflectivity) and the time when the particles are half melted. Mitra et al. (1990) showed that the velocity of an snowflake started to increase when it was 50 percent melted. This observation has to be used with caution as the lidar return is dominated by relatively small particles compared to the radar reflections. It is thus possible, given a broad particle size distribution, that the lidar return at some height mainly comes from small particles that are already fully melted, while the larger particles that dominate the radar return at that height have only melted a little. In section 8.5 we assume that for the first two case studies the radar-weighted velocity is representative for all particles, i.e. that the particle size distribution is relatively narrow. It would be best, however, to measure the velocity of the particles dominating the lidar backscatter directly.

There is some indication that normally the humidity of the air is low (40 to 85 %) when a dark band occurs. Whether the low humidity is related to the dark band is not known, as there no measurement has been analysed out during high humidity conditions.

The depth of the dark band seems to be statistically unrelated to the particle number density, which is a sign that interaction between particles is not important. The measurements with a much larger number density tended to belong to periods with a less deep dark band, however. The diameter of the particles is statistically related to the depth of the dark band. This is an indication that the size (which is closely related to the shape) of the ice precipitation is important. The absolute values of the calculated diameters and especially of the particle number densities should be used with caution.

When the lidar is tilted under a small angle, the lidar backscatter in the rain is reduced 6 to 8 dB and the water dark band depth is decreased considerably. This shallow water dark band is typical for the month of tilted lidar measurements we examined. For the Vaisala lidar ceilometers it is difficult to ascertain the noise level accurately. It is thus possible that the dark band is not present in the tilted measurements

due to an insufficient signal-to-noise ratio in the dark band itself. In the next section it will be assumed that the depth of the water dark band does depend on the measurement angle, i.e. that the signal-to-noise ratio is sufficient. Making tilted measurements with a more powerful scientific lidar should check this assumption. The dark band may be deeper for the green lidar beam, but this requires a more complete study.

The polarisation measurements of Sassen show a low optical depolarisation ratio in the lower part of the dark band. This is an indication that the particles in the lower half are symmetrical. Most likely the optical backscatter comes from a fully water-coated particle, which is almost completely melted.

8.5 Hypotheses

In this section some hypotheses are presented on the causes of the lidar dark band in the melting layer. Many of these ideas depend on assumptions about properties of the melting ice crystals. As these properties are not known, the ideas cannot be thoroughly tested. Because of this and the lack of dedicated measurements, the discussion of these ideas is speculative. This section is included to indicate what the most likely hypotheses are and to determine which type of measurements and theoretical study may be needed to confirm or refute the ideas.

8.5.1 Crystal imperfections

Milk is white because it contains a large number of small fat droplets. Pure water is transparent. Analogously enhancing the transparency of the crystal can decrease the backscatter of an irregular ice crystal. The transparency can be reduced due to all sorts of imperfections, e.g. rough surface, internal cracks and air bubbles. The meltwater can fill up these imperfections and in that way reduce the refractive index gradients that act as scatter centres. This effect is probably strongest for, e.g., graupel, which has many internal surfaces.

Macke (2000) made simulation of an irregularly shaped particle with air bubbles, to serve as a model for graupel and hail. The backscatter of this particle increased with the number of air bubbles. One can imagine that the backscatter of this particle would decrease when the bubbles were filled with water, which would lower the contrast in refractive index. Indeed, in a laboratory experiment Sassen (1977) measured an about 6 dB higher backscatter for an ice drop (frozen waterdrop) compared to the same drop fully melted.

The opposite is also possible. Bubbles and cracks may reduce the backscatter of specularly reflecting ice crystals. Macke (2000) shows this for a hexagonal column.

The bubbles spread the light rays, enhance the sidescatter, and thus reduce the backscatter.

How much this effect can contribute to the dark band will crucially depend on the properties of the initial ice crystals. It is thus important that experiments are done with crystals captured in the wild. Optical scattering calculations of (partly melted) ice crystals can also provide insight into the importance of imperfections.

8.5.2 Enhanced vertical backscatter of waterdrop

The case study of the 1st of April 1998 shows that the lidar backscatter of rain is much higher if the lidar is pointed vertically than if the lidar is pointed under a small angle. This may be due to the shape of the droplet. The frictional forces on the droplet may flatten its base [Chuang and Beard, 1990]; this would increase the lidar backscatter in the vertical direction.

The effect of flattening drop bases can cause part of the increase in the optical backscatter in the lower part of the dark band, as the water fraction of the melting crystal may experience a similar flattening as the amount of water becomes larger and the velocity increases. If this effect is important cause of the dark band, a positive correlation between the depth of the water dark band and the velocity in the rain would be logical. With increasing size ($D < 3$ mm), the flatness of the drop increases [Pruppacher and Klett, 1997]. However, such a correlation was not found in all cases. A flat drop base due to friction can explain the much smaller water dark band depth in the tilted lidar measurements. Further research is needed, especially many more measurements with an angle scanning lidar.

8.5.3 Aggregation and breakup

Aggregation and breakup is thought to be present throughout the melting layer. Aggregation, on the other hand, dominates in the top of the melting layer and breakup in the lower half [Barthazy, 1998]. This results in a larger average particle size and a lower particle number flux in the middle of the melting layer. Aggregation and breakup is an important topic for the radar community as it is used to partly explain the high radar reflections in the melting layer. In her careful study Barthazy (1998) combined radar measurements with in situ particle measurements on a mountain slope, and thus showed the existence of aggregation and breakup in the melting layer.

Assuming that the mass density of the particles themselves does not change by aggregation and breakup, the particle volume (third moment of diameter) should stay the same. The radar reflectivity (sixth moment) will thus be highest in the middle

of the melting layer and the lidar backscatter (second order) will be lowest in the middle. With aggregation and breakup one can thus kill two birds (the lidar dark band and the radar bright band) with one stone.

However, there are a few weak points in this explanation. If breakup is the dominant mechanism for the water dark band, the tilt angle of the lidar should not matter, but we found an angular dependence. The contribution of aggregation and breakup to the high reflections in the bright band is normally thought to be limited to a few dB [Fabry and Zawadski, 1995]. The contribution to the dark band should be in the same order of magnitude for a mono-disperse drop size distribution.

The absence of significant aggregation in light rain is supported by the study of Fabry and Zawadzki (1995). They made extensive measurements of radar reflectivity profiles during rain. Looking at the shape of the radar reflectivity profiles above the melting layer, they conclude that when the rain is below 15 dBZ, deposition is a more important growth process for the ice precipitation than aggregation. Above 20 dBZ some other growth process, probably aggregation, dominates. They do not expect aggregation to be more important in the top of the melting layer than in the snow above, as the aggregation efficiency is already large in the ice precipitation and the Doppler spectrum does not change much.

If the water dark band is to be explained by spontaneous breakup, it will have to occur in the lower half of the melting layer. In this part the polarisation measurements of Sassen indicate that the reflections come from waterdrops rather than snowflakes. Spontaneous breakup of waterdrops has only been observed for drops larger than 4.5 mm [Pruppacher and Klett, 1997, p. 410].

In case of aggregation and breakup one would expect a positive relation between number density and the depth of the dark band. Because the number density is related to the number of collisions. No such correlation has been found with the droplet number density in the rain, which is thought to be a measure for the number density at other heights as well. There are even some indications that the dark band is less deep for high number densities. Thus one would expect that aggregation and breakup is not a dominant mechanism causing the lidar dark band in the light-rain cases studied.

8.5.4 Collapse of snowflakes

The decrease in backscatter in the top of the melting layer may be explained by the collapse of a melted snowflake into a much smaller particle. This will reduce the area of the particle and reduce the number density (as the fall speed increases). Both effects will contribute to a lower backscatter. The same effects are used to explain the decrease in *radar* reflectivity in the bottom of the melting layer.

Collapse of the particle is closely related to the particle fall velocity. The lidar dark band starts at the top of the melting layer: The lidar backscatter is already decreasing sharply when the radar velocity is still barely increasing (and thus the particle size should still be about the same). What is more, the velocity is still increasing when the lidar backscatter starts to increase in the rain. This increase in lidar backscatter in the lower part of the melting layer is actually counteracted by the decrease in area and number density.

The radar velocity is of course not identical to the velocity of the particles that dominate the lidar backscatter. The lidar reflections mainly come from the smallest part of the size distribution; this part will also melt first. The radar reflections (and its velocity) are biased towards the largest particles in the size distribution. The best test of collapse of the particle as an explanation for the dark band will thus be a measurement of the melting layer with one of the new near-infrared Doppler lidars [Frehlich, 1997].

8.5.5 Enhanced vertical backscatter in ice precipitation

In case of very light rain it may be more useful to think of single crystals instead of aggregated snowflakes. The shape and orientation of such crystals is important. Especially in the optical regime ice crystals can have a very narrow scattering peak around the normal of the particle. Crystals fall with their biggest dimension horizontally aligned, and thus reflect strongly in the vertical direction. This is a well-known phenomenon in cirrus clouds. Thomas et al. (1990) have measured an angular distribution of just 0.3° around the zenith in cirrus; Platt et al. (1978) a distribution of 0.5°. Sassen (2000) has often measured the same angular dependence in virga (precipitation that does not reach the ground).

In the upper part of the dark band the power could decrease as the crystal shape changes or because the crystals are no longer falling horizontally. Asymmetric melting, e.g., may cause this disalignment.

By taking into account the shape and orientation of the ice crystal a very deep dark band is possible [Venema et al., 1998]. It may explain why the dark band begins high in the top of the melting layer. Aggregation may broaden the scattering peak and thus reduce the depth of the dark band. This would be a mechanism by which the correlation between number density and the depth of the ice dark band can become negative. There is some indication of such a negative correlation.

In one case Sassen (2000) observed no specular reflections in the falling ice crystals 10 minutes before the dark band appeared. It is therefore highly likely that in this dark band enhanced vertical backscatter played no role in the melting layer. It might still play some role in other measurements of deeper dark bands. Another important problem of this explanation is that horizontally oriented planar crystals have an opti-

cal depolarisation near zero and in the measurements of Sassen and Chen (1995) and Sassen (2000) a linear depolarisation ratio of above 50 percent was found. Most likely this explanation does not agree with the observations.

8.5.6 Blockage of rear surface raindrop

A spherical waterdroplet has three important ways for scattering light back to the lidar [Sassen, 2000]. Part of the light is captured by a surface wave and part is scattered back by the front and rear drop faces. As the front surface acts as a lens, the rear face is a significant contributor, according to Sassen (2000). An ice crystal in the middle of a waterdrop may block the contribution of the rear face. Sassen and Chen (1995) and Sassen (2000) claim that the backscatter in the dark band is lower compared to the ice due to collapse of the particle. They claim that the backscatter is lower in the dark band than in the rain because of this blockage effect by the remaining ice of a nearly completely melted particle.

Sassen (1977) supports his hypothesis by reprinting a laboratory measurement of the reflected energy of a suspended melting ice drop. This measurement in Sassen (2000) shows a 2 dB lower reflection of the almost completely melted drop compared to the fully melted drop. There are two problems with this hypothesis. First of all, 2 dB is not enough: the depth of the water dark band is much more.

The second problem is that the plot from Sassen (1995) of returned energy as a function of the melt time is the co-polar return from Sassen (1977), not the total backscatter; the cross-polar return is omitted. The co-polar return does increase when the ice crystal is almost melted and it moves to a position in the middle of the drop, but the cross-polar return decreases at this moment. The *total* returned power of the almost melted particle is actually larger than that of the fully melted particle in this laboratory experiment. The increase in co-polar return is probably due to the reduction of the leakage to the cross-polar return as the particle becomes symmetrical.

This change from an asymmetrical to a symmetrical particle could theoretically give a dark band of 3 dB for a co-polarised lidar. As the Vaisala systems are about 3 times more sensitive to the cross-polar return, these lidars should actually receive more power from the asymmetrical particles in the top of the melting layer than from the symmetrical drops. The HTRL lidar receives all polarisations and should thus not see this contribution to the dark band.

8.5.7 Absorption

De Wolf and Russchenberg (1999) explain the dark band by attenuation of the lidar signal due to cumulative *absorption* in the lower half of the melting layer and strong

reflections by large snowflakes in the top of the melting layer. To get 10 dB absorption in 100 m they use a number density of 2000 m^{-3}, and a particle diameter of 6.7 mm.

Both particle parameters are much higher than those from the first-order calculation from the radar measurements. The main problem with this explanation is, however, that with such a high absorption in the lower melting layer, the lidar would never have been able to penetrate a few kilometres through the rain up to melting layer in the first place. This explanation can only work if there is a reason to assume that the absorption of an almost melted particle is much higher than that of a fully melted raindrop. Furthermore, absorption cannot explain the angular dependence found in the water dark band depth.

8.6 Discussion of the hypotheses

Summarising the argumentation in section 8.5, the most likely dominating mechanism for explaining the water dark band is the enhanced vertical backscatter due to a flat drop base of a falling raindrop. A secondary effect could be breakup of the melting particles. A weak point of the flat-drop hypothesis is that the correlation between water dark band depth and the diameter is not always positive. However, the empirical data favours this hypothesis and the correlation could be perturbed by other causes. Aggregation and breakup will occur but is probably no very significant for the dark band, especially as the dark band is also seen in *very* light rain cases.

To strengthen the flat-drop hypothesis, measurements with a powerful scanning lidar would be valuable. Such a lidar system should be powerful enough to have a good signal-to-noise ratio in the minimum of dark band itself and in the rain while measuring under an angle. A scattering calculation would be valuable to estimate how much this mechanism can contribute to the water dark band.

For the ice dark band there are a few good hypotheses. The two most likely ones are crystal imperfections that are reduced due to melting and collapse of the melting particles. Aggregation could play a secondary role. These hypotheses are suggested as little or no empirical evidence against them was found, and they appear to be theoretically sound. The collapse hypothesis does not fit with the radar velocity, but may still be confirmed by a Doppler lidar measurement.

For investigating the importance of crystal imperfections of the ice precipitation measurements in a wind tunnel of melting natural particles should be made. Also a modelling study could provide more insight.

The three remaining hypotheses have major empirical or theoretical problems.

8.7 Conclusions and recommendations

The melting layer shows up in radar measurements as a bright band, i.e. a layer with high reflections. In lidar measurements the reflections in a part of the melting layer are low compared to its environs: a dark band. The difference in reflectivity between the melting layer and the rain in the cases studied can be up to 20 dB and compared to the ice precipitation up to 30 dB.

The lidar reflections in the upper half of the dark band come from an irregular particle, whereas those in the lower half come from a symmetrical particle. The depth of the dark band seems to be (statistically) unrelated to the number density of the particles. The dark band is quite thin: it is just 200 to 300 m wide. And the decrease of lidar reflectivity starts at a height well above the height at which the radar velocity starts to increase. The lidar backscatter in rain is found to be 6 to 8 dB higher when the lidar is pointed to the zenith compared to the backscatter under a small angle.

The explanation of this dark band is far from certain yet. Discussed mechanisms were: crystal imperfections, enhanced vertical backscatter of raindrops, aggregation and breakup, collapse of the particle, enhance vertical backscatter of the ice precipitation, blockage of the backscatter from the rear surface of a drop by an ice nucleus, and absorption. At least several of these mechanisms will simultaneously contribute to the dark band depth. Their importance for explaining the lidar dark band cannot be quantified yet. For the water dark band the enhanced vertical backscatter of raindrops is the most likely candidate, and breakup of the melting particles could contribute to some extent. For the ice dark band the best candidates are crystal imperfections and particle collapse. Aggregation may contribute somewhat.

Many uncertainties may be resolved by making fall speed measurements of the optically dominating particles in the melting layer with a Doppler lidar. This could prove whether collapse of the particle enhances or reduces the depth of the dark band. Together with radar velocity measurements, it could estimate the difference in size between the dominant scatterers for both instruments. If the sizes (velocities) are about the same, one can estimate the maximum possible amount of aggregation and breakup.

More (quasi-)simultaneous measurements with lidars under two observation angles (vertical and some small angle) would provide information about how strongly enhanced vertical reflections in the rain are.

Theoretical simulations and laboratory measurements of the optical scattering of natural particles that are melting could also provide more insight into what happens in the melting layer.

Acknowledgements. I would like to thank Marcus Quante and Olaf Danne of GKSS, Germany, for access to their mm-wave radar data and everyone at their institute for an inspiring and pleasant visit. Furthermore, I would like to thank all people at my institute with whom I had fruitful discussions.

Appendix. Calculation of rain parameters

The purpose of this calculation is to see whether there is a relation between the dark band depth and the microphysical properties of the precipitation. Therefore, we will only make a simple order of magnitude calculation of the diameter and the number density in the rain, assuming a mono-disperse drop size distribution. The velocities (V) have been converted into raindrop diameters (D), assuming no average vertical wind, using a fit to the results of Beard (1976), for $1 < V < 7$ m/s:

$$D[\text{mm}]=0.29V[\text{m/s}]-0.24 \tag{8.1}$$

These diameters and the radar reflectivities have been used to calculate the number densities in the rain, using:

$$N = Z / D^6 \tag{8.2}$$

This method only gives a rough estimate as vertical wind can influence the calculated diameter, and this will have a strong influence on the calculated number density. Another source of uncertainty lies in Eq. (8.1) itself; it can also be formulated as $V = 9.65 - 10.3 \exp(-0.6D)$. With this formulation the estimated diameters will be larger and thus the calculated number densities lower. The absolute rain parameters (D and N) are thus subject to a considerable error. For the correlations between number density (or diameter) and dark band depth the difference between these formulations is, however, small.

The drop size distribution (especially its width) has to be known for accurate absolute values of the rain parameters. The measured average velocity is weighted based on the radar reflectivity of the droplets. The real average velocity will thus be lower and consequently the real diameter will be lower and the number density higher.

Concluding: the absolute values are unreliable and the relative values will have a large scatter, but are on average likely to be a monotonous function of the absolute values.

Reference

Apituley, A., A. van Lammeren, and H.W.J. Russchenberg. High time resolution cloud measurements with lidar during CLARA. *Phys. Chem. Earth (B)*, 24, no. 2, pp. 107-114, 2000.

Barthazy, E. *Microphysical Properties of the Melting Layer.* PhD dissertation Swiss Federal Institute of Technology (ETH), Zurich, Switzerland. no. 12687, 1998.

Beard, K.V. Terminal velocity and shape of cloud and precipitation drops aloft. *J. Atmos. Sci.*, **33**, pp. 851-864, 1976.

Browell, E.V., S. Ismail, and S.T. Shipley. Ultraviolet DIAL measurements of O3 profiles in regions of spatially inhomogeneous aerosols. *Appl. Opt.*, **24**, no. 17, 1 Sept., pp. 2827-2836, 1985.

CLARA web pages, http://irctr.et.tudelft.nl/projects/clara/ and http://www.knmi.nl/CLARA/.

Chuang, C., and K.V. Beard. A numerical model for the equilibrium shape of electrified raindrop. *J. Atmos. Sci.*, **47**, no. 11, pp. 1374-1389, 1990.

Fabry, F., and I. Zadwadski. Long-Term Observations of the Melting Layer of Precipitation and Their Interpretation. *J. Atmos. Sc.*, **52**, no. 7, pp. 838-851, 1995.

Frehlich, R. Effects of wind turbulence on coherent Doppler lidar performance. *J. Atmos. Ocean.. Technol.* **14**, no. 1, pp. 54-75, 1997.

Goddard, J.W.F. Nature of precipitation and cloud. In *Propagation of radiowaves*, eds. M.P.M. Hall, L.W. Barclay, and M.T. Hewitt. ISBN: 0-85296-819-1, The Inst. of Electr. Eng., London, UK, 1996.

Van Lammeren, A., A. Feijt, D. Donovan, H. Bloemink, H.W.J. Russchenberg, V.K.C. Venema, J.S. Erkelens, A. Apituley, H. Ten Brink, A. Khystov, S. Jongen, G. Brussaard, and M. Herben. Clouds and radiation: intensive experimental study of clouds and radiation in the Netherlands (CLARA) *Proc. Symposium Remote Sensing of Cloud Parameters: Retrieval and Validation*, pp. 5-10, 21-22 October Delft, The Netherlands, 1999.

Macke, A. Monte Carlo Calculations of Light Scattering by Large Particles with Multiple Internal Inclusions. In *Light Scattering by Nonspherical Particles. Theory, Measurements, and Applications.* M.I. Mishchenko, J.W. Hovenier, L.D. Travis (eds.), ISBN: 0-12-498660-9, Academic Press, San Diego, 2000.

Mirtra, S.K., O. Vohl, M. Ahr, and H.R. Prupacher. A wind tunnel and theoretical study of the melting behaviour of atmospheric ice particles. IV: Experiment and theory for snow flakes. *J. Atmos. Sci.*, **47**, pp. 584-591, 1990.

Platt, C.M.R., N.L. Abshire, and G.T. McNice. Some Microphysical Properties of an Ice Cloud from Lidar Observations of Horizontally Oriented Crystals. *J. Appl. Meteorol.*, **17**, pp. 1220-1224, 1978.

Pruppacher, H.R, and J.D. Klett. *Microphysics of Clouds and Precipitation; second edition.* Kluwer, Dordrecht, 954 p., 1997.

Russchenberg, H.W.J., and L.P. Ligthart. Backscattering by and Propagation Through the Melting Layer of Precipitation: A New Polarimetric Model, *IEEE Trans. Geosc. and Remote Sensing*, **34**, no.1, pp. 3-14, 1996.

Sassen, K. Lidar Backscatter Depolarization Technique for Cloud and Aerosol Research. In *Light Scattering by Nonspherical Particles. Theory, Measurements, and Applications.* M.I. Mishchenko, J.W. Hovenier, L.D. Travis (eds.), ISBN: 0-12-498660-9, Academic Press, San Diego, 2000.

Sassen, K. Optical backscattering from near-spherical water, ice, and mixed phase drops. *Appl. Opt.*, **16**, no. 5, pp. 1332-1341, 1977.

Sassen, K., and T. Chen. The lidar dark band: An oddity of the radar bright band analogy, *Geoph. Res. Lett.*, **22**, no 24, pp. 3505-3508, 1995.

Szyrmer, W., and I. Zawadzki. Modelling of the Melting Layer. Part I: Dynamics and Microphysics. *J. Atmos. Sci.*, **56**, pp. 3573-3592, 1999.

Tanner, V., product manager Vaisala, personal comm., 2000.

Thomas, L., J.C. Cartwright, and D.P. Wareing. Lidar observations of the horizontal orientation of ice crystals in cirrus clouds, *Tellus*, **42B**, pp. 211-216, 1990.

Venema, V.K.C., H.W.J. Russchenberg, A. Van Lammeren, A. Apituley, and L.P. Ligthart. The melting layer: The radar bright band is dark for lidar. *Proc. of the 8th URSI Commission F Triennial Open Symp.*, 22 Sept., Universidade de Aveiro, Aveiro, Portugal, pp. 159-162, 1998.

Wolf, de, D.A., and H.W.J. Russchenberg. A Tentative Explanation of the Optical "Dark Band" in the Melting Layer. *Proc. Remote sensing of cloud parameters: retrieval and validation*, Delft, The Netherlands, 21-22 Oct., pp. 141-143, 1999.

Chapter 9

Conclusions and recommendations

Abstract. *Much has been learned about performing cloud measurements with a radar in the last four years. Here we repeat the most important conclusions and recommendations from the previous chapters about spectral radar data processing, coherent scattering by clouds, cloud boundary measurements and the lidar dark band. Then more general conclusions and recommendations will be given, some of which apply specifically to cloud research at IRCTR.*

9.1 Spectral radar data processing

Spectral radar data processing can enhance the sensitivity of a cloud radar considerably. Unfortunately due to the distributed nature of clouds, this enhancement has much less effect for clouds than for targets with just one radial velocity. Clipping of the velocity spectra is effective in reducing the noise, but it can also reduce the measured power of cloud signals with a low SNR and a relatively high spectral width. It is possible to correct for this undesired effect if the shape of the original signal is known.

More work is needed to make a good error estimate. What errors are made, for example, if the width of the velocity spectrum, which is used for the correction, is wrong, or if the spectrum has a different shape?

The full velocity spectrum gives information on the shape of the distribution (including the width) as well as on clutter, disturbances in the system, and bimodal or

multimodal spectra. For this reason it would be useful to store the complete velocity spectrum. The clipping correction function needs information on the shape of the spectrum as input; if the SNR of the velocity spectrum were much better (more than 10 dB) than the spectra from which the moments were calculated, this would allow a very reliable clipping correction.

The clipping method could be used as a first step in a more sophisticated processing method, given enough calculation power. The calculated velocity (and possibly the spectral width) could, for example, be used to define a clipping region: Only values from the original velocity spectrum within this clipping region should then be used in the calculation of the moments.

9.2 Coherent particle scatter

Besides coherent air scattering from variations in refractive index of the air (clear-air/Bragg scattering) and incoherent particle scattering (Rayleigh scattering), coherent scattering by ensembles of particles may also be important in explaining radar measurements of the atmosphere. Coherent air scattering from variations in humidity in clouds is probably less important than has previously been thought.

Dual-frequency measurements of cumulus clouds can be largely explained by a new equation for coherent scatter by waterdroplets. This shows that in parts of the cumulus clouds coherent scattering from the droplets may be the dominating scattering mechanism.

Theoretical calculations show that coherent particle scatter can dominate coherent air scatter in the top part of cumulus clouds. In stratiform clouds one cannot say whether coherent particle scatter or coherent air scatter is strongest given the large margin of error; simultaneous measurements of humidity and LWC (Liquid Water Content) variations will have to be made to determine which mechanisms dominate. For an S-band radar measurement of stratocumulus clouds, a typical condition for the CLARA campaigns, coherent scatter can be significant compared to incoherent scatter.

The slope of the humidity and LWC variance spectra may be very important for determining whether coherent air scattering or coherent particle scattering is the dominant reflection mechanism in a cloud.

To test the theory of coherent particle scatter, simultaneous measurements of LWC, humidity (and temperature) variations should be compared with radar measurements of coherent scatter. Measurements of the LWC and humidity spectra of a range of different cloud types should be made, together with estimates of the inner scale of the inertial subrange, to determine which type of coherent scatter is important for which type of cloud. Once the theory of coherent particle scatter has been devel-

oped more fully it may be possible to use this scattering mechanism to improve retrievals of LWC, cloud boundaries and spatial humidity and LWC variations.

Big fires can strongly reflect radio waves from rain radars. This may be due to coherent scattering by the smoke particles. Radar might help quantifying this source, and may be used for the early detection of dangerous large fires.

9.3 Cloud boundary measurements

To measure cloud boundaries accurately under a broad range of atmospheric conditions one has to use both lidar and radar. Physical processes whose influence on measurements of cloud geometry is important are particle size, attenuation and maybe specular reflections. The current measurement techniques still have to be improved a great deal before performing representative operational cloud measurements under almost all atmospheric conditions is feasible. Difficult and regularly occurring conditions are rain and virga. Also difficult from a measurement point of view are ice clouds with a broad size distribution and ice clouds with specular reflections. How often these problems occur should be the subject of further study and optimised measurement techniques have to be developed for these cases.

The measurement artefacts created by specular reflections should disappear when the lidar is tilted under a small angle. Tilting the lidar will also enhance the contrast between cloud droplets and raindrops due to the higher backscatter of raindrops in the vertical direction.

Radar may be able to measure the cloud geometry during rain (including rain that does not reach the ground) when information of the velocity spectra in used. In the rain measurements the cloud may be made visible using the power of the upward moving particles, even though the *average* velocity is dominated by the precipitation. But as updrafts and downdrafts easily perturb the velocity of the cloud particles, Doppler polarimetry or multi-frequency power spectra may be necessary to unambiguously identify the cloud particles.

The radar should, furthermore, have a very high sensitivity, in the order of -40 dBZ. Even then some clouds may still remain undetected. For the techniques that use the full power spectrum more sensitivity is also required. Maybe cm-wave radars need not be this sensitive due to relatively strong coherent particle scatter.

9.4 Lidar and radar measurements of the melting layer

The melting layer shows up in radar measurements as a bright band, i.e. a layer with high reflections. In lidar measurements the reflections in a part of the melting layer

are low compared to its environs: a dark band. The difference in reflectivity between the melting layer and the rain in the cases we studied sometimes reached values up to 20 dB and compared to the ice precipitation up to 30 dB. Lidar backscatter in the upper half of the dark band comes from irregular particles, whereas the backscatter in the lower half comes from symmetrical particles. The lidar backscatter in rain is found to be 6 to 8 dB higher when the lidar points to the zenith compared to the backscatter under a small angle.

The explanation of this dark band is far from certain yet. For the water dark band the enhanced vertical backscatter of fast falling raindrops is the most likely candidate, and breakup of the melting particles could contribute to some extent. For the ice dark band the best candidates are crystal imperfections, collapse and the change in their shape and orientation due to melting. Aggregation may contribute somewhat.

It would be useful to have a Doppler lidar next to a Doppler radar for some measurement campaigns. This could prove whether collapse of the particle enhances or reduces the depth of the dark band. Together with radar velocity measurements, Doppler lidar could estimate the difference in size between the dominant scatterers for both instruments.

More (quasi-)simultaneous measurements with lidars under two observation angles (vertical and some small angle) would provide information about how strong enhanced vertical reflections in the rain are. Theoretical simulations and laboratory measurements of the optical scattering of natural particles that are melting could also provide more insight into what happens in the melting layer.

9.5 Outlook

Much progress has been made in recent years in retrievals of cloud properties. A large obstacle is the difficulty of making a good evaluation of the quality of the retrievals. It is very hard to accurately compare the retrieved values with values measured in situ by aeroplanes; making falsification almost impossible. Improvement of the validations should get a high priority on the research agenda. In future measurement campaigns the aeroplanes should not only fly horizontal laps, but ramps up and down as well. Furthermore, new and improved technologies for making in situ measurements are needed and the comparison methodology deserves systematic study. Measurements using tethered balloons and kites may fit into such a future research program.

Combinations of instruments will be used more and more. That is why super sites with a large number of instruments are very important for monitoring the cloud cli-

mate, improving our understanding of the measurements and developing better retrieval methods.

Radar will likely continue to play a large role in cloud research, as it can measure inside dense clouds. The utility of radar for atmospheric research will be improved by applying tailor-made measurement techniques to specific information demands from the cloud research community. Sometimes this could imply specific processing algorithms, sometimes even specific radar systems. The costs of radar systems and measurement know-how are factors limiting more general use of radar products.

Dual-wavelength radar methods will enhance the retrievals. A very promising retrieval technique is using the difference in attenuation between mm-wave radars. From dual-wavelength radar much can be learnt about coherent scattering. This will open exciting new research perspectives and may improve retrievals of important cloud properties. Without a thorough understanding of coherent scatter, one should use quantitative radar reflectivity values from an S-band radar with caution.

9.6 Recommendations for cloud research at IRCTR

There are plans for building a super remote sensing site at Cabauw in the Netherlands. This would provide great opportunities for making high-quality cloud measurements, which is important for climate research. The co-operation with users and experts from other fields will undoubtedly be very enriching, just as it was in the CLARA project.

IRCTR offers perfect opportunities to study coherent scattering by clouds further. In 1998 we organised a measurement campaign using both DARR (S-band) and SOLIDAR (X-band). This showed very promising results. The beam width and processing of both radars match closely. With an upgrade of SOLIDAR to make this radar more sensitive than DARR, it will be a state-of-the-art measurement facility. Many interesting questions may be answered by such a facility, which will inspire research for the years to come. Questions like, for example, in which cloud types does coherent scatter occur, what are the sources and sinks of spatial structures, and is it possible to use coherent particle scatter to improve cloud retrievals?

Two important instruments for enhancing radar measurements are lidar and the microwave radiometer. It would be good if IRCTR were to obtain them or find some way it could frequently use them for a short campaign. This will facilitate and speed up the development and testing of better retrieval methods for cloud properties.

Building a low-cost mm-wave cloud radar can open new possibilities for radar cloud research as it will lead to a much more frequent use of radar for cloud measurements and allows studies where many radars are used to examine what the influence clouds have on the climate system on large (e.g., continental) scales. The starting position of IRCTR to design such a system is very good; it has state-of-the-art mm-wave measurement facilities, know-how of MMIC, an active cloud remote sensing group, and a radar design group that just proved that it can build a complete radar system from scratch

Dankwoord

Bij het begin van mijn promotie werd ik direct in het diepe gegooid. Na twee weken begon namelijk direct de eerste CLARA campagne. Gelukkig had mijn copromotor, Herman Russchenberg, alles goed voorbereid, leerde hij me de radarbeelden lezen, en wist me snel in te wijden in de radar-wirwar van kabels, knopjes, programma's en files. Het diepe bestond vooral uit een zee van mensen; wolkenonderzoek begint op hoge-energie fysica te lijken. Ik ben dus dank verschuldigd aan tientallen mensen, van alle technici en wetenschappers die de instrumenten hebben geïnstalleerd en bediend tot de mensen die me hebben geleerd om weerballonnen op te laten; van de piloot van het meetvliegtuig en van de vluchtleiding in Schiphol tot de meteorologen van het KNMI die speciale wolkenverwachtingen maakten. Allemaal erg bedankt: dit is ook deels jullie proefschrift.

Mooie metingen doen is één ding, het meeste werk is ze uitwerken. De samenwerking met de andere instituten was erg vruchtbaar. Arnoud Apituley van het RIVM en André van Lammeren van het KNMI hebben een grote bijdrage geleverd aan dit proefschrift. Van hen heb ik veel geleerd over lidars en optische meettechnieken. Mijn promotor, Leo Ligthart, heeft tijdens mijn promotie enorm veel energie gestoken in het opbouwen van het IRCTR. De prima faciliteiten die hierdoor beschikbaar zijn, maken het werk een stuk plezieriger. Vele collega's en studenten hebben me geholpen mijn inzicht in radars en de atmosfeer te vergroten met hun kennis of gewoon als praatpaal; Alex Gibbs, Annemarie Schipper, Jan Erkelens, Christien Unal, Dmitri Moisseev, en Sylvester Heijnen, allemaal ontzettend bedankt. Jan Erkelens moet ik speciaal bedanken. Jarenlang kwam hij 's avonds na blokuren bij me langs om te brainstormen over zijn ideeën over verstrooiing van radiogolven door wolkenstructuren. Ondanks dat onze collega's gek werden van de turbulente wervel-

tjes en de conservatieve passieve additieven hebben we doorgezet en dit heeft uiteindelijk geresulteerd in de twee mooiste hoofdstukken van dit proefschrift.

Als laatste wil ik mijn vrienden bedanken die mij de energie gaven om door te gaan. Mijn vrienden uit Groningen: Liesbeth, Peter en Remco, jullie steun was onmisbaar, vooral toen ik in Delft nog niemand kende. Dat ik me later beter thuis begon te voelen in het Westen komt door Dmitri, en mijn vrienden in het Delfts Universitair Milieuplatform, GroenLinks Delft en het International Research Centre for Pubs and Restaurants (IRCPR). Iedereen bedankt.

Publications

Venema, Victor, Jan Erkelens, Herman Russchenberg, and Leo Ligthart. Clear-air scattering observations: downdraft and angels. *Proc. of the First European Conference on Radar Meteorology* (ERAD), Bologna, Italy, 4-8 September 2000, published in special issue of Physics and Chemistry of the Earth, 2000.

Venema, Victor, Jan Erkelens, Herman Russchenberg, and Leo Ligthart. Coherent particle scatter in clouds: reflection calculations based on in-situ measurements. *Proc. 13th International Commission on Clouds and Precipitation (ICCP)*, Reno Area, Nevada, USA, pp. 260-263, 14-18 August, 2000.

Victor Venema, Herman Russchenberg, Arnoud Apituley, Andre van Lammeren, Susanne Crewell, and Leo Ligthart. Radar and Lidar Observations of the Melting Process in the Bright Band. *Proc. IGARSS 2000*, Hawaii, USA, pp. 1580-1583, 24-28 July, 2000.

Erkelens, Jan, Victor Venema, Herman Russchenberg, and Leo Ligthart. Coherent scattering of microwaves by particles; Evidence from clouds and smoke. *Journal of the Atmospheric Sciences*, in press, 2000.

Venema, V.K.C., H.W.J. Russchenberg, A. Apituley, A.C.A.P. van Lammeren, and L.P. Ligthart. Cloud boundary height measurements using lidar and radar. *Physics and Chemistry of the Earth*, **24**, no. 2, pp. 129-134, 2000.

Boers, R, H.W.J. Russchenberg, J.S. Erkelens, V.K.C. Venema, A.C.A.P. Van Lammeren, A. Apituley, and S. Jongen. Ground-based remote sensing of stratocumulus properties during CLARA-1996. *J. Appl. Meteorol.*, **39**, no. 2, pp. 169–181, 2000.

Venema, Victor, Jan Erkelens, Herman Russchenberg, and Leo Ligthart. Some notes on scattering of radiowaves by clouds. *Proc. Symposium Remote Sensing of Cloud Parameters: Retrieval and Validation*, pp. 63-70, 21-22 October Delft, The Netherlands, 1999.

Van Lammeren, A.C.A.P., A. Feijt, D. Donovan, H. Bloemink, H.W.J. Russchenberg, V.K.C. Venema, J.S. Erkelens, A. Apituley, H. Ten Brink, A. Khystov, S. Jongen, G. Brussaard, and M. Herben. Clouds and radiation: intensive experimental study of clouds and radiation in the Netherlands (CLARA). *Proc. Symposium Remote Sensing of Cloud Parameters: Retrieval and Validation*, pp. 5-10, 21-22 October Delft, The Netherlands, 1999.

Erkelens, J.S., V.K.C. Venema, and H.W.J. Russchenberg. Coherent particle scatter in developing cumulus clouds. *Proc. Radar Meteorology 99*, Montreal, Canada, 1999.

Erkelens, J.S., V.K.C. Venema, and H.W.J. Russchenberg. Coherent Particle Scatter in a Smoke Plume and Cumulus Clouds. *Proc. Igarss99*, June 28-July 2, Hamburg, Germany, pp. 687-689, 1999.

Venema, V.K.C., H.W.J. Russchenberg, and L.P. Ligthart. Correction for clipping of Doppler spectra from clouds and other atmospheric targets. *Proc. Igarss99*, June 28-July 2, Hamburg, Germany, pp. 1180-1183, 1999.

Russchenberg, H.W.J., V.K.C Venema, A.C.A.P. van Lammeren, A. Feijt, and A. Apituley. Observations of the vertical structure of stratocumulus with lidar and an S-band radar. *Proc. Radar 4th International Symposium on Troposphere Profiling: Needs and Technologies*, Snowmass, Colorado, USA, 21-25 Sept., pp. 185-187, 1998.

Venema, V.K.C., H.W.J. Russchenberg, and L.P. Ligthart. The effect of the orientation of ice crystals in the melting layer and ice clouds on measurements using radar and lidar. *Proc. Scattering by Non-spherical particles*, New York, USA, 29 Sept.., pp. 136-139. Published by American Meteorological Society, Massachusetts, USA, 1998.

Venema, V.K.C., H.W.J. Russchenberg, A.C.A.P. van Lammeren, A. Apituley, and L.P. Ligthart. The melting layer: The radar bright band is dark for lidar. *Proc. of the 8th URSI Commission F Triennial Open Symp.*, 22 Sept., Universitade de Aveiro, ISBN: 972-8021-65-8, pp. 159-162, 1998.

Russchenberg, H.W.J., V.K.C. Venema, A.C.A.P. Van Lammeren, and A. Apituley. *Cloud measurements with lidar and a 3 GHz radar.* Final report for ESA, contract PO 151912, published by IRCTR, Delft, 42 p., no. IRCTR-S-008-98, 1998.

Russchenberg, H.W.J., V.K.C. Venema, A.C.A.P. van Lammeren, and A. Apituley. Radar-lidar observations of clouds during the CLARA-campaigns. *Proc. Workshop on Synergy of Active Instruments in the Earth Radiation Mission*, 12-14 November, GKSS Research Centre, Geesthacht, Germany, pp. 161-165, rep. no. ESA EWP-1968, rep. no. GKSS 98/E/10, 1997.

Summary

Cloud measurements with radar

Victor Venema

In the CLARA campaigns the macrophysical and microphysical cloud properties were measured in situ by aeroplane and with a large number of remote sensing devices: S-band radar, near-infrared and optical lidar, microwave radiometer, infrared radiometer, radiosondes, satellites and GPS, amongst others. The campaigns focussed mainly on stratiform water clouds, stratocumulus and stratus. CLARA was organised by four institutes: KNMI, IRCTR, RIVM and ECN. This PhD thesis was prepared at IRCTR, a radar research institute at Delft University of Technology that operates an S-band (9-cm wavelength) atmospheric radar, DARR.

Important cloud parameters for research on the interaction of cloud and radiation are cloud height (base and top), liquid (or ice) water content, number density and the diameter of the droplets. This thesis focuses on improving (our understanding of) radar measurements of the cloud boundary height and liquid water content of clouds. For many retrievals of the liquid water content an accurate measurement of the radar reflectivity factor is required. During the project we found that combining instruments improves the quality of the measurements considerably. Therefore sensor synergy became an important research theme as well.

This thesis demonstrated that although our spectral processing method, via clipping, increased the sensitivity of DARR to clouds, care must be taken with the measured radar reflectivity factors from clouds since these can be reduced by this method. It is possible to correct for this undesired effect if the shape of the original spectrum is known. A method will be presented here to correct the measured reflectivities for clipping, thus allowing quantitative recovery of the radar data.

In the literature it is conventionally assumed that the radar scattering by particles is incoherent, i.e. that the reflected power of the particles can be simply added to get the reflected power of all particles. It will be shown that in some radar measurements coherent *particle* scatter (by cloud structures) can dominate the incoherent scatter. Coherent *air* scattering from spatial structures in humidity in clouds is probably less important than has previously been thought. Dual-frequency radar measurements of cumulus clouds can be largely explained by a new equation for coherent scatter by waterdroplets. This shows that in parts of the cumulus clouds coherent scattering from the droplets is likely the dominating scattering mechanism in these measurements. For measurements of stratocumulus clouds by an S-band radar coherent scatter can be significant compared to incoherent scatter. The slope of the humidity and LWC variance spectra may be very important. Measurements of the LWC and humidity spectra should be made for a range of different cloud types, together with estimates of the inner scale of the inertial subrange to determine which type of coherent scatter is important for which type of cloud.

The measurement of cloud boundaries is not only important for climate studies directly, but also for some algorithms to retrieve cloud properties. It is shown that for reliable measurements the combination of lidar and radar is indispensable; either instrument by itself is often incapable of getting good results. Physical properties and processes whose influence on measurements of cloud geometry is important are the width of the particle size distribution, attenuation and maybe specular reflections. Difficult and regularly occurring conditions are multiple cloud layers, rain and virga, ice clouds with a broad size distribution and possibly ice clouds with specular reflections. The measurement artefacts created by specular reflections should disappear when the lidar is tilted under a small angle. Radar may be able to measure the cloud geometry during rain (including rain that does not reach the ground) when information of the full velocity spectra is used.

As an exercise in sensor synergy, radar and lidar measurements of the melting layer of precipitation are analysed. This layer, in which ice melts into rain, typically gives high radar reflections and is therefore, called the bright band. Lidar reflections in the melting layer are lower than those of its environs; this is called the lidar dark band. The difference in reflectivity between the melting layer and the rain in the cases we studied sometimes reached values up to 20 dB and compared to the ice precipitation up to 30 dB. By analysing simultaneous measurements with radar and lidar one gains insight into this dark band. The lidar dark band is seen for very low rain rates, with radar reflectivities down to 0 dBZ. Some hypotheses about the cause of the dark band are tested against the results of this data analysis.

Samenvatting

Wolkenmetingen met radar

Victor Venema

In de CLARA campagnes werden de macro- en microfysische eigenschappen van wolken gemeten, zowel *in situ* met een vliegtuig als op de grond met een groot aantal *remote sensing* instrumenten: S-band radar, nabij-infrarood en optische lidar, microgolf radiometers, infrarood radiometers, radiosondes, satellieten, en GPS, onder andere. De meetcampagnes waren gericht op stratiforme bewolking, stratocumulus en stratus. CLARA was opgezet door vier instituten: KNMI, IRCTR, RIVM en ECN. Dit proefschrift is geschreven aan het IRCTR, het radaronderzoeksinstituut van de Technische Universiteit Delft, welke een S-band (9 cm golflengte) atmosferische radar in haar bezit heeft, DARR.

Belangrijke grootheden voor het onderzoek naar de interactie tussen wolken en straling zijn de wolkhoogte (onder- en bovenkant), water of ijsinhoud, deeltjesdichtheid, en de diameter van de druppels. Dit proefschrift is gericht op het verbeteren van ons begrip van radarmetingen van de hoogte en de waterinhoud van wolken. Vele van de methoden om de waterinhoud van wolken te schatten hebben nauwkeurig metingen van de radarreflectiviteitsfactor nodig. Gedurende het project bleek dat door het combineren van de signalen van de instrumenten men de kwaliteit van de metingen fors kan verbeteren. Daarom is ook de synergie van instrumenten een belangrijk onderzoeksthema geworden.

Dit proefschrift toont aan dat de gebruikte spectrale databewerkingsmethode, *clippen*, de gevoeligheid van DARR voor wolkenreflecties vergroot, maar dat tegelijkertijd de gemeten radarreflectiviteitsfactor zal afnemen voor wolken met een lage signaal-ruisverhouding. Het is mogelijk om dit laatste ongewenste effect te compenseren als de vorm van het originele spectrum bekend is. We geven een methode om de gemeten reflecties te corrigeren voor het *clippen*, zodat het kwantitatieve gebruik

van de radar data met lage signaal-ruisverhouding weer mogelijk wordt.

De schattingmethoden die gebruik maken van kwantitatieve radarreflecties nemen normaal aan dat de verstrooiing van de microgolven aan deeltjes incoherent is, dwz. dat het gereflecteerde vermogen van de deeltjes kan worden opgeteld om het gereflecteerde vermogen van alle deeltjes te krijgen. Dit proefschrift zal laten zien dat in sommige radarmetingen coherente deeltjesverstrooiing (door wolkenstructuren) de incoherente verstrooiing kan domineren. Coherente verstrooiing door ruimtelijke structuren in de waterdamp in wolken zijn waarschijnlijk minder belangrijk dan tot nu toe gedacht. Dubbele-frequentie radarmetingen van cumuluswolken kunnen grotendeels verklaard worden met een nieuwe formule voor coherente deeltjesverstrooiing. Dit toont aan dat in delen van cumulus wolken coherente deeltjesverstrooiing waarschijnlijk het dominerende verstrooiingsmechanisme is in deze metingen. Bij metingen van stratocumuluswolken met een S-band radar is coherente verstrooiing significant ten opzichte van incoherente verstrooiing. Metingen van de ruimtelijke variaties in vloeibare waterinhoud en waterdamp van verschillende wolkentypes zijn nodig, samen met schattingen van de *inner scale* van de *inertial subrange*, om te bepalen welk type coherente verstrooiing belangrijk is in welk wolkentype.

Metingen van de hoogte van de wolkengrenzen zijn niet alleen van direct belang voor klimaatonderzoek, maar ook voor sommige algoritmes die de waterinhoud van wolken bepalen. Voor betrouwbare metingen hiervan is de combinatie van lidar en radar onmisbaar; de afzonderlijke instrumenten zullen individueel regelmatig geen goede resultaten kunnen leveren. Fysische processen en eigenschappen die een belangrijke invloed hebben op de meting van wolkengeometrie zijn de breedte van de deeltjesgroottedistributie, demping van het signaal en wellicht spiegelde reflecties. Moeilijke en regelmatig voorkomende situaties zijn overlappende wolkenlagen, regen en virga, ijswolken met een brede deeltjesgrootte distributie en wellicht ijswolken met spiegelende reflecties. De meetproblemen die door spiegelende reflecties ontstaan zouden moeten verdwijnen als de lidar onder een hoek gezet wordt. Radar zou wellicht wolkengeometrie kunnen meten tijdens neerslag (inclusief virga) door gebruik te maken van de informatie in de snelheidsspectra.

Als oefening in sensor synergie hebben we radar en lidar metingen van de smeltlaag van neerslag geanalyseerd. Deze laag, waarin ijs smelt tot regen, veroorzaakt hoge radarreflecties en wordt daarom de heldere band genoemd. De lidar terugverstrooiing in de smeltlaag is lager dan die van de omgeving; dit wordt de lidar donkere band genoemd. Het verschil in terugverstrooiing tussen de smeltlaag en de regen bereikt soms waarden tot de 20 dB en vergeleken met de ijsneerslag tot 30 dB. Door gelijktijdige metingen met radar en lidar te analyseren verkrijgt men meer inzicht in deze donkere band. De lidar donkere band is gezien tijdens zeer lage regenhoeveelheden met radarreflecties beneden de 0 dBZ. Enkele hypothesen over de oorzaken van de donkere band worden getest tegen de resultaten van deze data-analyse.

List of Symbols

Roman

a	Constant
A	Area [m^2]
b	Constant
C	Spatial correlation function
C_n^2	Measure for the total variance of the spatial refractive index variations [$m^{-2/3}$]
c	Speed of Light [m s^{-1}]
D	Diameter (of the droplet) [m]
E	Energy [J]
E_n	Refractive index variance spectrum [m]
F	Frequency excursion [Hz]
f_b	Beat frequency [Hz]
G	Gain of the antenna
K	Constant that depends on the relative permittivity of a particle
k	Wave number [m^{-1}]
l_0	Outer scale of the inertial subrange
ℓ_0	Inner scale of the inertial subrange
l	Correlation length [m]
L_{dr}	Linear Depolarisation Ratio
N	Number of samples or

N	Number of particles
n	Refractive index
P	Power [W]
P_0	Average pulse power [W]
p	Slope of the variance spectrum
Q_v *or* Q_l	Mixing ratio of vapour or liquid water [gr kg^{-1}]
R	Rain rate [mm hr^{-1}]
r	Distance [m]
r_d	Distance between the radar and the target (the range) [m]
Δr	Range resolution [m]
T	Sweep time [s]
Δt	Time period [s]
V	Volume [m^3]
V	Speed [m s^{-1}]
v	Speed [m s^{-1}]
Z *or* Z_e	(Equivalent) radar reflectivity factor [$m^{+6}m^{-3}$]

Greek

α	Extinction coefficient [m^{-1}] or
α	Polarizability of a particle or
α	Amplitude of a scattered wave
β	Relative standard deviation of the spatial liquid water content variations or
β	Lidar backscatter coefficient [$srad^{-1}$ m^{-1}]
Γ	Gamma function
ε_r	Relative permittivity
η	Radar reflectivity; radar cross section per unit volume [m^2 m^{-3}] or
η	Efficiency of the lidar detector
η_0	Kolmogorov scale [m]
θ_b	The -3dB full beam width [rad]
θ	Angle between the transmitted and scattered wave [rad]
k	Wave number [m^{-1}]
κ	Effective wave number [m^{-1}]
λ	Wavelength [m]
λ_c	Critical wavelength [m], smallest radar wavelength within the inertial subrange
ρ	Density [kg m^{-3}] or [m^{-3}]
σ	Radar cross section [m^2]

σ_x	Standard deviation in velocity spectrum due to x [m s^{-1}]
τ	Transmittance
ϕ_D	Phase difference [rad]
φ_n	spatial spectrum of variance of n [m^3]

Abbreviations

Ac	Alto-cumulus cloud
ARM	Atmospheric Radiation Measurement Program
As	Alto-stratus cloud
ASTEX	Atlantic Stratocumulus Transition Experiment in 1992
ATSR-2	Along Track Scanning Radiometer
AVHRR	Advanced Very High Resolution Radiometers
AWATER	Atmospheric WATER project
CaPE	Convection and Precipitation/Electrification Experiment in Florida 1991
CCN	Cloud Condensing Nuclei
CDN	Cloud Detection Network
Ci	Cirrus cloud
CLARA	CLouds And Radiation cloud measurement campaigns
CPA	Conservative Passive Additive
CT-12K or CT-25K	Type of lidar ceilometer made by Vaisala
CT-75K	Type of lidar ceilometer made of four units of the CT-25K
Cu	Cumulus
DARR	Delft Atmospheric Research Radar, S-band radar of TUD
DSD	Drop Size Distribution
DZS	Radar reflectivity factor at S-band
DZS-X	Difference in radar reflectivity factor between S-band and X-band
DZX	Radar reflectivity factor at X-band
ECN	Netherlands Energy Research Foundation
FFT	Fast Fourier Transform, a fast algorithm for a Discrete Fourier Transform
FM-CW	Frequency Modulated Continuous Wave, type of radar system
FOV	Field Of View of lidar receiver
FSSP	Forward Scattering Spectroscope Probe, measure drop size distributions in situ
GKSS	Research Centre in Geesthacht, Germany
GPS	Global Positioning System; measures precipitable water path
HTRL	High Temporal Resolution Lidar

IR	Infrared
IRCTR	International Research Centre for Telecommunications-transmission and Radar
ITS	Faculty of Information Technology and Systems
Ka-band	A radar band between 33 and 36 GHz or around 9 mm.
KNMI	Royal Dutch Meteorological Institute
LDR	Linear Depolarisation Ratio
LWC	Liquid water Content [kg m^{-3}]
LWP	Liquid water Path [kg m^{-2}], LWC integrated over a (vertical) path
MCTEX	Maritime Continental Thunderstorm Experiment
MIRACLE	MIcrowave RAdar for Cloud Layer Exploration
MMIC	Millimetre Integrated Circuit
NIR	Near-infrared
NOP	Dutch National Programme on Global Air Pollution and Climate Change
Ns	Nimbostratus
PVM	Particle Volume Monitor
PMS	Particle Measurement System
RIVM	National Institute of Public Health and the Environment
RMS	Root Mean Square
S-band	A radar band around 3GHz or 10 cm
Sc	Stratocumulus cloud
SCMS	Small Cumulus Microphysics Study in Florida 1995
SNR	Signal-to-Noise Ratio
SOCEX	Southern Oceanic Cloud EXperiment
SOLIDAR	Solid state radar, X-band radar of TUD
St	Stratus cloud
TUDelft	Delft University of Technology
TWT	Travelling Wave Tube amplifier
UHF	Ultra High Frequency; radio frequency band from 0.3 to 3 GHz; 100 to 10 cm
UT	Universal Time
UTC	Universal Time Code
Var	Variance
VHF	Very High Frequency; radio frequency band from 30 to 300 MHz; 10 to 1 m
X-band	A radar band around 1GHz or 3 cm